3-2006

Characteristics of Two-Dimensional Triangular and Three-Dimensional Face-Centered-Cubic Photonic Crystals

Jeffery D. Clark

www.manaraa.com

CHARACTERISTICS OF TWO-DIMENSIONAL
TRIANGULAR AND THREE-DIMENSIONAL
FACE-CENTERED-CUBIC PHOTONIC CRYSTALS

THESIS

Jeffrey Dustin Clark, Major, USAF

AFIT/GEO/ENP/06-01

DEPARTMENT OF THE AIR FORCE
AIR UNIVERSITY

AIR FORCE INSTITUTE OF TECHNOLOGY

Wright-Patterson Air Force Base, Ohio

The views expressed in this thesis are those of the author and do not reflect the official policy or position of the United States Air Force, Department of Defense, or the United States Government.

AFIT/GEO/ENP/06-01

CHARACTERISTICS OF TWO-DIMENSIONAL TRIANGULAR AND THREE-DIMENSIONAL FACE-CENTERED-CUBIC PHOTONIC CRYSTALS

THESIS

Presented to the Faculty

Department of Engineering Physics

Graduate School of Engineering

Air Force Institute of Technology

Air University

Air Education and Training Command

In Partial Fulfillment of the Requirements for the

Degree of Master of Science in Electrical Engineering

Jeffrey Dustin Clark, B.S.E.E.

Major, USAF

March 2006

APPROVED FOR PUBLIC RELEASE; DISTRIBUTION UNLIMITED

CHARACTERISTICS OF TWO-DIMENSIONAL TRIANGULAR AND THREE-DIMENSIONAL FACE-CENTERED-CUBIC PHOTONIC CRYSTALS

Jeffrey Dustin Clark, B.S.E.E.

Major, USAF

Approved:

/signed/	23 Mar 2006
————————————————	————————————
Dr. Michael A. Marciniak (Chairman)	date
/signed/	23 Mar 2006
————————————————	————————————
LtCol James A. Lott (Member)	date
/signed/	23 Mar 2006
————————————————	————————————
Dr. Robert L. Nelson (Member)	date

AFIT/GEO/ENP/06-01

Abstract

Photonic crystals (PhC's) are periodic structures of differing dielectrics that create a photonic band gap (PBG). A PBG, in turn, inhibits the propagation of electromagnetic waves of a specific frequency range. This thesis focuses on the fabrication and characterization of triangular-structured, two-dimensional PhC's with a PBG designed for visible wavelengths and with applications in visible integrated photonic systems. A three-dimensional PhC with a PBG in the infrared is also studied for its characteristics in regard to its PBG.

The two-dimensional fabrication processes pursued were: focused ion beam, electron beam lithography and holographic photo-polymerization/lithography. The fabrication techniques and materials used to create the PhC in part determined the characterization technique required to investigate the PBG. Characterization techniques include: the coupling of a beam by means of a prism into a wave-guiding medium in which the PhC has been fabricated, Fourier transform infrared spectrometer, spectrophotometer, and edge firing techniques. Analysis of the transmission and reflectance properties of a PhC for various incident angles (within the two dimensional plane of the PhC) confirms the presence of a PBG. The design of the PhC was based on a program created to display gap maps for triangular structures. The PBG of the structure, designed from the gap maps, was modeled using another program created to display band diagrams for triangular structures. Finite difference time domain (FDTD) software was then applied to compare the experimental results with the modeling and simulation of the PhC fabricated. Two different FDTD softwares were also evaluated.

The three-dimensional PhC sample obtained was successfully tested with the Fourier transform infrared spectrometer and the spectrophotometer. The results of fabricating two-dimensional PhC's, on the order of visible wavelengths, is shown for

the holographic photo-polymerization/lithography process and the focused ion beam. Modeling and simulation of the these designs were accomplished and compared to some of the experimental results. A design that incorporates the electron beam lithography process was created and modeled.

Acknowledgements

Most importantly, I would like to thank the Lord, without whom nothing is possible. I also owe a great deal of gratitude and adoration to my wife and children for their patience and understanding during this thesis process. I would like to thank my parents for their support and guidance in pursuing my undergraduate degree, making this possible.

Technically, I owe a great deal of thanks to my advisor, Dr. Marciniak, for his technical advice and guidance into this new field. I also want to thank Dr. Nelson for his tutelage in the field of photonic crystals, shedding light on many principles and providing the use of the AFRL laboratories and various equipment. Also deserving of a great deal of thanks are: Lt. Col. Lott for his help in semiconductor properties; Dr. Choquette in the fabrication of a PhC in AlGaAs; Scott Apt in the materials lab at AFRL for his focused ion beam work; Vincent Tondiglia for help with the holographic optic table; Dr. Richard Sutherland for his guidance in the equations necessary to design the holographic setup; Mr. Donald Agresta for his help in material deposition and technical insight helping me achieve the proper index in the desired material. Finally, I need to recognize my friends here at AFIT in their support and camaraderie making this process bearable, and the United States Air Force for this opportunity that I might not otherwise had.

Jeffrey Dustin Clark

Table of Contents

List of Figures

xi

xviii

List of Abbreviations

CHARACTERISTICS OF TWO-DIMENSIONAL TRIANGULAR AND THREE-DIMENSIONAL FACE-CENTERED-CUBIC PHOTONIC CRYSTALS

I. Introduction

Photonics has come to be known as the relationship between electronics and optics, optics being grounded in the "generation, propagation and detection of light" [18]. Thus, photonics is the control of photons [18]. A photonic crystal (PhC) is one way to control these photons. More importantly, a PhC with a photonic band gap (PBG) prevents the propagation of certain wavelengths within the PhC. This thesis focuses on the capabilities of fabrication and characterization of triangular-structured, two-dimensional PhC's with a PBG designed for visible wavelengths and with applications in visible integrated photonic systems. A three-dimensional PhC with a PBG in the infrared is also studied for its characteristics in regard to its PBG. The three different techniques for fabricating these PhC's are: focused ion beam, electron beam lithography and holographic photo-polymerization/lithography. An evaluation of two different finite difference time domain (FDTD) software programs will be discussed.

PhC's can be of one-, two- or three-dimensional structures. A quarter-wave stack is an example of a one-dimensional PhC; examples of two- and three-dimensional PhC's will be covered in this work. The history and theory of PhC's is essential to the understanding of the fabrication techniques used and is presented in this chapter.

1.1   History Behind Photonic Crystals

There are many examples throughout history of man manipulating and using the observable properties of optics. It is documented that Euclid, in 300 B.C., knew of the Law of Reflection, and Plato, in 50 A.D, documented the bending of light in

water. Evidence shows that the Romans possessed burning glasses, thought to be similar to magnifying glasses [9]. By the end of the thirteenth century, Bacan (1215-1294) began inventing lenses for the use of correcting vision [9].

However, in the late 1800's, discoveries made by a few people in a short period of time created a giant leap forward in understanding. Planck, in 1899, published his theory on the quantization of light, which directly affected the development of Einstein's photoelectric effect in 1905. Concurrently, Lord Rayleigh began studying wave propagation in a periodic media (1887) [14], later progressing to more direct studies of a one-dimensional PBG, in which he showed systems that produced such effects [14]. Later in 1904, he discovered the phenomenon now called Rayleigh scattering. In 1922, the publication and study of Bohr's model of the atom furthered the understanding of the nature of photons on the atomic scale. In 1928, Bloch studied wave propagation in a three-dimensional periodic material proving, by adding Maxwell's equations and Schrodinger's equations, that waves in such a media can propagate without scattering [14], thus paving the way for three-dimensional PhC's and PBG's. Ohtaka, in 1979, derived the vector-spherical-wave expansion method, allowing the calculations of dispersion and transmittance for arrays of dielectric spheres [1]. But, the most directly related advancement was made in 1987, when two independent researchers, Sajeev John and Eli Yablonovitch, with two different goals, submitted proposals within months of each other on the probability and possibility of PBG's [25]. Since then, three-dimensional structures have been predicted [12] and fabricated by John and Yablonovitch in 1987. Since John and Yablonovitch were the first to fabricate a three-dimensional PhC with a PBG, the terms that they chose to describe the phenomena (photonic band gap and photonic crystal) were adopted, and they are credited with being the fathers of this field.

1.2 Theory of Photonic Crystals

A PhC is a periodic structure of differing dielectrics that creates a PBG. A crystal-like material is one that has a periodic arrangement of atoms or molecules [12].

2
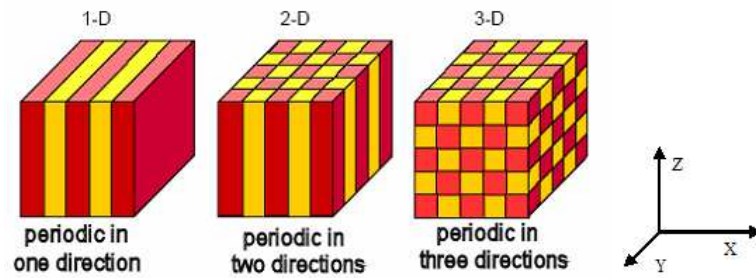
Figure 1.1: Examples of one-, two- and three-dimensional crystal structures. The red and yellow colored regions are regions of different dielectric constants [14].

The geometric placement of these periodic arrangements is crucial to the creation of PhC's – photonic because they scatter light, crystals because they are of a periodic arrangement [16]. Thus, the fundamental principals of a PBG are the same as that of the energy band gap of a semiconductor and analogous qualities exist between the two. The energy band gap of a semiconductor is a complete band gap of that semiconductor and restricts the existence of electrons of the energy band gap states to exist in the material. A three-dimensional PhC, with a PBG, has the same characteristics as that of the energy band gap of a semiconductor. PhC's prevent the propagation of certain frequencies (frequencies on the order of the periodic arrangement); thus, if such a frequency is incident upon the PhC, it will be reflected. The full three-dimensional PBG is a PBG in the crystal and restricts the ability of any photon of that wavelength, propagating at any angle, to exist in the material. Note that a one-dimensional or two-dimensional PhC that contains a PBG does not have a complete PBG based on the previous definition; depending on the angle of incidence, a different periodic structure will be realized and there will be a momentum vector in the reciprocal lattice space (Brillouin zone or k-space) in which the frequency can exist within the crystal. Some basic examples of one-, two- and three-dimensional periodic structures are shown in Figure 1.1. Understanding the details of a PBG requires solving Maxwell's equations within a periodic dielectric material. Maxwell's equations govern the propagation of light [12].

3

$$\nabla \cdot B = 0$$

$$\nabla \cdot D = 4\pi\rho$$

$$\nabla \times E + \frac{1}{c}\frac{\partial B}{\partial t} = 0$$

$$\nabla \times H - \frac{1}{c}\frac{\partial H}{\partial t} = \frac{4\pi}{c}J \tag{1.1}$$

where E is the electric field, H is the magnetic field, D is the displacement field, B is the magnetic induction field, J is free current, ρ is the free charge, c is the speed of light and t is time.

If there are no free charges and no free currents in the material, then $J = 0$ and $\rho = 0$. The material is then a linear, lossless, constant dielectric material and Maxwell's equations reduce to:

$$\nabla \cdot H(\mathbf{r}, t) = 0$$

$$\nabla \cdot \epsilon(\mathbf{r})E(\mathbf{r}, t) = 0$$

$$\nabla \times E(\mathbf{r}, t) + \frac{1}{c}\frac{\partial H(\mathbf{r}, t)}{\partial t} = 0$$

$$\nabla \times H(\mathbf{r}, t) - \frac{\epsilon(\mathbf{r})}{c}\frac{\partial E(\mathbf{r}, t)}{\partial t} = 0 \tag{1.2}$$

where $\mathbf{r}$ is the wave vector. With a few more algebraic manipulations, an equation in regards to the magnetic field $(H(\mathbf{r}))$ [12] is observed.

$$\nabla \times [\frac{1}{\epsilon(\mathbf{r})}\nabla \times H(\mathbf{r})] = (\frac{\omega}{c})^2 H(\mathbf{r}) \tag{1.3}$$

Solving for $H(\mathbf{r})$, the electric field, $E(\mathbf{r})$ [12], is found by:

$$E(\mathbf{r}) = (\frac{-ic}{\omega\epsilon(\mathbf{r})})\nabla \times H(\mathbf{r}) \tag{1.4}$$

4

By rewriting equation (1.3) in the following form, it can be seen that an eigenvalue problem exists [12].

$$\Theta H(\mathbf{r}) = (\frac{\omega}{c})^2 H(\mathbf{r}) \qquad (1.5)$$

where Θ takes the curl, divides by $\epsilon(\mathbf{r})$ and takes the curl again [12]. This operator, Θ, is a linear operator, and thus, in defining the modes, since Θ is linear, any linear combination of solutions is also a solution. So, any fields that differ only by a linear multiplier are of the same mode [12]. In order to solve for the specific frequencies that are either allowed or forbidden to propagate through the crystal, the previously derived equations will be used. If the fields are represented as a set of plane waves and require that $H(\mathbf{r})$ has the same periodicity of $\epsilon(\mathbf{r})$, by using the crystal's reciprocal lattice vectors, then each mode can be represented with a wave vector, $\mathbf{k}$. Also, by expanding $\epsilon(\mathbf{r})$ as plane waves, these equations of plane waves can be inserted into the original equation (1.3). Solving this Hermitian eigenvalue problem [12] is the basic equation behind photonic crystals.

There are several computer software programs available that make these computations; however, each one can be slightly different in the calculations based on assumptions made to solve Maxwell's equations. Regardless, solving these equations by hand would be a long and tedious endeavor at best and in most cases impossible since most cases can only be solved numerically.

Since these solutions are periodic with regards to the wave vector, $\mathbf{k}$, they will be analyzed with respect to the Brillouin zone. The PBG is obtained due to the fact that the fields of the lowest mode try to satisfy the condition of obtaining low energy by having a low curl (slow oscillations). Also, this mode desires to have the electric field concentrated in the high dielectric region. Since the next highest mode has to be orthogonal to the lower mode, it will concentrate its energy in the low dielectric. This gives rise to a frequency band gap [16].

These two modes are also analogous to the semiconductor band gap with respect to electrons; electrons in the conduction band (like modes concentrated in low dielectric) feel fewer restrictions to them than those in the valence band (like modes

5
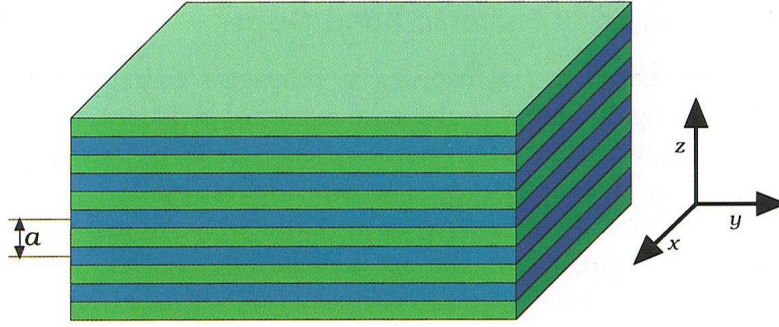
Figure 1.2: One-dimensional crystal, the blue and green represent the different materials of different dielectric constants [12].

concentrated in the high dielectric region). With these concepts in mind, a one-dimensional crystal with a PBG can be examined. A quarter-wave dielectric stack is a good example of a one-dimensional PhC containing a PBG (Figure 1.2). As long as the incident wave is perpendicular to the layers (and has a wavelength that is four times the optical thickness of each layer), it will be totally reflected, due to Bragg reflection. However, if the incident wave is no longer perpendicular to the layers, it will not be perfectly reflected. Looking at the Brillouin zone for this case, a PBG at the edges ($k = \pi/a$, where 'a' is the lattice constant) is observed [12]; the modes at this point are standing waves, *i.e.*, the periodic structure is 180° out of phase with the others in the crystal at this frequency. The modes will tend to be located in high dielectric material for the low frequency mode and the low dielectric material for the next higher frequency mode (Figure 1.3) [12]. In a one-dimensional photonic crystal, there will always be a PBG in the direction of propagation (kz) for some frequency, but not in the off axis (*e.g.* ky) direction for that same frequency.

For a two-dimensional structure (Figure 1.4), PBG's occur at some frequency for any direction within the two-dimensional plane. Consider the two-dimensional plane to be the x-y plane, and therefore, the desire is to create a PBG for any direction in that plane. This can be accomplished with a specific periodic structure (correlating to the wavelength of choice) and differing dielectric constants in the x-y plane. However, now there will be a Brillouin zone that has two distinct polarizations

6

(a) E-field for mode at top of band 1

(b) E-field for mode at bottom of band 2
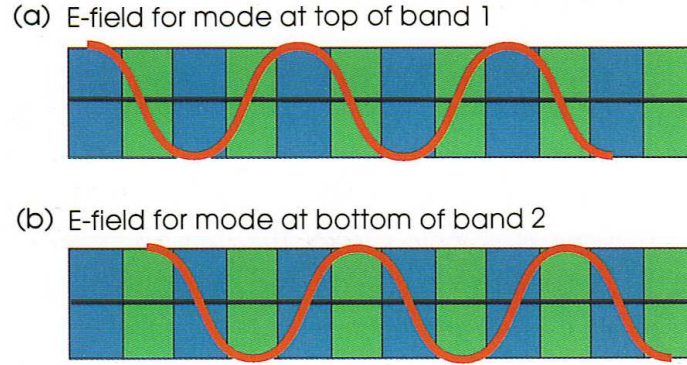
Figure 1.3:   E-field distribution on high dielectric (blue) and low dielectric (green) [12].

to it that is not typically shown in the one-dimensional case, since the one-dimensional case is usually dealing with the incident wave perpendicular to the surface (Figure 1.5) [12]. These polarizations are the transverse electric (TE) and transverse magnetic (TM) waves. TE waves are defined as the case where the electric component is in the plane of incidence and the magnetic component is normal to the plane of incidence. The TM case is where the magnetic component is in the plane of incidence and the electric component is normal to the plane of incidence. Figure 1.5 is a graph of the Brillouin zone where the TM modes have a PBG but the TE modes do not. Thus, the PBG's differ for different polarizations [12].   After several experimentations and calculations, it was found that isolated high dielectric regions make good TM PBG's and connected lattices make good TE PBG's [12]. Therefore, a compromise is necessary to get a complete PBG for both.

Three-dimensional lattice structures are discouragingly difficult to construct. There are a few basic designs that can be produced accurately; however, one of the challenging tasks is to construct a three-dimensional structure on the scale necessary to be used in most applications. Two common types are shown in Figure 1.6. The two-dimensional examples provide building blocks to use for assembling three-dimensional structures. Figure 1.6 illustrates the use of spheres placed in a periodic sequence in which the spheres are touching, and then arranged in a diamond lattice structure to

7
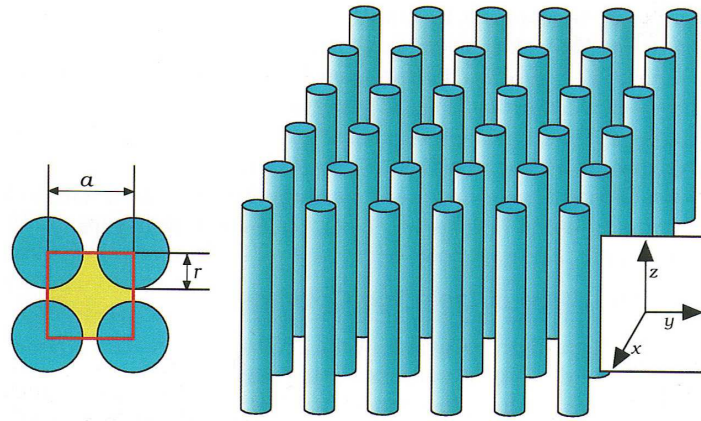
Figure 1.4: Illustration of a two-dimensional PhC of columns of dielectric in air, where 'a' is the lattice constant or periodicity and 'r' is the radius of the columns [12].
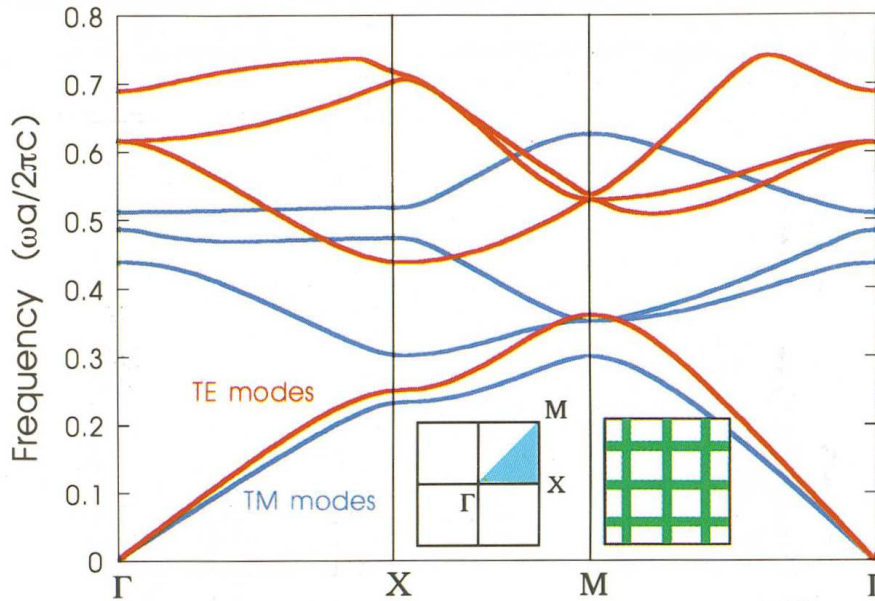
Figure 1.5: Two-dimensional crystal Brillouin zone representation of frequency versus k-space. Γ corresponds to $k = 0$, χ corresponds to $k = \left(\frac{\pi}{a}\right)x$, M corresponds to $k = \left(\frac{\pi}{a}\right)x + \left(\frac{\pi}{a}\right)y$, The inset on the left shows the wave vector with respect to the reciprocal lattice space. The inset on the right shows the reciprocal lattice of the crystal [12].

8
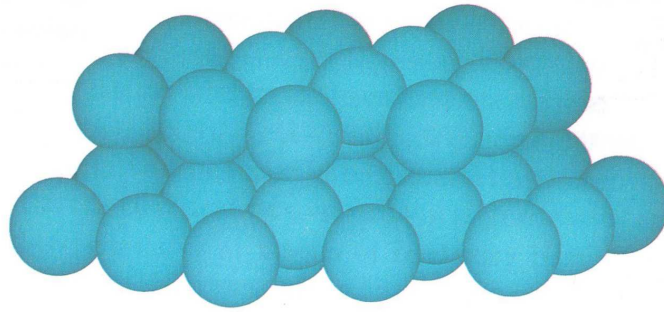
(a)
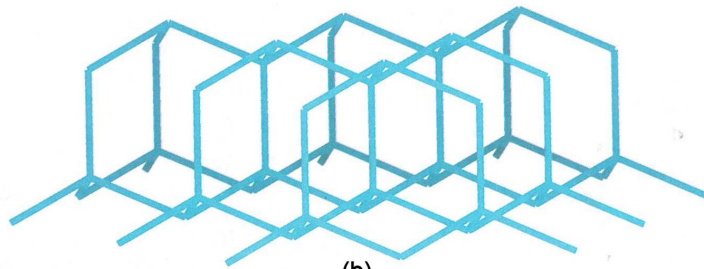
(b)

Figure 1.6:   Two examples of three-dimensional photonic crystal structures. (a) Spheres in a diamond lattice structure and (b) the same structure where the spheres were replaced with rods [12].

[12]
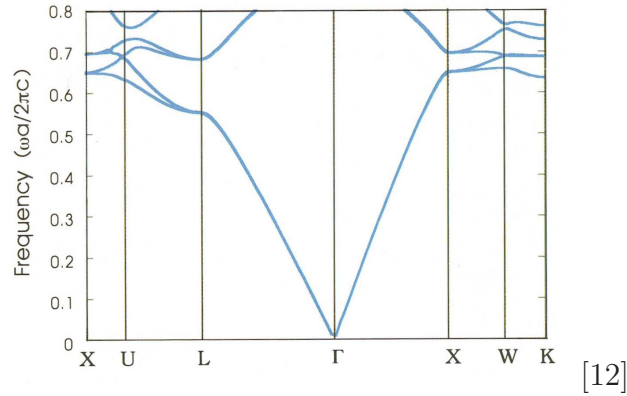
Figure 1.7: Brillouin zone band diagram of a three-dimensional crystal of frequency versus k-space of incorrect geometry and large dielectric contrast of 13 to 1.

provide the same periodic look in all three directions [12]. This figure also shows taking a diamond lattice structure and connecting the points with columns of dielectric [12]. For clarification, it should be noted that the larger the dielectric contrast between the two materials that make up the PhC, the larger the PBG. However, this is not the only requirement for a PBG in a one-, two- or three-dimensional crystal. Figure 1.7 depicts a Brillouin zone for a three-dimensional crystal with a dielectric contrast of 13 to 1; yet, there is no band gap due to the incorrect geometry of the crystal [12]. However, Figure 1.8 shows a three-dimensional crystal structure arranged in interpenetrating diamond lattice spheres that have produced a band gap [12]. Many other two- and three-dimensional crystal structures have and are currently being designed and fabricated.

1.3 Conclusion

It was shown in this chapter how the culmination of works from several great men in history lead to the eventual understanding and creation of PhC's as discovered by Sajeev John and Eli Yablonovitch, the fathers of PhC's. A brief introduction of the theory, explaining PhC's, was presented, illustrating one of the most important facts of PhC's; the requirement for the proper dielectric contrast and periodic geometry of the PhC is detrimental in obtaining a PBG. In the next chapter, an overview of

10
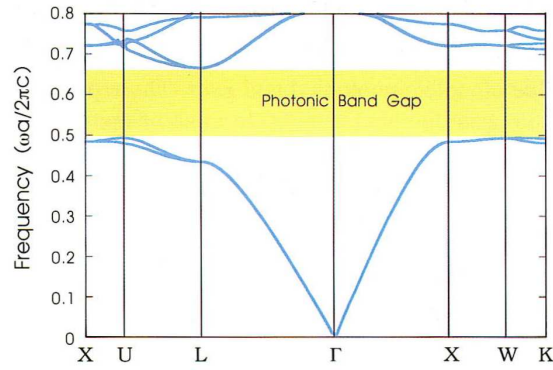
Figure 1.8:   Three-dimensional photonic crystal Bril-
louin zone representation of frequency versus k-space of
a complete PBG for a interpenetrating diamond lattice
of spheres [12].

the different types and fabrication techniques of two- and three-dimensional PhC's is
covered, illustrating the variety of fabrication techniques possible depending on the
wavelength band of the PBG and the application required of the PhC's.

11

II. Background of Two- And Three-Dimensional Photonic Crystal

The utility of PhC's is becoming increasingly popular in all areas of engineering; some applications include telecommunications, lasers, electro-optical computing, sensors and wave guides. As the process to fabricate two-dimensional PhC's with complete in-plane PBG's becomes easier and more industrially available, this need will increase exponentially. Along with this advancement in fabrication will arise the advancement of applications and designs of two- and three-dimensional PhC's. Ultimately, applications involving a three-dimensional PhC's with complete PBG's will be inevitable and required for technological advancement in this field. In order to reach these goals, a building block approach must be accomplished. Two-dimensional PhC's must be able to be fabricated and characterized for a broader range of frequencies in order to heighten the knowledge in this field, thus, paving the way for better three-dimensional PhC's.

In Chapter I, the history and theory of PhC's was discussed, where it was shown that a complete PBG can be created for a specific frequency range depending on the geometry and dielectric contrast of the features in the PhC. This chapter focuses on the considerations of fabrication and testing of PhC's, as well as introducing some recent work in two- and three-dimensional PhC's.

2.1 Fabrication and Characterization of Photonic Crystals

The visible frequency regime has had very little successful experimentation conducted and needs more exploration to further PhC research and design in that area. Fabrication techniques for two-dimensional PhC's vary depending on the size and type of PhC desired. Attempts to fabricate PhC's with complete two- and three-dimensional PBG's have been met with some success. This thesis examines the capabilities to fabricate two-dimensional PhC's with complete PBG's designed for the visible range and to characterize two and three-dimensional PhC's. Different analysis processes can be used to determine the presence of a two- and three-dimensional

12

PBG within a PhC, including: measuring the reflection amplitude of the incident beam on the PhC, measuring the transmittance, recording the specular scattering that occurs incident on the PhC, and obtaining the near field by using scanning optical microscopy, to name a few. For the fabrication techniques used in this experiment, characterization could be accomplished by measuring the transmittance and observing the specular scattering produced by beams of different wavelengths and different angles incident on the PhC's. In order to better understand the results obtained, each device must be modeled and simulated under similar conditions. The use of a commercial FDTD software will be used to model and simulate the designs of this thesis.

One program that is used for this experiment is a two-dimensional triangular structured PhC band solver created by Dr. Joseph Haus of the University of Dayton [8]. This program is listed in Appendix C. Appendix C displays another program that creates gap maps based on the materials' dielectric constants, the periodicity of the triangular columns of air and a specified range of the air column radii. Commercial FDTD software and band-solver software was then applied to model and simulate the initial design. The modeled results would then be compared to the actual test data. There are several companies that create software to evaluate these types of designs. Characteristics and examples of two different commercial softwares will be presented as part of this study.

2.2   Recent Studies of Two-Dimensional PhC's

Two-dimensional PhC's have been successfully fabricated over the past five years and can be produced (depending on wavelength of the PBG) without too much difficulty. Some of the latest work in two-dimensional PhC's is in the realm of tuneable PBG's. Tuning, or changing, the band gap in real time can be accomplished by several methods. One such method would be to change the dielectric constant, and another would be to change the periodic structure. Henry Driel *et al.* have investigated three different ways of creating a tunable two-dimensional PhC [7]. One method was to

fill the periodic columns of air in the silicon substrate with a nematic liquid crystal, and by adjusting the temperature, they were able to shift the PBG. Another method was to optically inject electron-hole pairs into the silicon and change the dielectric constant; approximately 30-nm shifts were recorded. As can be seen by the scanning electron microscope (SEM) image in Figure 2.1, their periodicity is on the order of 1.5 μm which, in turn, produced a PBG around 3-6 μm as illustrated in Figure 2.2. Lastly, by using non-resonant, nonlinear induced optical changes (Kerr effect), they were able to achieve faster tuning effects. By utilizing a pre-patterned electrochemical etching process, they fabricated a triangular lattice of air pores of high geometrical accuracy. Upon applying a temperature change to the substrate, a shift in the band gap was noticed; however, it was not as much as predicted and only affected the air band gap edge (higher mode) with any appreciability. This can be explained due to the fact that it is the air band edge that will change the most since it housed the medium that was changing [7].

Christopher Summers, Georgia Institute of Technology, *et al.* merged the ability to tune both the refractive and dispersion properties [4]. "Super lattice" structures, as they call them, were the result of their work. They took an ordinary two-dimensional column structure aligned in a triangular shape and made the alternating rows of a different dielectric column and resized it to be smaller in diameter (see Figure 2.3). This had the effect of folding the Brillouin zone into a rectangular zone when liquid crystal (LC) is deposited within the lattice structure and by addressing alternate rows (changing the refractive indices). Due to this unique property, depending on the direction of propagation through the crystal, it can be switched from having no PBG to having a PBG, thus either allowing light to flow through or not [4].

Schonbrun *et al.* have demonstrated a technique to change the dielectric of the lattice by stressing the material. A dual set of electrostatic comb actuators were used to effectively stress the material as depicted in Figure 2.4 [24]. What they ended up proving from their testing was an ability to change the refraction angle by up to 75°. Their structure consisted of an array of high index dielectric embedded in a flexi-
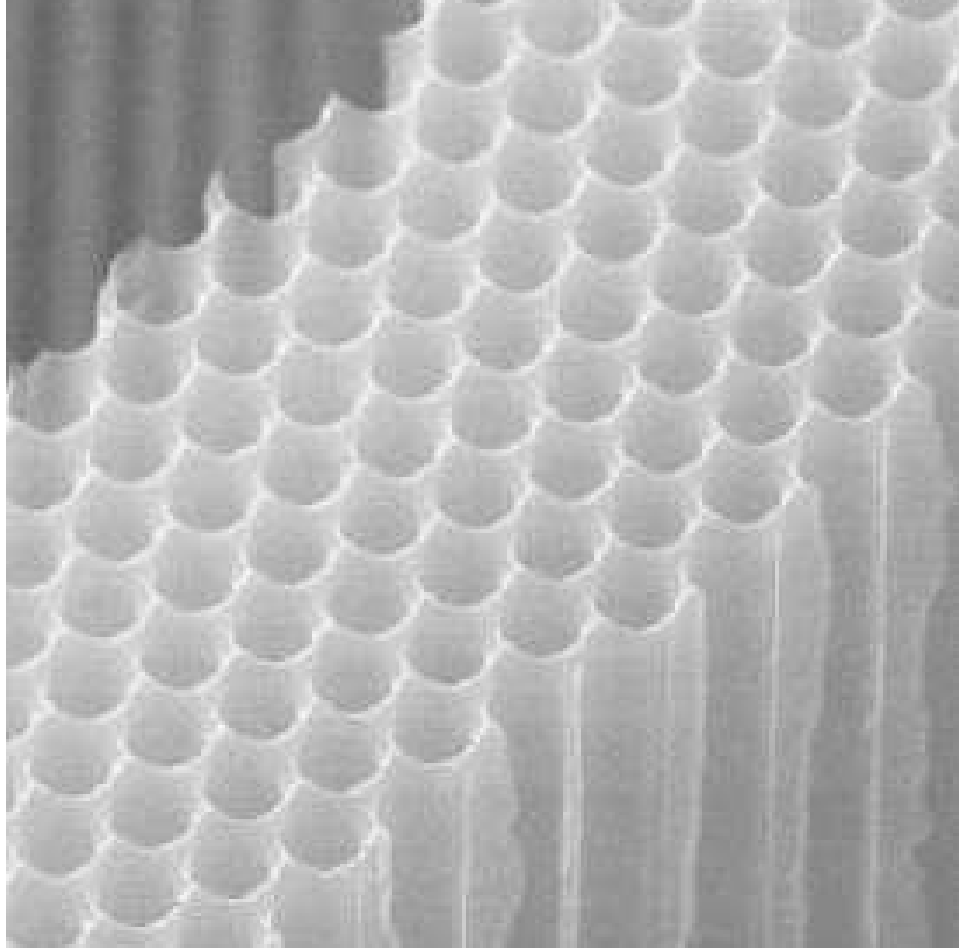
Figure 2.1:   SEM images of a triangular structured two-dimensional PhC with a periodicity of 1.5 μm of air columns in silicon [7].
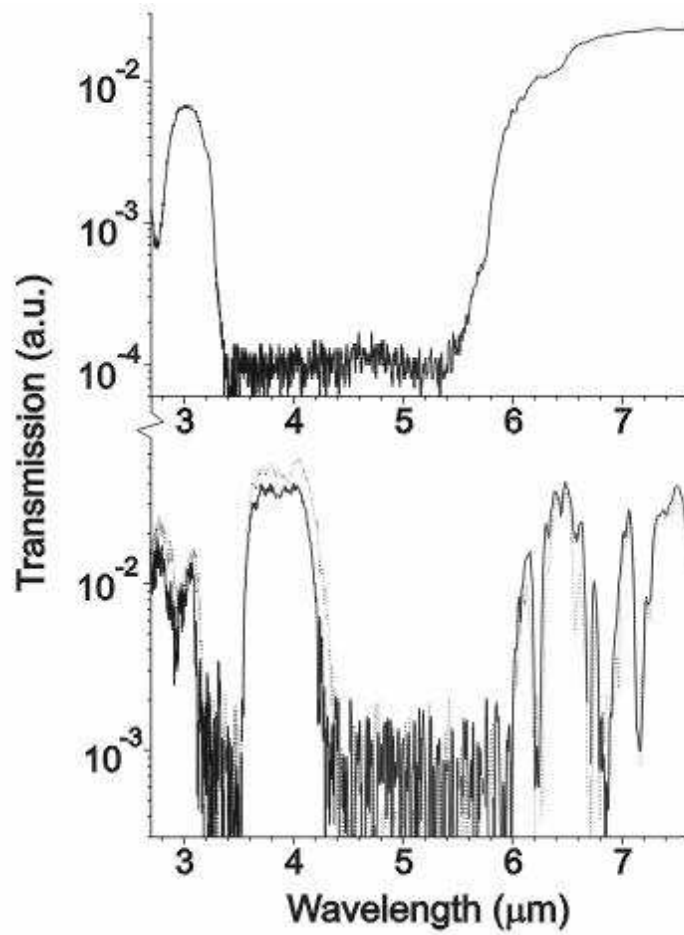
Figure 2.2: (Top) Transmission of H-polarized spectrum prior to infusion of liquid crystal into the PhC of Figure 2.1 and (bottom) after infusion of liquid crystal into the PhC [7].

16
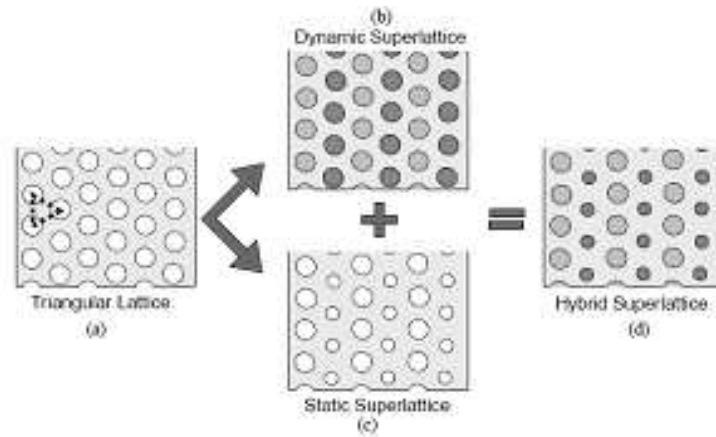
Figure 2.3: Super lattice structures, (a) Triangular lattice, (b) Triangular lattice with rows of different dielectric columns (c) Static Superlattice - alternating column sizes, (d) Hybrid Superlattice - combination of (b) and (c). This picture shows the progression of standard triangular two-dimensional PhC to the new Hybrid Superlattice two-dimensional triangular PhC [4].
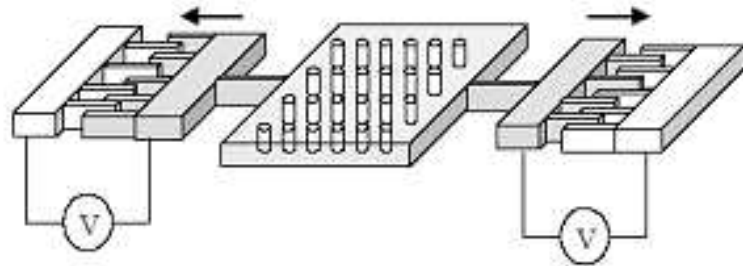
Figure 2.4: MEMS actuators used to stress the polymer PhC [24].

ble polymer film (poly-dimethylsiloxane) and polymide. The microelectromechanical systems (MEMS) electrostatic actuator, stresses the material when activated, causing the crystal structure to change, thus changing the refractive index and the shifting the refractive angle. They were able to achieve up to $75°$ for incident angles between $5°$ and $15°$. A combination of low pressure chemical vapor deposition (LPCVD) and reactive ion etch (RIE) was used to create this structure [24].

The use of specific semiconductor materials for the near infrared wavelengths was reported by S. Noda [15]. These are two-dimensional structures that combine to make three-dimensional crystals. He reports that utilizing either gallium arsenide

17
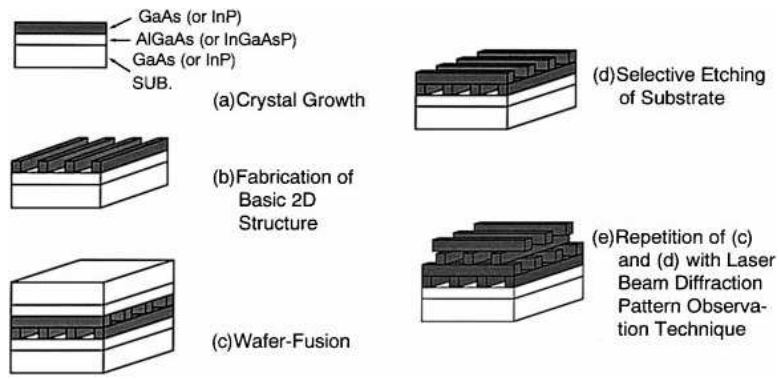
Figure 2.5:   Log-Log stack, a two-dimensional structure used to create a three-dimensional structure [15].

(GaAs) or indium phosphide (InP) will give a band gap in the low infrared range. However, upon review of the process, it would be impractical for mass production. He utilized a GaAs substrate and then grew an etch stop layer. On top of this etch stop layer, he patterned strips using either electron beam lithography or photolithography. The strip's dimensions and the thicknesses of the substrate are determined based upon the wavelength of the desired PBG. The next step is to create the previous steps again separately, then bond the two strips together, etch away the top substrate layers and repeat as many times as desired (see Figure 2.5). Another drawback to this technique is the precision and difficulty of aligning the first and third layers. The resultant band gap is reported to be in the 5-10-μm wavelength range. He reports the ability to make the gap at any near infrared frequency, depending on the geometry of the structure as stated earlier. He was also able to create a band gap of wavelengths from 1-2 μm as well. The attenuation was only about 18 dB. To test his crystal, he utilized a globar lamp monochromator and mercury cadmium telluride (HgCdTe) detector to measure the reflections of the normally incident wave in the <001> direction (see Figure 2.6) [15].

2.3   Recent Studies of Three-Dimensional PhC's

As of late, three-dimensional PhC's are of the most desired, but also the most elusive to obtain. Many different designs have been introduced: log design, square pile

18
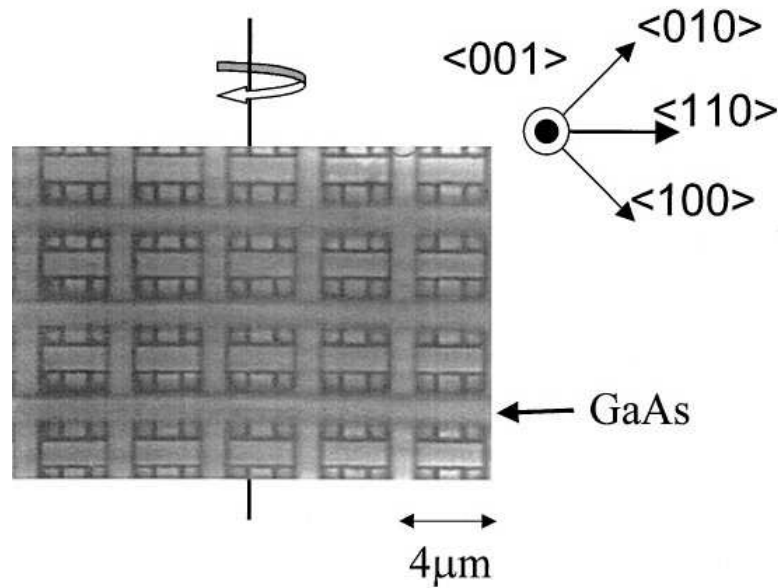
Figure 2.6:　Top view of the Log-Log stack showing the crystal orientation and periodicity of 4 μm [15].

structure, and face centered cubic (fcc) structures [21]; however, the search to discover better and more applicable ways to create three-dimensional PhC's with complete PBG's continues. S. Johnson and J. Joannopoulos designed a structure that gives a complete three-dimensional band gap and is able to be fabricated using planer layer stacks [16]. Their structure (Figure 2.7) is an fcc structure with air cylinders in a dielectric. This crystal has a complete PBG around the 1.55-μm wavelength; when using silicon and air, a 12:1 (dielectric constant of silicon to the dielectric constant of air) ratio which gives a 21% band gap and an 8% gap, is obtained at a ratio of 12:2 ratio of dielectric constants [14]. This structure continues to provide a gap down to a ratio of 4:1 [16]. The percentage band gap is a method of comparing the quality of band gaps of various PhC's. The percentage band gap is calculated by dividing the frequency range of the band gap by its mid-gap frequency.

J. Fleming *et al.* have demonstrated a MEMS fabrication technique that enables a slightly broader range of frequencies [11]. This structure is a face-centered tetragonal structure of 'logs' (see Figure 2.8). This new technique consists of combining a series of molding, filling and chemical mechanical polishing (CMP) steps. This

19
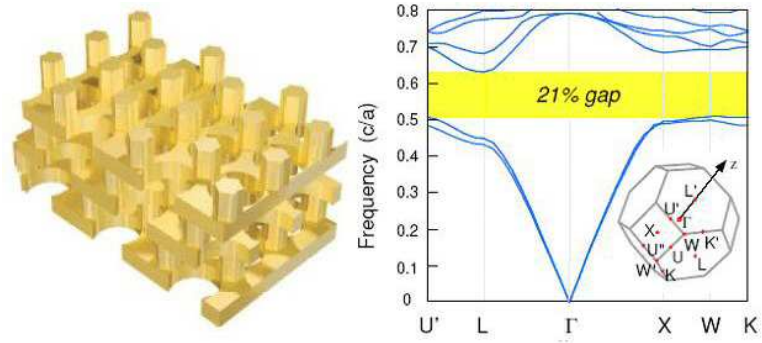
Figure 2.7: Three-dimensional PhC design and associated band diagram [16].
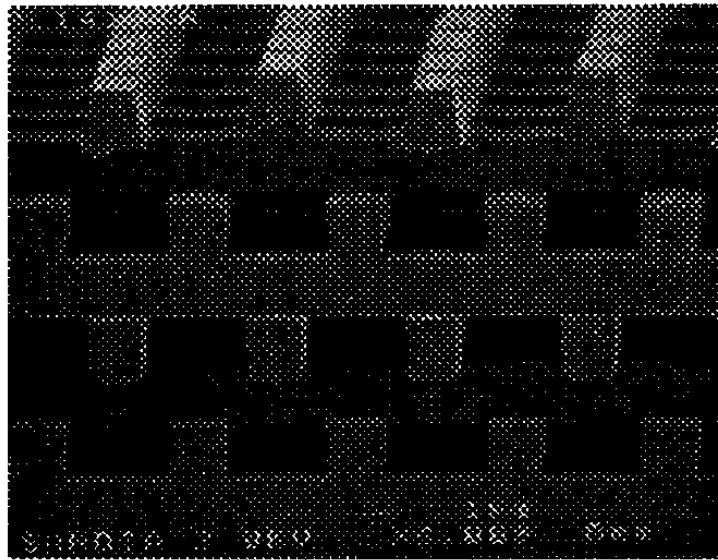
Figure 2.8: SEM view of the log-log stack [11].

process enabled a band gap with the propagation vector normal to the substrate to appear from about 10-14 microns [11]. They accomplished this by patterning parallel rods separated by half the wavelength. The next layer is patterned orthogonal to the first layer, again spaced at half the wavelength, and separated from the first layer by half the wavelength. The third layer is parallel to the first layer and placed halfway between the rods of the first layer, and thus this pattern can continue to be repeated as desired. New fabrication techniques they developed while creating this structure have allowed them to make the features extremely small. The molding, filling and CMP process allowed them to fabricate down to sizes of 1.2 μm. The second process allowed them to fabricate down to 0.18 μm; this was done with a stepper of 0.5-μm resolution and fillet processing, RIE, and CMP. They tested their crystal with an infrared measurement system that had a frequency range from 2.5-25 μm. In order to mitigate the scattering of light off the back of the Si substrate, they polished it to a smoothness of less than 0.3 μm. They extracted the true attenuation of the design by using an identical Si substrate as a base to reference against [11].

Other techniques of three-dimensional fabrications and designs have been created; John *et al.* have proposed another fabrication technique that incorporates interweaving polygonal spiral posts and involves a custom-built deposition system [23]. Utilizing non-coplanar laser beam techniques on a photo-resist, cross-linked polymer rods can be produced according to Campbell *et al.*, but it is extremely complicated [23]. Another new approach to fabricating three-dimensional PBG structures, outlined by Venkataraman *et al.*, uses a single planar etch mask with timing sidewall deep anisotropic RIE etching and an isotropic etch, followed by a sidewall polymer deposition and removal from the bottom of spheres so as to repeat the process (Figures 2.9, 2.10 and 2.12) [23]. The key is the ability to etch sphere-like voids which are sufficiently large so as to perforate into the spheres next to them. This would be analogous to the two-dimensional case of having columns of either air or dielectric connected by a beam in order to take advantage of both the TM and TE gaps. A polymer is deposited to protect those spheres from further etching; the polymer is

21
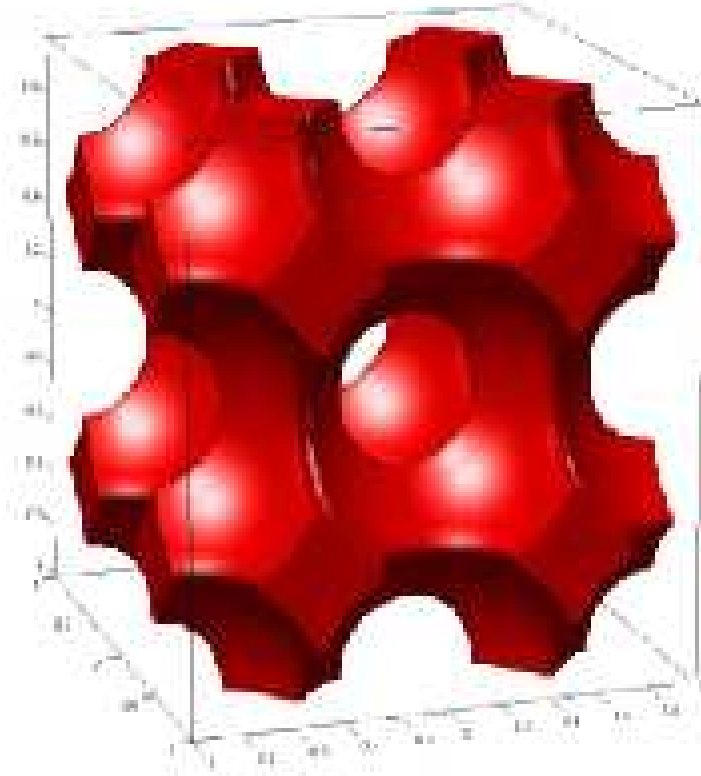
Figure 2.9: Three-dimensional PhC computer design of novel methodology [23].

able to be removed from the bottom of that layer of spheres by "smash" etching, allowing them to continue etching the next layer of spheres, and then the cycle can be repeated. Their calculations lead them to believe that they will create a complete three-dimensional PBG with this design [23].

Miklyaev *et al.* improves on the holographic technique of using directed laser beams that form an interference pattern in the photo-resist, causing nulls and peaks in intensity whose structure is in the form of an fcc lattice [26]. The places within this interference structure where the intensity is high causes the photo-resist to effectively be exposed. This capability allowed them to produce lattice features down to 550 nm. Figures 2.11 and 2.13 depict an SEM image of a structure created by Miklyaev *et al.* and the band gap with the transmission of this structure, respectively. They used optical spectroscopy with a spot size of 100 μm to test the structure [26].

22

(1) Apply etch mask layer   (2) Pattern etch mask

(3) Etch top layer of voids   (4) Passivate

(5) Anisotropic "smash" etch   (6) Etch 2nd layer of voids

(7) Passivate   (8) Anisotropic "smash" etch
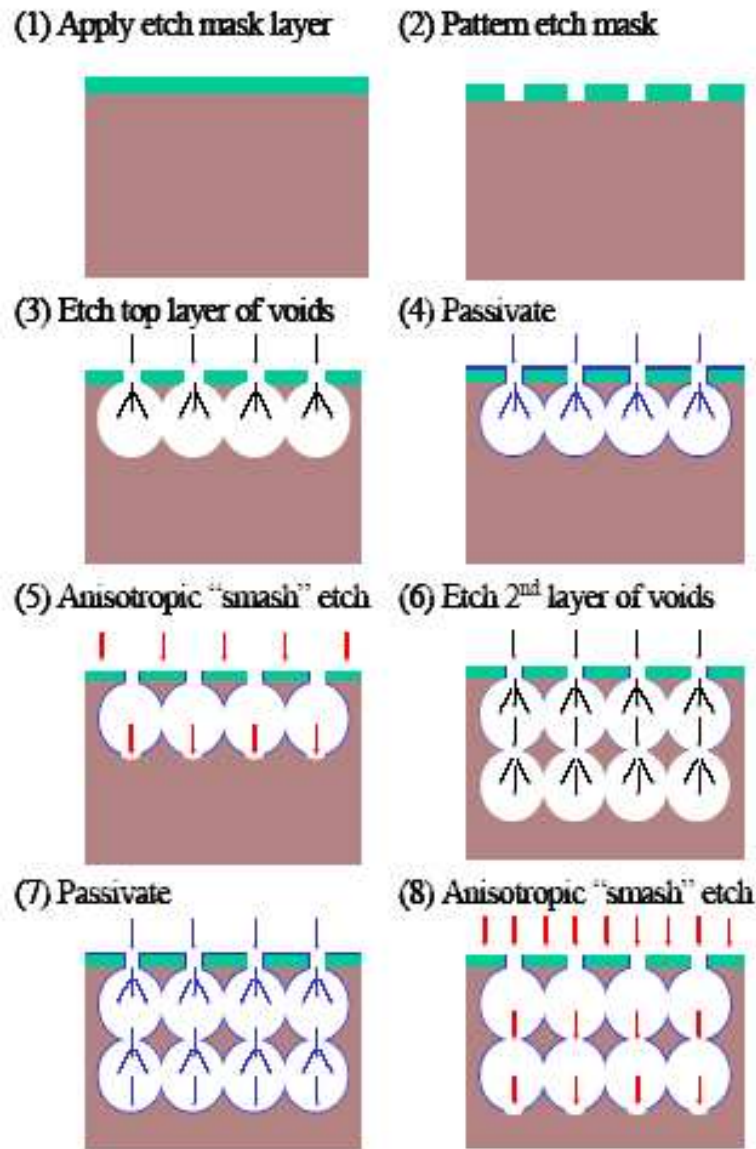
Figure 2.10:   Three-dimensional PhC fabrication technique of novel methodology. Steps one through eight describe the etching process of this novel fabrication technique [23].

23
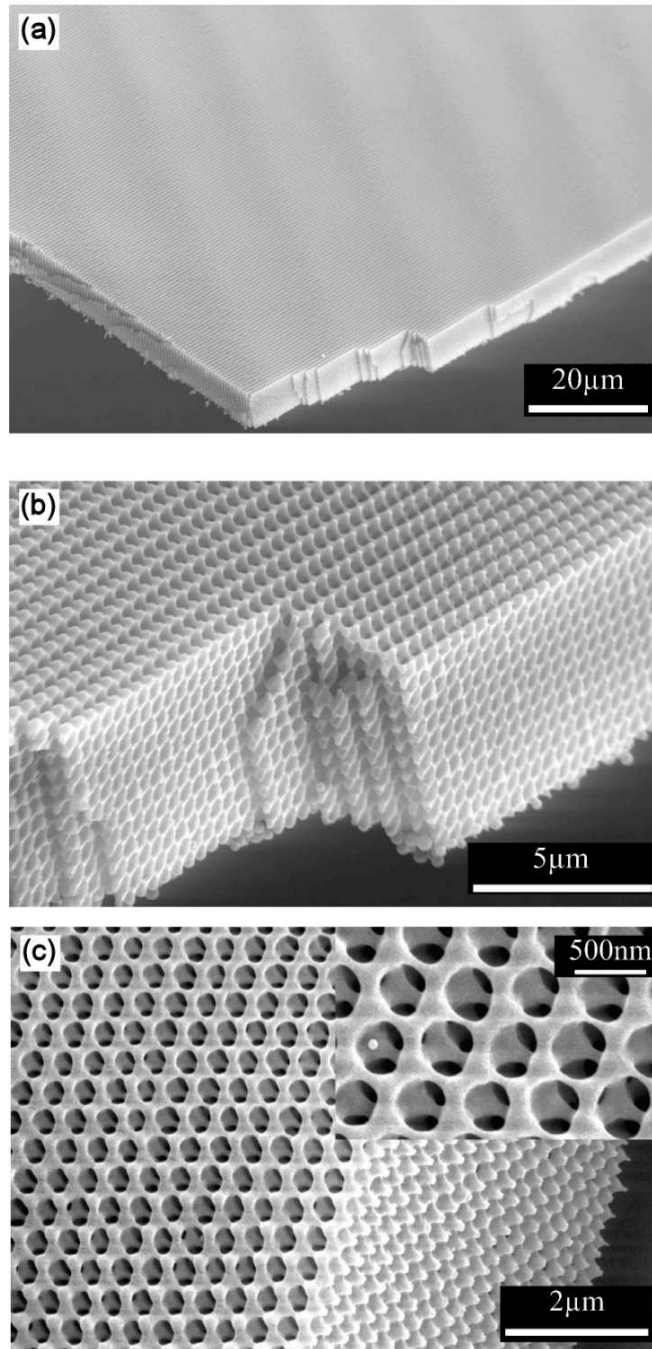
Figure 2.11: SEM image of sample produced with holographic techniques in photo-resist, where (a) shows the structure with a 20-μm scale, (b) shows the structure with a 5-μm scale and (c) shows the structure with a 2-μm scale and an inserted 500-nm scale [26].
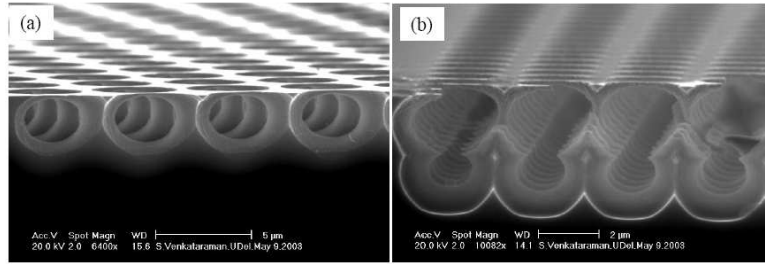
Figure 2.12:   SEM image of single-cell and two-layer
PhC, using method outlined in Figure 2.10. (a) Shows
the results of the first four steps in the novel fabrication
technique of Figure 2.10. (b) Shows the results of second
four steps in the novel fabrication technique of Figure
2.10 [23].
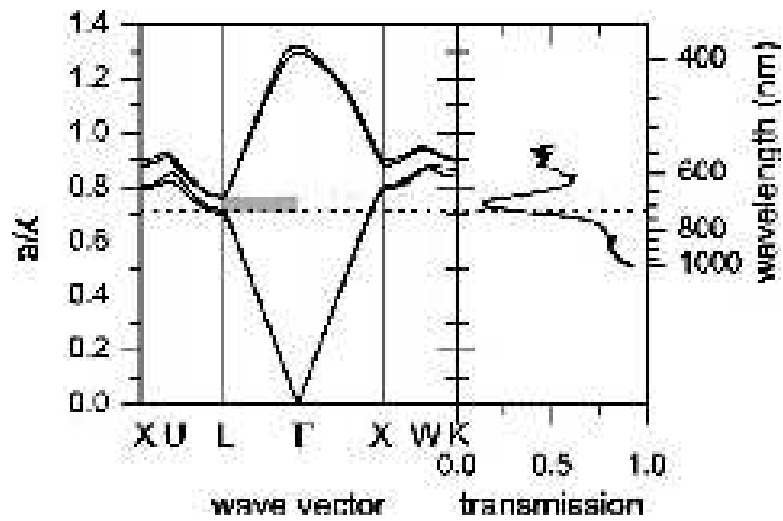
Figure 2.13:   Band gap and transmission spectrum of
holographic sample of Figure 2.11 [26].
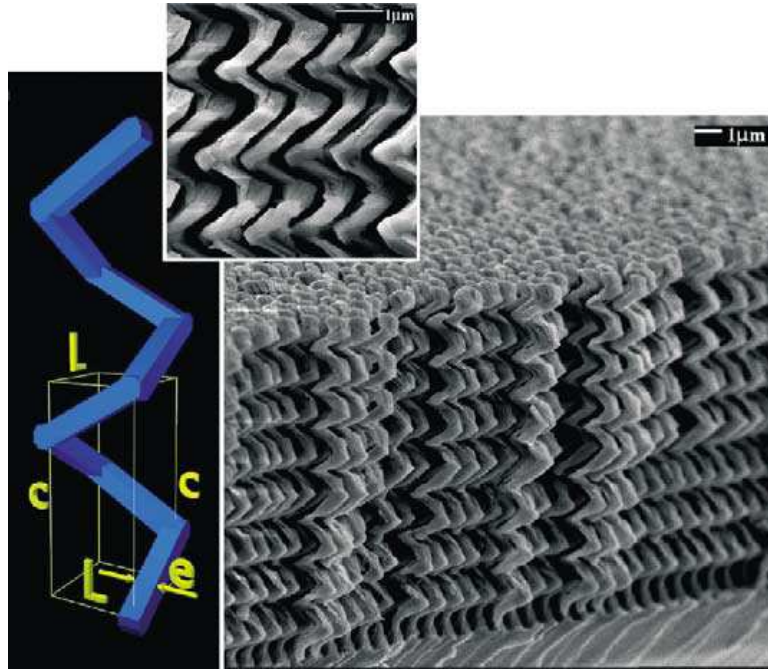
Figure 2.14:   SEM image of the sample fabricated with
GLAD. The left is a computer generation of the individ-
ual structure and the inset is a magnified section of the
sample [19].

A new technique has been introduced by Kennedy *et al.* that incorporates fabri-
cating a three-dimensional PhC using a thin-film deposition process that allows large
PBG's to be produced in a one-step process. The technique, glancing angle deposition
or GLAD, is outlined in their paper [19]. Figure 2.14 is an SEM image along with
a computer generated structure of the device they created using GLAD. They used
a Fourier transform infrared (FTIR) spectrometer in reflection mode to measure the
properties of this design. Figure 2.15 is a graph of the reflectance spectrum at normal
incidence, and the inset is a plot of the reflectivity at shorter wavelengths and was
accomplished using a Perkin-Elmer Lambda 900 spectrophotometer and an optical
system with a numerical aperture of 0.6 [19].

Auto-cloning is one technique that has recently shown some promise to the
creation of larger scale three-dimensional PhC's. This type of three-dimensional
PhC is fabricated by a combination of sputter-deposition and sputter-etching simu-
taneously [17]. This process requires a two-dimensional PhC as substrate on which

26
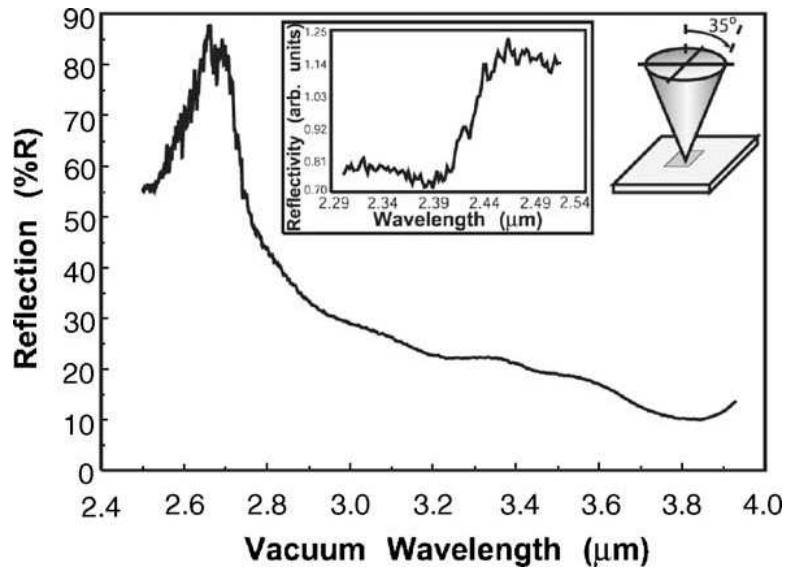
Figure 2.15: Reflectance spectrum at normal incidence of the GLAD fabricated sample in Figure 2.14 [19].
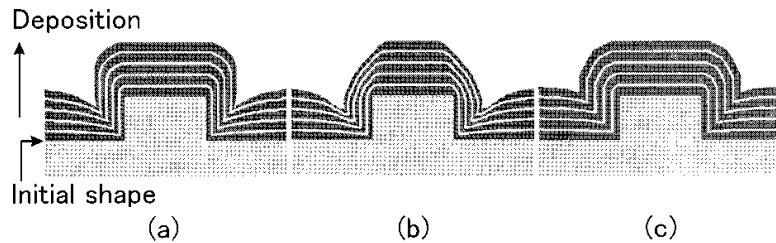
Figure 2.16: Pictorial of the auto-cloning evolution showing the conformal nature created [17].

to be sputtered. As the normal sputtering process is typically non-conformal, with the radio frequency (RF) etching process occurring simultaneously, it creates a more conformal sputtering process as can be seen in Figure 2.16. Auto-cloning does not require a perfect two-dimensional structure; imperfections are often fixed after a couple of layers of sputtering so as to match the rest of the structure's dimensions. Figure 2.17 is an SEM image of a two-dimensional grating that has been auto-cloned. After approximately four to five periods of deposition, the structure is then resolved, and that periodicity holds for the rest of the required deposition layers [17].
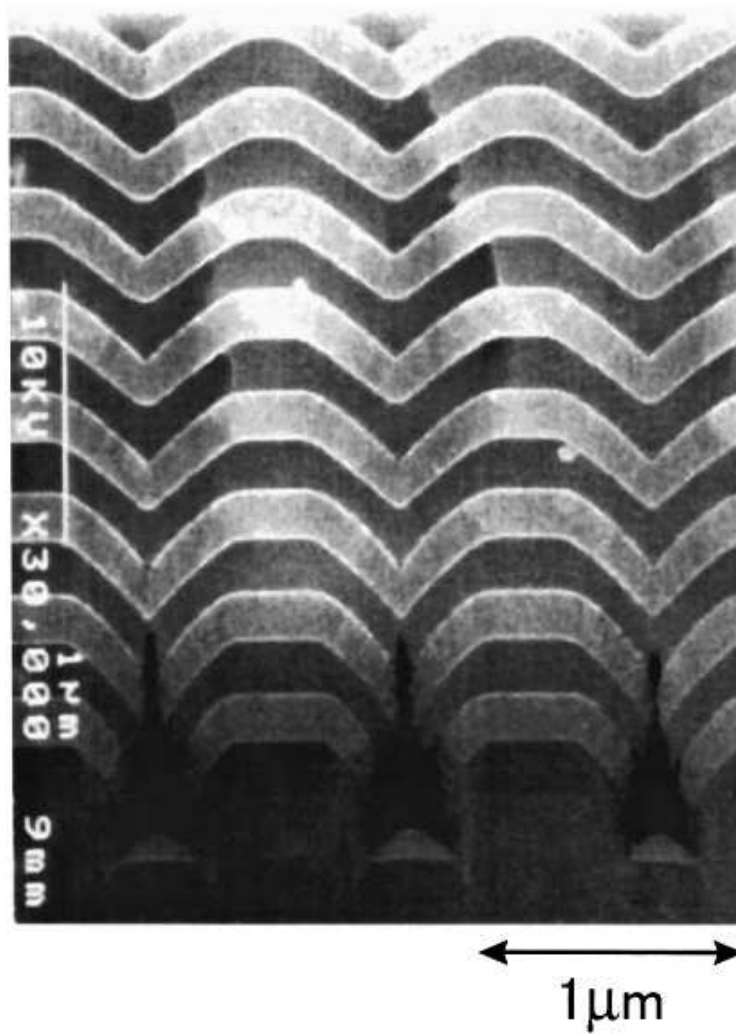
Figure 2.17: SEM image of the auto-cloning process on a two-dimensional grating [17].

28

2.4   Conclusion

This chapter looked at the different types of PhC's and the various fabrication techniques used to create two- and three-dimensional PhC's based on their frequency range of the PBG. In order to accomplish the ultimate goal for the PhC field (three-dimensional PhC's with complete PBG's for frequency range of the desired application), a building block approach must be accomplished. Based on the fabrication techniques accomplished to date, this thesis will focus on expanding this PhC knowledge base by examining some fabrication techniques to create a two-dimensional PhC with a PBG in the visible range. To aid in the fabrication process, FDTD software, used to model and simulate various PhC designs, should be used to verify the designs created before the fabrication process. The next chapter will evaluate two FDTD softwares for their use as sufficient modeling and simulation software of PhC's.

III. Two- and Three-Dimensional Photonic Crystal Modeling Tools

The utility to model and simulate a PhC design prior to attempting fabrication is paramount. The validation of a specific PhC design for a specific PBG prevents wasted time and funds in fabricating a PhC that may or may not be designed properly. Also, the use of FDTD software for modeling PhC's allows for more precise designs based on the application desired, which can be simulated with the software.

Chapters I and II covered the history, theory of PhC's and some examples of current two- and three-dimensional PhC structures with differing fabrication techniques, pointing out the fact that the most important attributes to creating a PhC are the dielectric contrast, geometric structure and the fabrication technique based on the size of the PhC structure desired. This chapter evaluates two FDTD softwares used to design and model PhC's. Modeling the specific PhC design is a necessary step prior to the fabrication stage.

3.1 Modeling and Simulation Software Attributes

The two different softwares used were Optiwave's OptiFDTD and Photon Design's Crystalwave. These commercial softwares solve the Maxwell wave equations problem by using the FDTD method. This is a direct numerical solution of the time-dependent Maxwell curl equations. These softwares have a graphical interface, allowing for ease of design, simulation and analysis. They contain many analysis tools, such as plane wave expansion (PWE) band solver, Fourier analysis, and graphical representation of the TE and TM modes as they propagate through the crystal. A few basic properties similar to both programs will be demonstrated using Optiwave's OptiFDTD software. Figure 3.1 is a graphical user interface (GUI) representation of a simple PBG structure that is one row by six columns of dielectric cylinders (refractive index 3.1) in air. The radius of the cylinder is 0.2 μm and the separation (center to center) is 1 μm. This crystal will be evaluated by an input wave from the left of 1.9-μm wavelength Gaussian modulated continuous wave, simulating a two-dimensional

www.manaraa.com
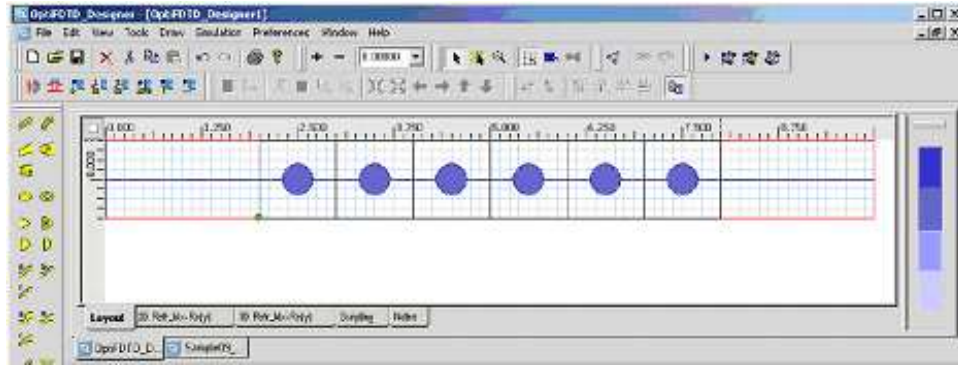
Figure 3.1: Single PhC row of cylindrical columns created with Opti-
wave.
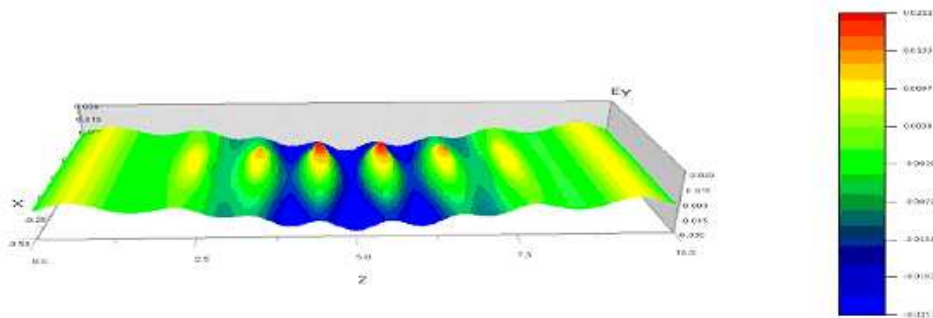
Figure 3.2: Depiction of the E_y wave of the PhC columns of Figure
3.1.

situation and analyzing the TE component. Figure 3.2 shows the E_y (electric field in
the y direction) simulated wave propagation.

Another analysis tool is the frequency analyzer. Here, the transmittance and
reflectance of the simulated wave is normalized to the input plane (Figure 3.3). This
next example is how Optiwave simulates a defect in a PhC with a PBG. When prop-
erly designed, the PhC is almost like a perfect reflector. When the defect is arranged
in a line, it can be used as a channel to guide the trapped wave (Figure 3.4). An
important note is that this is much like a fiber optic cable except sharp bends (*i.e.*,
90° or better) can be made and have little to no loss, unlike that of fiber optics. From
Figure 3.4, it is shown that the defect is the absence of the periodic dielectric columns.
The columns have a radius of 0.3 μm, and are separated by 1 μm. They are arranged
in a two-dimensional hexagonal pattern. This is simulated using a 1.9-μm Gaussian

31
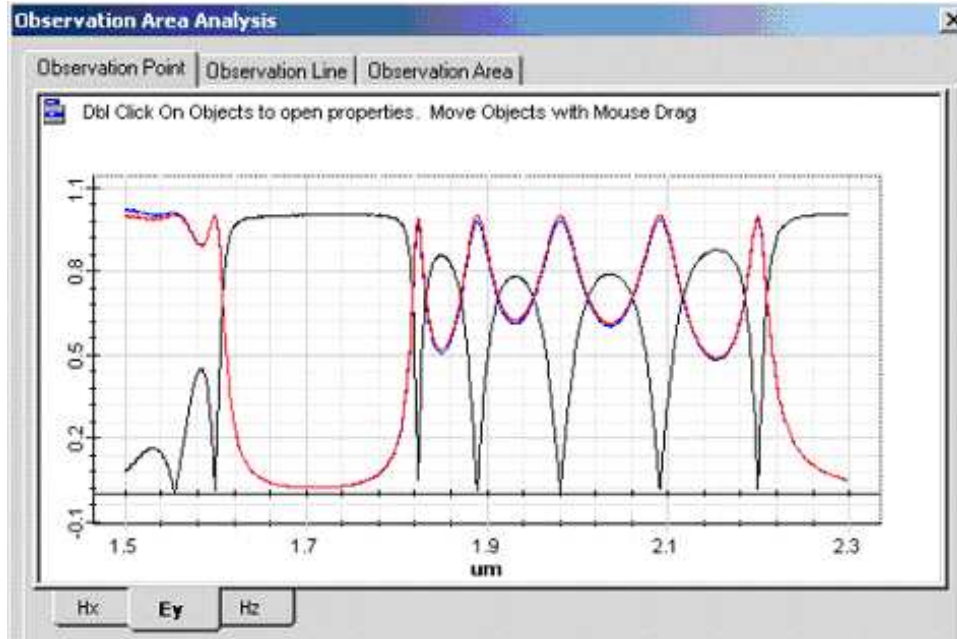
Figure 3.3: Fourier transform of the PhC columns depicted in Figure 3.1, showing the incident wave (black line) and the transmitted wave (red line).

modulated continuous wave in two dimensions with respect to the TE wave. Figure 3.5 displays the normalized frequency analysis of this design. For the frequency of interest, it has a wide bandwidth that almost completely transmits through with little loss.

The resulting Poynting vector can be seen in Figure 3.6, along with the E_y field. This was a sample of what OptiFDTD can do in two-dimensions. Optiwave's interface relies more on the ability to construct the lattice, based on mathematical formulas, which allows for an extremely versatile capability to construct any lattice desired. It also requires a little more advanced knowledge of the mathematical formulas to implement more complicated designs. Optiwave's PWE is extremely useful and easy to implement. Optiwave also features the ability to design graded indices of atoms and allowances for doping in the material.

Crystalwave has similar capabilities. The GUI is very user friendly; however, this may present some limitations in the complexity of design allowed to be created. Crystalwave, when modeled for a similar situations as Optiwave, provides similar re-

32
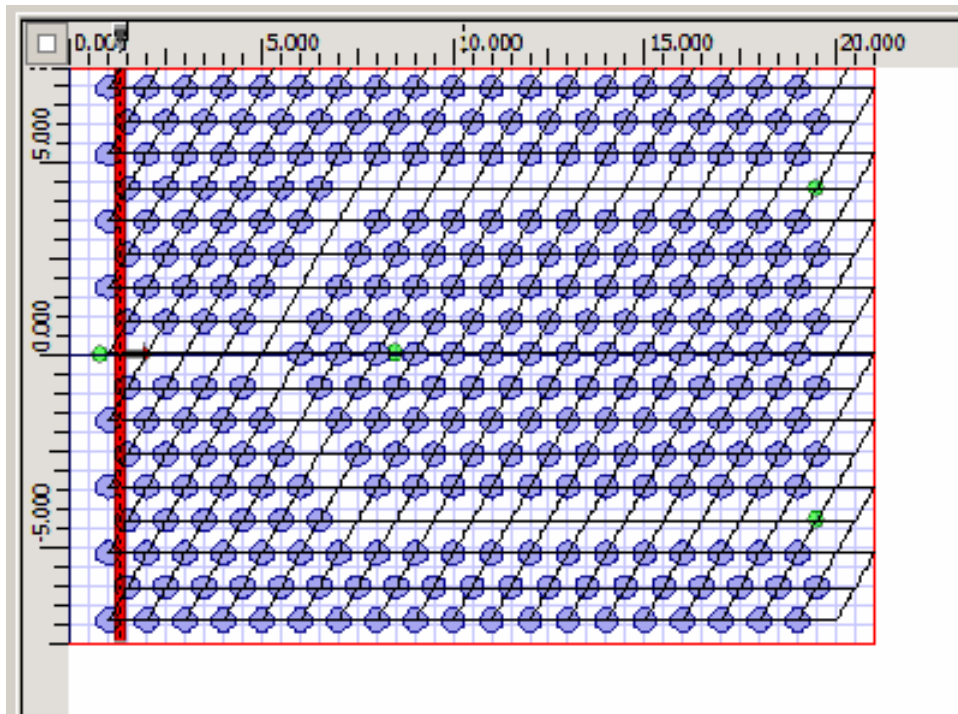
Figure 3.4:   Top view of dielectric crystal with defect channel created in Optiwave.
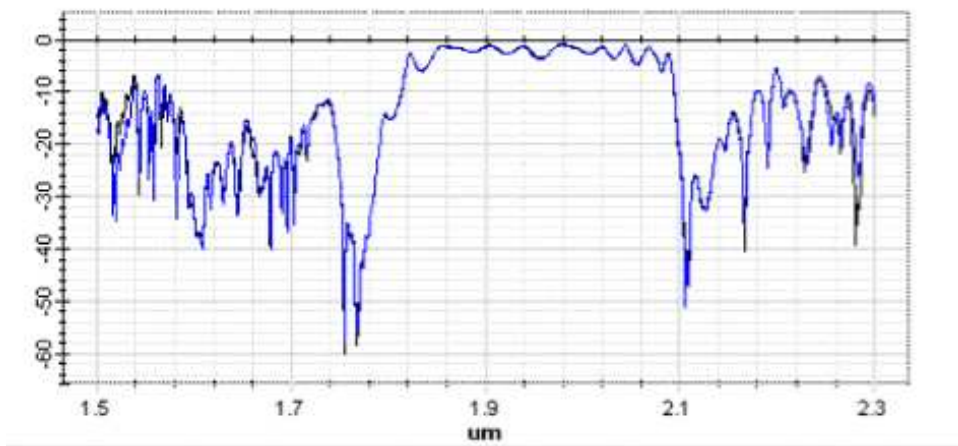
Figure 3.5:   Frequency component of the PBG of the Y-split channel depicted in Figure 3.4.

33
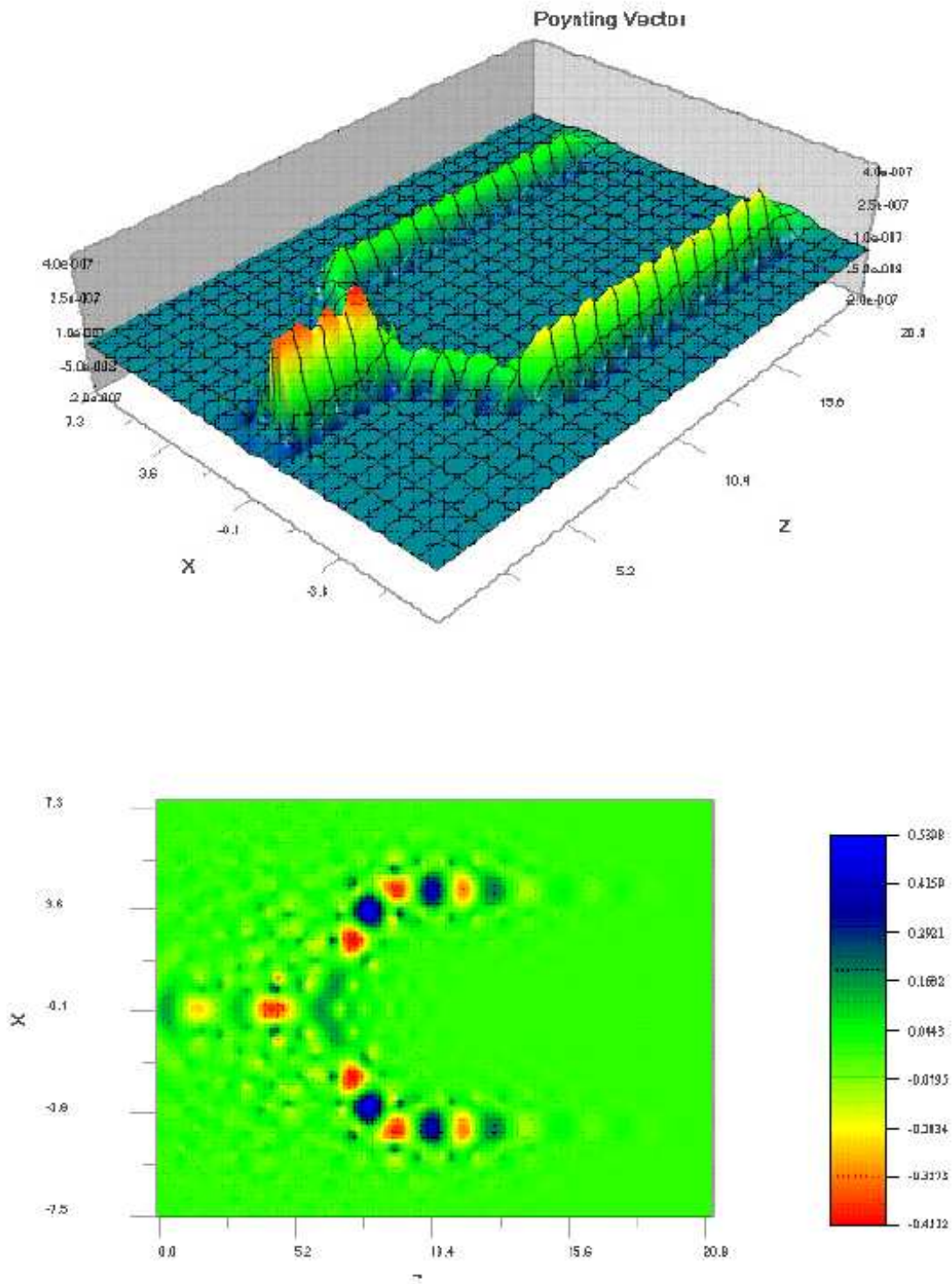
Figure 3.6: Poynting vector (top) and E_y field (bottom) of Y-split channel depicted in Figure 3.4.

34
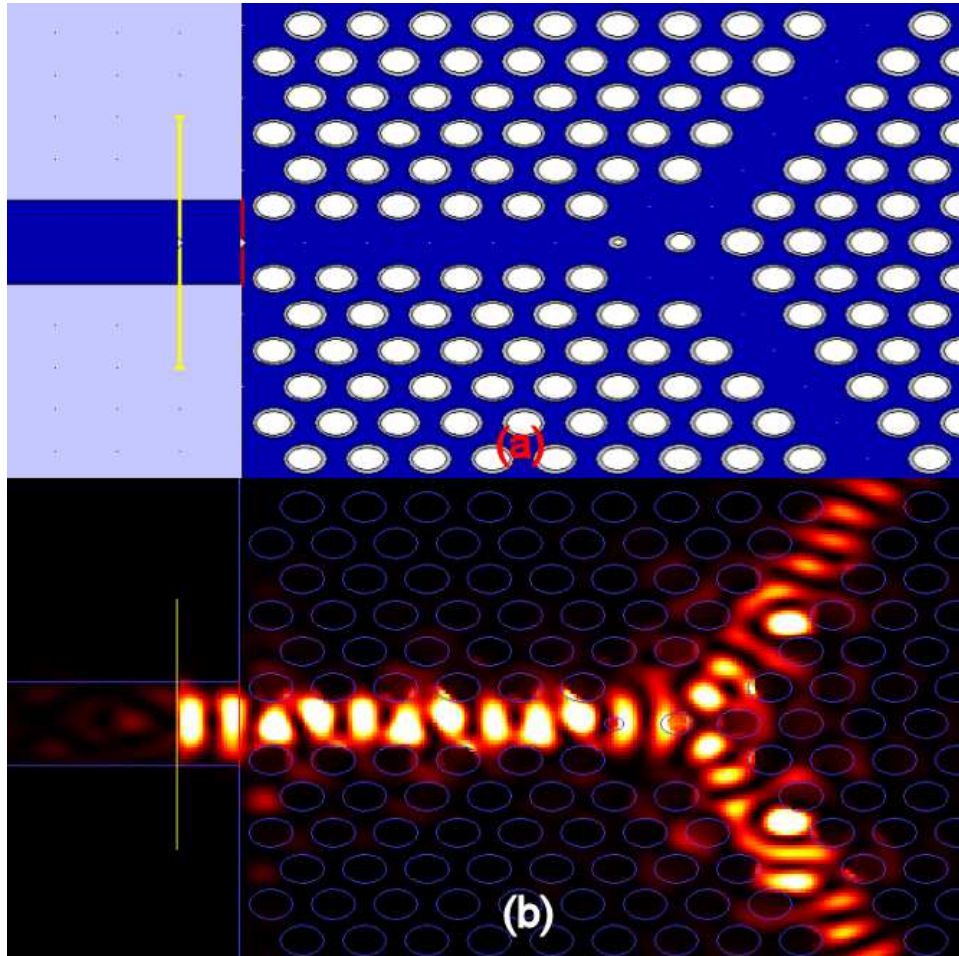
Figure 3.7: (a) Graphical user interface for the Y-design in Crystal-wave software, showing the oxidation layer around the columns. (b) Intensity pattern for the Y-design of (a).

sults. Figure 3.7 (a) shows the waveguided Y-split using a PhC; note the Y-split has been optimized at the split which accounts for the extra off-sized columns in the Y-split. The intensity pattern of this design in Crystalwave is modeled in Figure 3.7 (b).

Incorporated into Crystalwave is a common occurrence, oxidation. Crystal-wave allows for a wall layer to be modeled on any atom structure easily; to do the same in OptiFDTD can be done, but not as easily. This wall layer could be used to account for oxidation that occurs unavoidably in most situations. Crystalwave is more confusing when trying to add multiple atoms to a region. Crystalwave incorporates

35

an interesting feature, allowing the side cut away view to be pictured anywhere in the structure; whereas OptiFDTD allows a three-dimensional look at the entire structure that can be rotated about all three axes. Crystalwave allows not only the FDTD analysis in two-dimensions for a two-dimensional structure, but also in three-dimensions for a two-dimensional structure. This allowance accounts for the layer thickness of the structure, instead of assuming infinite layer thickness. Crystalwave does not have a correctly operating three-dimensional band solver. Another unique feature that Crystalwave has is an optimization function. This feature allows the computer to solve for the best size and placement of designated atoms based on the user's desired results of the PhC and the inputs of the dependent and independent variables, which is somewhat confusing and requires some knowledge in C++ programming. The K-vector of the band diagram can be easily manipulated in Crystalwave (*i.e.*, drag and drop feature) as compared to Optiwave (which has a more complex method of doing the same thing), allowing for any wavevector angle to be evaluated and not just the standard wavevectors of high periodicity. Also, Crystalwave allows for a choice of graphing techniques of the band diagrams where the y-value can represent different characteristics (*i.e.*, frequency, normalized wavelength, *etc.*) Optiwave has a fixed band diagram y-axis (normalized frequency). Crystalwave currently has no way of propagating a mode in the y-direction. However, this can be simulated by using a Gaussian mode exciter. To demonstrate this property, the following example is shown.

The best way to test this feature is to build a vertical cavity surface emitting laser (VSCEL) in the modeling software. Figure 3.8 shows a VSCEL design that incorporates a two-dimensional PhC in the gain medium for the lateral confinement. This PhC and VCSEL is designed for the wavelength of 632.8 nm. In order to make this design easy to model, the distributed Bragg reflector (DBR) layers are designed to be of optimum refractive index to facilitate minimum layers to achieve a 0.999 reflectance at the bottom of the gain medium and a 0.9 reflectance at the top of the gain medium. The top of the gain medium will also act as a DBR for the waveguided layer. The top of the waveguided layer has a DBR with a reflectance of 0.999, also.

36
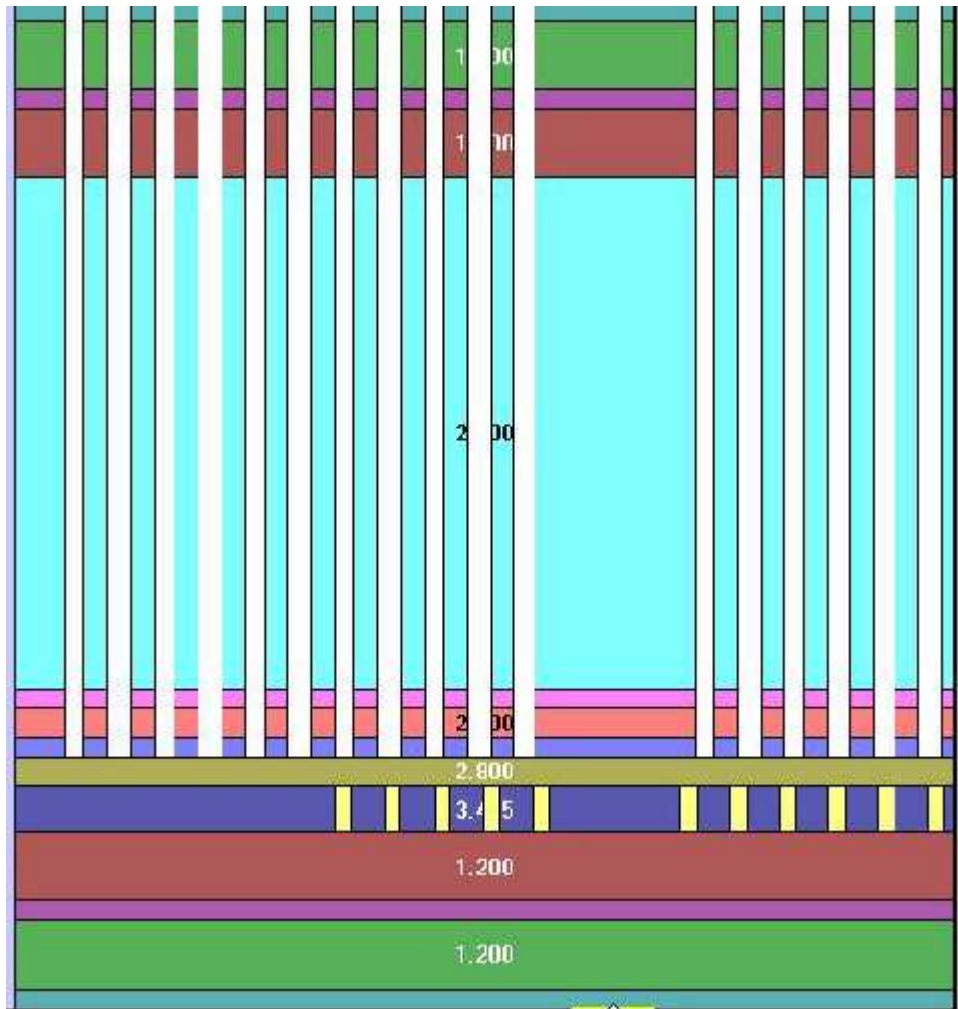
Figure 3.8:   Side view of the VCSEL and the DBR layers and the PhC's used for horizontal confinement.

37
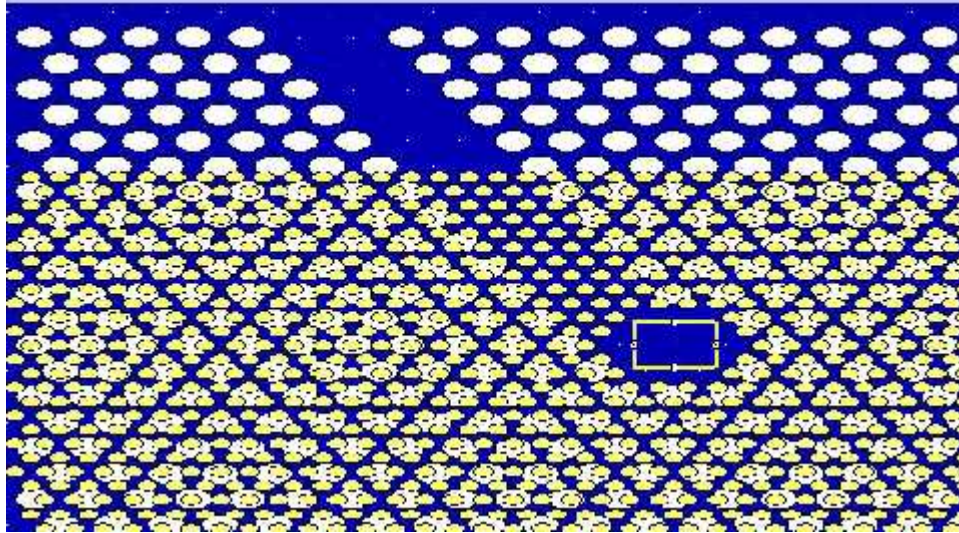
Figure 3.9: Top-down view of the VCSEL design in the GUI of Crystalwave; the different sized columns are the different PhC's of the waveguide and gain layers depicted in Figure 3.8.

Both two-dimensional PhC's in Figure 3.8 are set to confine the wave laterally at a wavelength of 632.8 nm; the reason that the two PhC's do not seem to have the same periodicity is due to the different dielectrics of the gain and waveguide materials. The waveguide layer has an index of 2.0, where the gain medium is aluminum gallium arsenide (AlGaAs) with an index of 3.455. Figure 3.9 shows the top-down GUI view of the VCSEL cavity. The physical layer view is seen in Figure 3.10 containing the corresponding physical (not optical) thickness required and index necessary to obtain the DBR and VCSEL situation described above. The waveguide layer has a defect channel built into it, which can more readily be seen in Figure 3.9. This waveguide channel is a defect line of missing columns; the defect line was placed so that the coupled lateral mode, due to the resonance (standing wave) in the y-direction, is lined up with the coupled mode.

Figure 3.11 (a) is the intensity of the mode as it propagates down the waveguide channel. Figure 3.11 shows the E_z (b) and the E_x (c) fields, respectively, propagating down the waveguide channel. A reference probe and a transmitted probe were placed at the opening of the waveguide from the cavity and at the opposite end, respectively. Based on these probes, the following data was able to be assessed. Figure 3.12 shows

38

Figure 3.10: Physical layers indicating the thickness in μm and refractive index of the VCSEL model in Crystalwave.
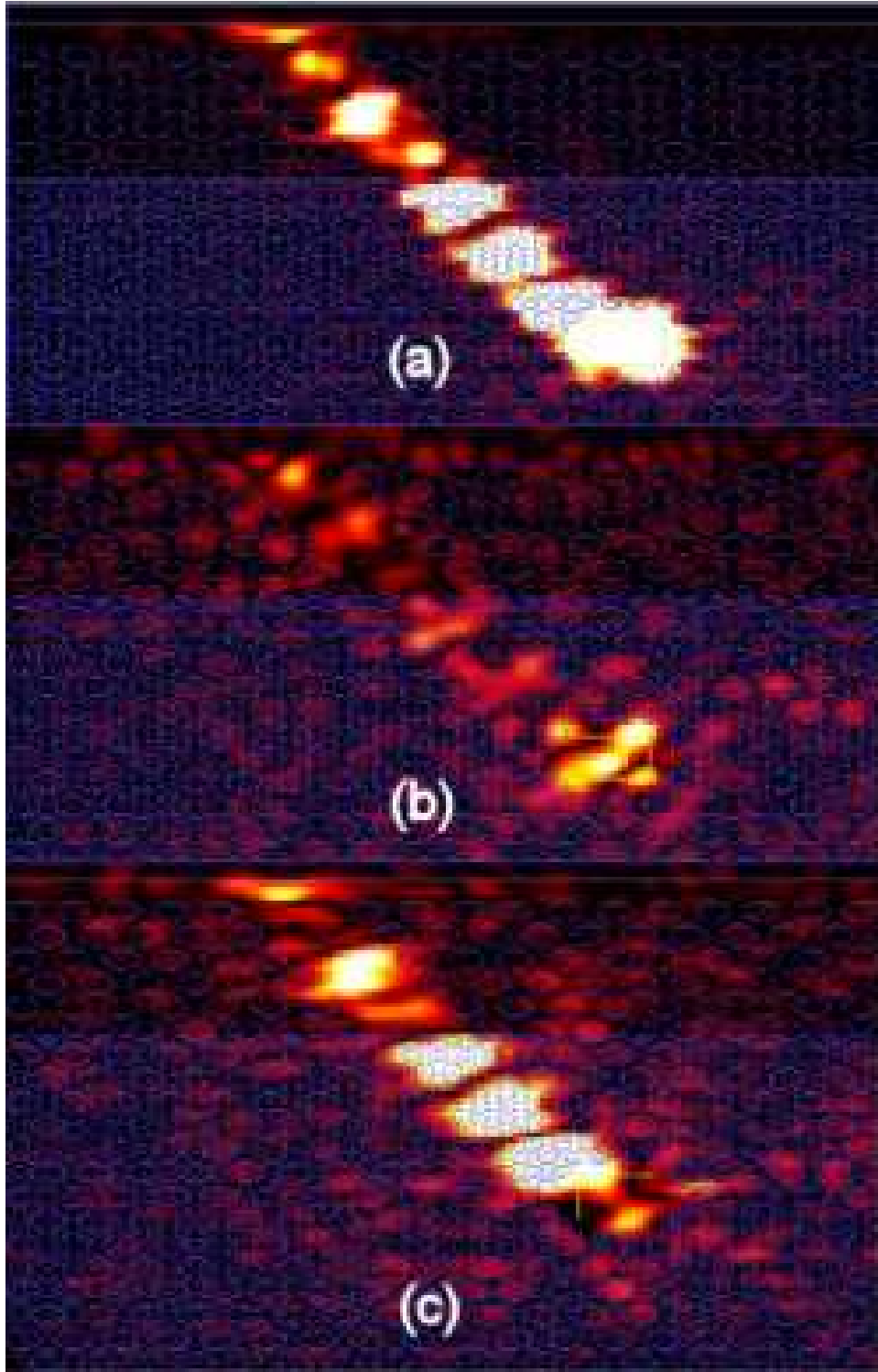
Figure 3.11: (a) Intensity, (b) E_z field and (c) E_x field of the VCSEL simulation in Crystalwave of the coupled wave propagated down the waveguide.

40
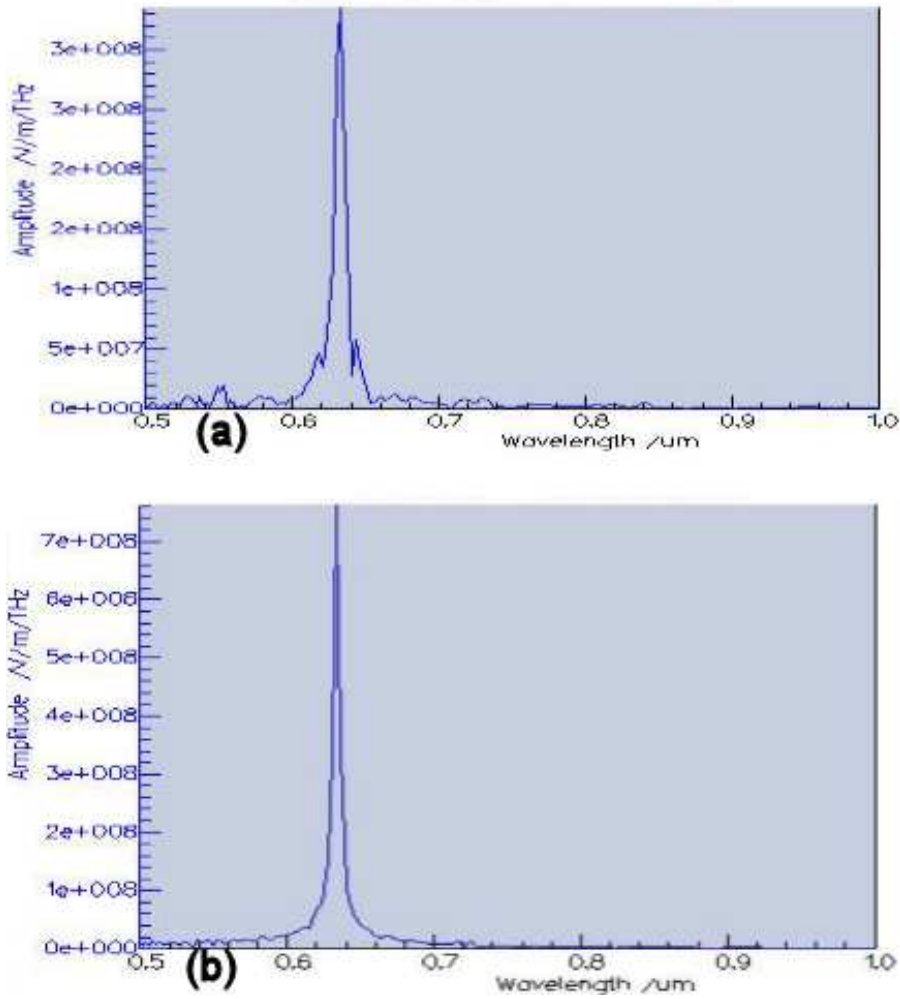
Figure 3.12: E_x field of VCSEL simulation in Crystalwave showing (a) the reference probe data and (b) the transmitted probe data.

the reference and transmitted data of the E_x field for the waveguide channel, and Figure 3.13 shows the net flux data of the E_x field for the waveguide channel. A three-dimensional image of the intensity in the waveguide layer is shown in Figure 3.14. Figure 3.15 is an image of the confinement due to the PhC in the gain medium of this VCSEL design.

In order to determine if the loss in the waveguide channel is average, a test design was set up to model the waveguide layer as it was designed in the VCSEL simulation. A mode exciter was placed in the waveguide layer at the opening of the channel and pointed down the channel. Again, probes were placed at the beginning

41
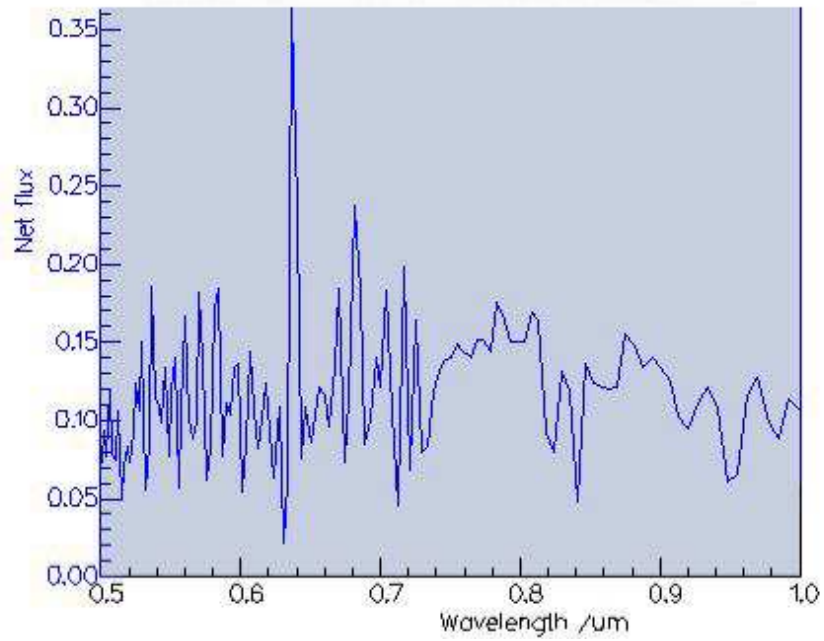
Figure 3.13: E_x field of VCSEL simulation in Crystalwave showing the net flux of the transmitted flux referenced to the reference flux.
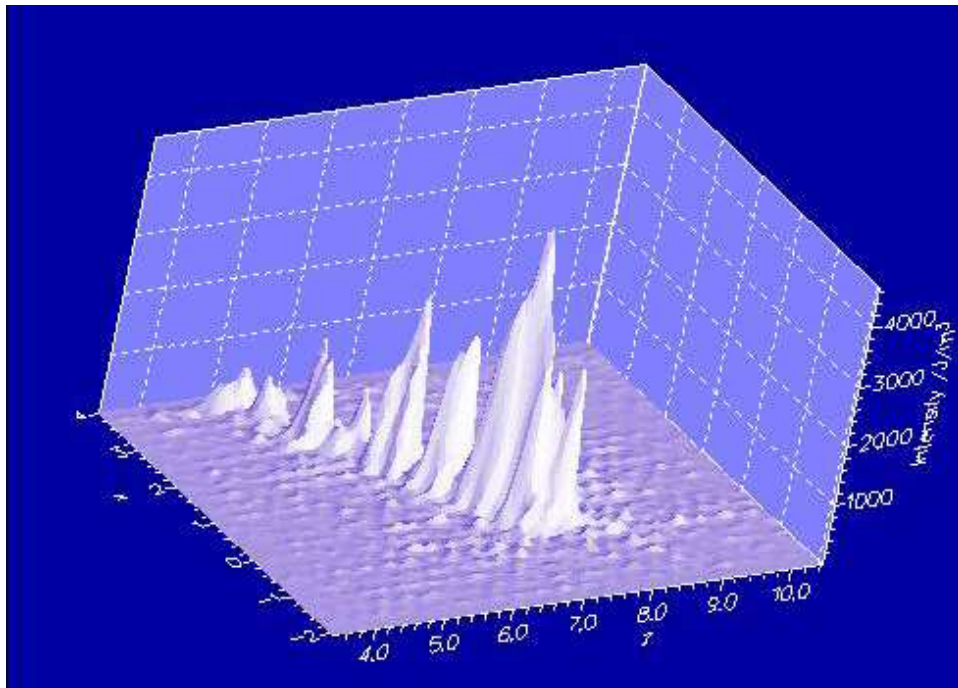
Figure 3.14:   Three-dimensional graph of the waveguide channel of the VCSEL simulation in Crystalwave.

42
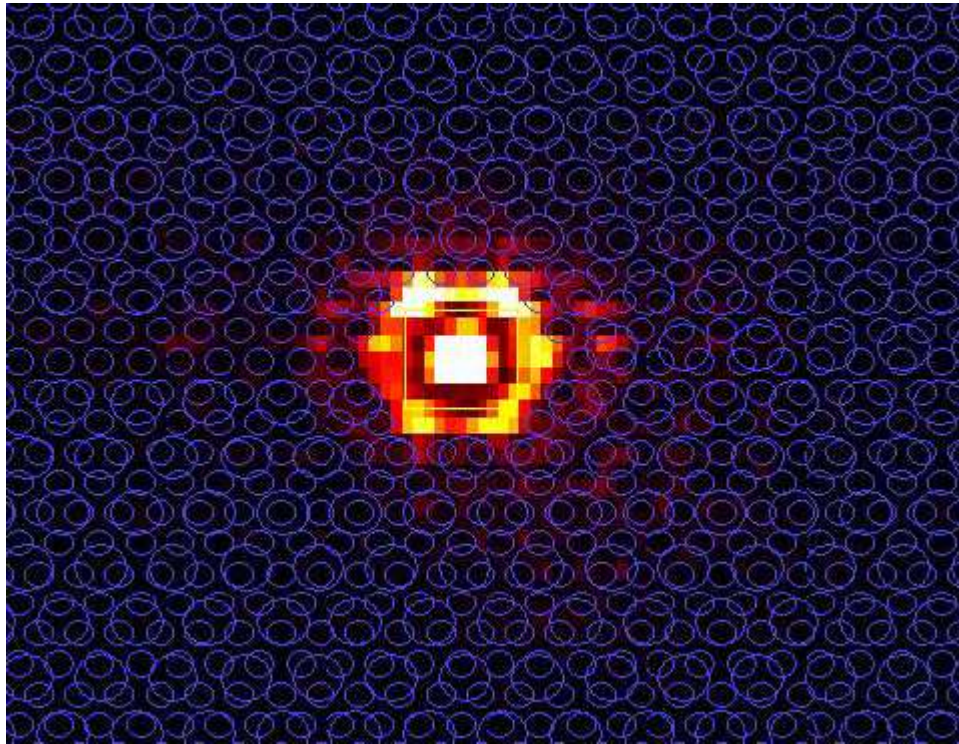
Figure 3.15:   The confinement of the gain medium of the VCSEL simulation in Crystalwave.
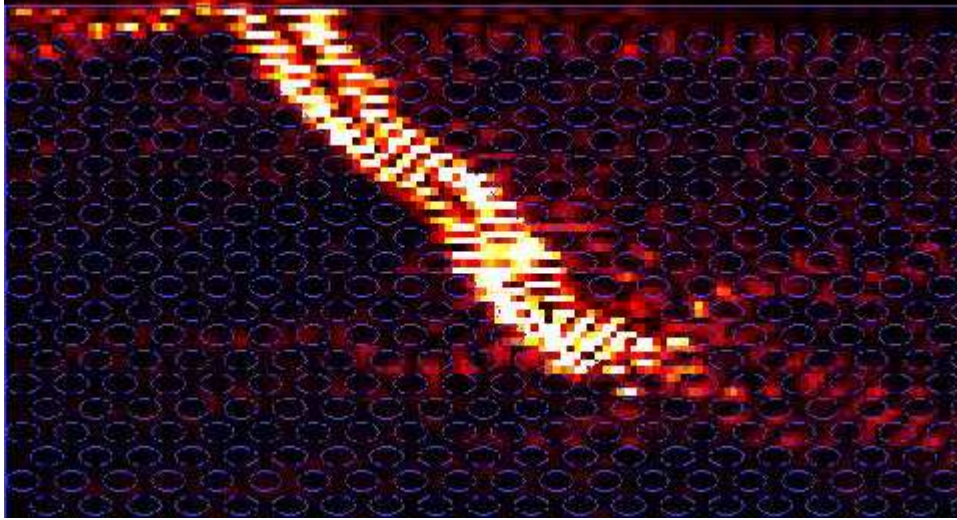
Figure 3.16:   Waveguide channel intensity of the test waveguide simulation in Crystalwave.

and end of the waveguide channel as in the VSCEL case. Figure 3.16 is the intensity image of this test scenario and Figure 3.17 is the net flux of the transmitted flux referenced to the reference flux.

It can be seen that, compared to the actual VCSEL simulation, the net flux is significantly less than that of the test case where the mode exciter exists in the waveguide region. It can also be seen that the reference amplitude of the VCSEL case is less than the reference of the test case (Figures 3.12 (a) and 3.18). This could be due to the fact that the mode in the VCSEL must pass through a 0.9 DBR before setting up a resonance in the waveguiding region. A comparison of the reference data (Figures 3.12 (a) and 3.18) shows that the starting flux at the beginning of the waveguide channel is significantly less than that of the test case.

This scenario shows that using a Gaussian mode exciter is a good work-around in the Crystalwave software to simulate a mode in the y-direction. It also shows the possibility of coupling off of a VCSEL laser and propagating the mode down a horizontal waveguide.

Some of OptiFDTD's and Crystalwave's analysis results have already been shown, and more of Crystalwave's results will be shown throughout the rest of the

44
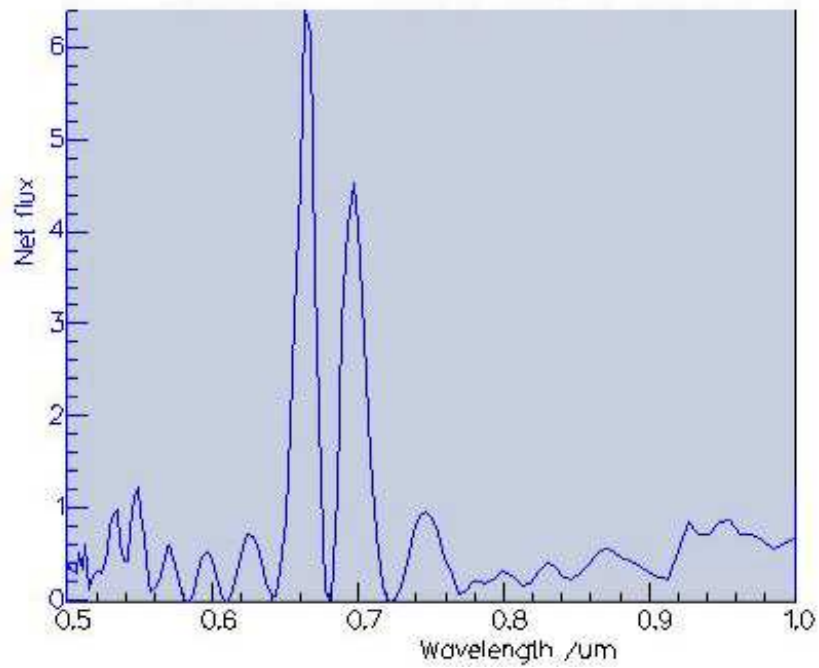
Figure 3.17:   Net flux of the test waveguide simulation in Crystalwave.
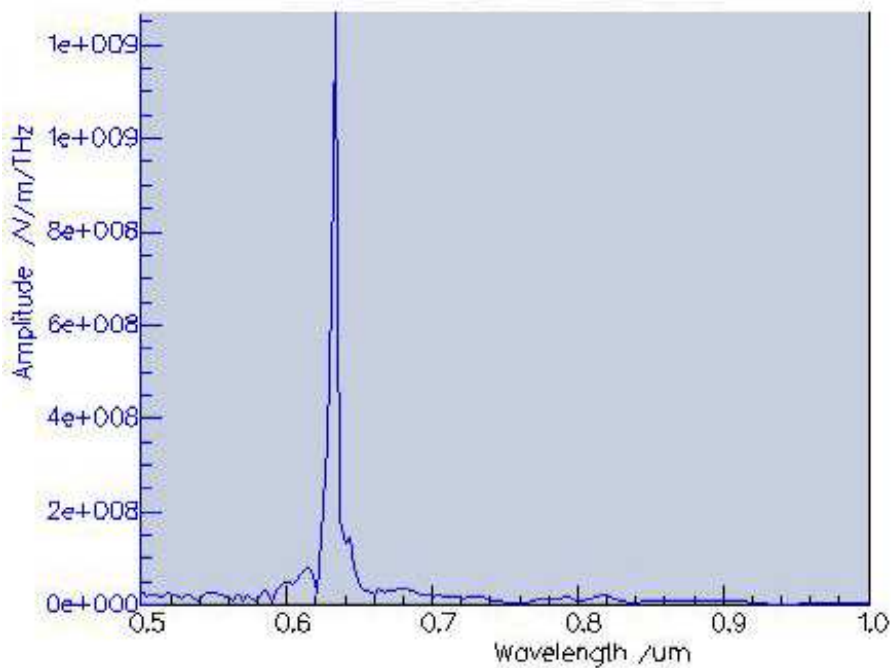
Figure 3.18: E_x field at the reference probe in the waveguide test simulation in Crystalwave.

45

document as they explain some of the modeled situations of this thesis.

Overall, both softwares are very useful and helpful in the modeling of PhC's. Optiwave's analysis is more of an ideal theory model and it was easy to represent band diagrams as previously modeled in other works. Crystalwave's features and user friendly design are very nice, and their results tend to be more the real-world approximation. Both come up with very similar results. The expectation is that either one of these software packages will provide results showing that the experiments closely match that of the modeled data. The goal is to prove that these softwares can produce results for the measured data that are accurate enough to validate their use for the design of future crystal structures.

3.2 Conclusion

The tools used to model any PhC design should be validated against test results. Once proper validation is concluded, the use of these tools will be extremely powerful for experimentation in different types and designs of PhC's, which will lead to better and more practical PhC designs with applications reaching into more fields. This software will also be extremely useful in determining the validity of a PhC design before the time intensive and costly fabrication stage. Two different FDTD types of software were evaluated and compared in this chapter. The end result showed that the either software is adequate; however, it does depend on the purpose of the specific PhC design being created and its intended purpose. This chapter shed some light into this aspect for these two softwares. Crystalwave will be used throughout the rest of this thesis as a continuation of its evaluation on the specific designs presented in the next chapter. The next chapter will demonstrate the design and fabrication techniques for the two-dimensional triangular PhC structures. One very important aspect to consider when evaluating an FDTD software is to fully understand the techniques used for modeling. For example, Crystalwave currently can do a three-dimensional FDTD solve; however, it is not a true three-dimensional FDTD analysis; it is an analysis of a two-dimensional structure in three-dimensions. However, they

www.manaraa.com

are working on the ability to have a three-dimensional structure solved using a three-dimensional FDTD analysis. The warning is to be aware of the terminology used by the software under question and fully understand the techniques employed by their analysis techniques.

IV. Experimental Design and Modeling for various Fabrication Techniques of Two-Dimensional Triangular and Three-Dimensional Face-Centered-Cubic Photonic Crystals

The creation of each PhC for this thesis was designed using a gap map program for two-dimensional triangular PhCs. They were then verified by a band diagram program and modeled (as part of the software evaluation) by commercial FDTD software. The fabrication techniques explored, to determine viability of the fabrication process for this PBG wavelength range, were: focused ion beam, holographic polymerization/lithography, and electron beam lithography. The criteria for a PhC, which was covered in the theory as explained in Chapter I, and lessons learned from previous experiments, as shown in Chapter II, were used and considered when designing the two-dimensional triangular PhC's in this thesis. The process of designing and modeling PhC's based on the fabrication techniques listed above is outlined in this chapter.

4.1 Focused Ion Beam Technique of Two-Dimensional Triangular Photonic Crystals

One of the fabrication techniques attempted for the two-dimensional PhC's was the focused ion beam (FIB) process. For this process, the desire was to create a PhC in a waveguiding medium, allowing for the PhC to be characterized by various incident angles of a wavelength that resides in the PBG; in this case, the PBG is designed for a helium-neon laser (632.8-nm) wavelength. Silicon nitride and Amorphous Poly Carbonate (APC) were the two materials chosen in which the PhC would be etched using the FIB process. A limitation of the FIB process is that the size of the PhC that can be created, in any reasonable time frame, is extremely small, smaller than any slab waveguided beam. Due to this constraint, a mask of air was attempted, as well as a mask of gold, in order to prevent light from going around the PhC and flooding the detector.

The gold mask concept is a two-step process with the FIB. Once the gold strip

E-Beam	Mag	Det	Spot	FWD	Tilt	Scan	100 μm
5.00 kV	350 X	SED	4	4.858	0.0°	H 22.63 s	
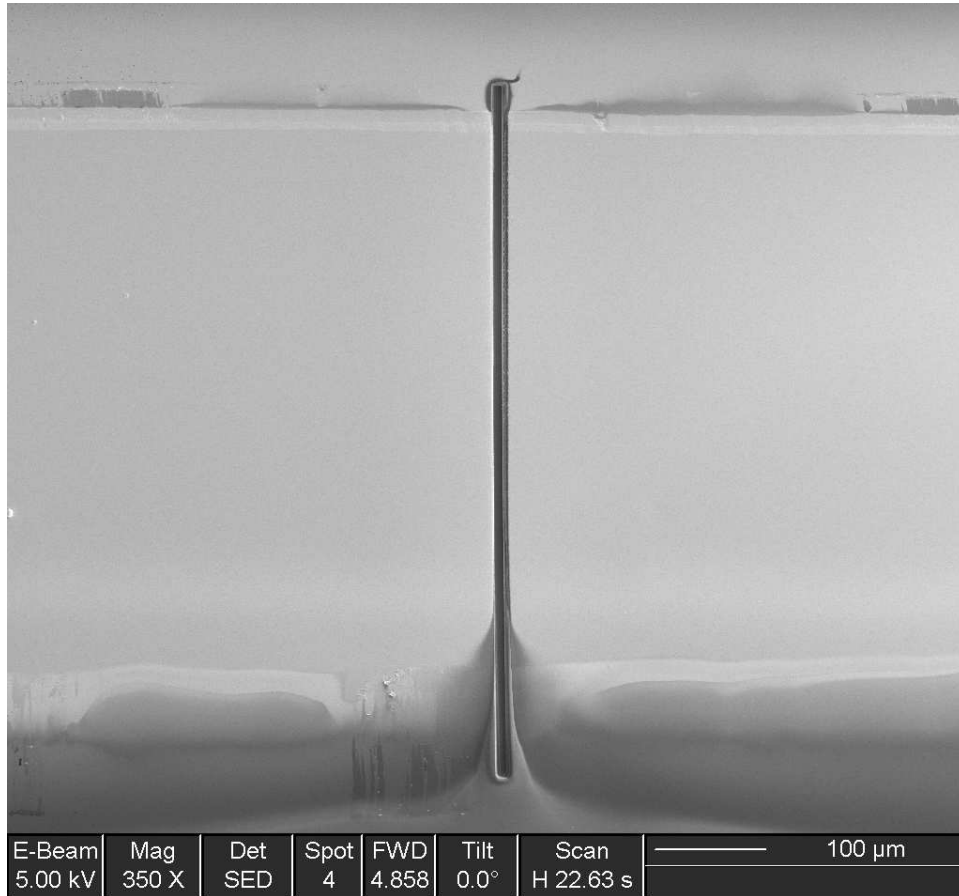
Figure 4.1:   SEM image of gold strip with a 10-μm wide channel cut by the FIB.

is deposited by means of shadow masking across the wafer (in a thin line), the FIB cuts a 10-μm channel in the gold line as shown in Figure 4.1. In terms of the FIB, this gold line is large and it is extremely time-consuming to cut a 10-μm wide channel through it. Other methods to shorten the time frame were to only cut a short channel into the gold line. This would allow enough room past the PhC region that the scattering of the beam, off of the back wall of the gold, could still be observed if the beam propagated through the PhC. Figure 4.2 shows some of these shorter channels that were etched by the FIB process. After the channel is etched in the gold, the wafer would have silicon nitride or APC deposited on it. The FIB is then used to etch the PhC structure in the opening of the channel. This will enable the PhC to be tested at various incident angles.

49
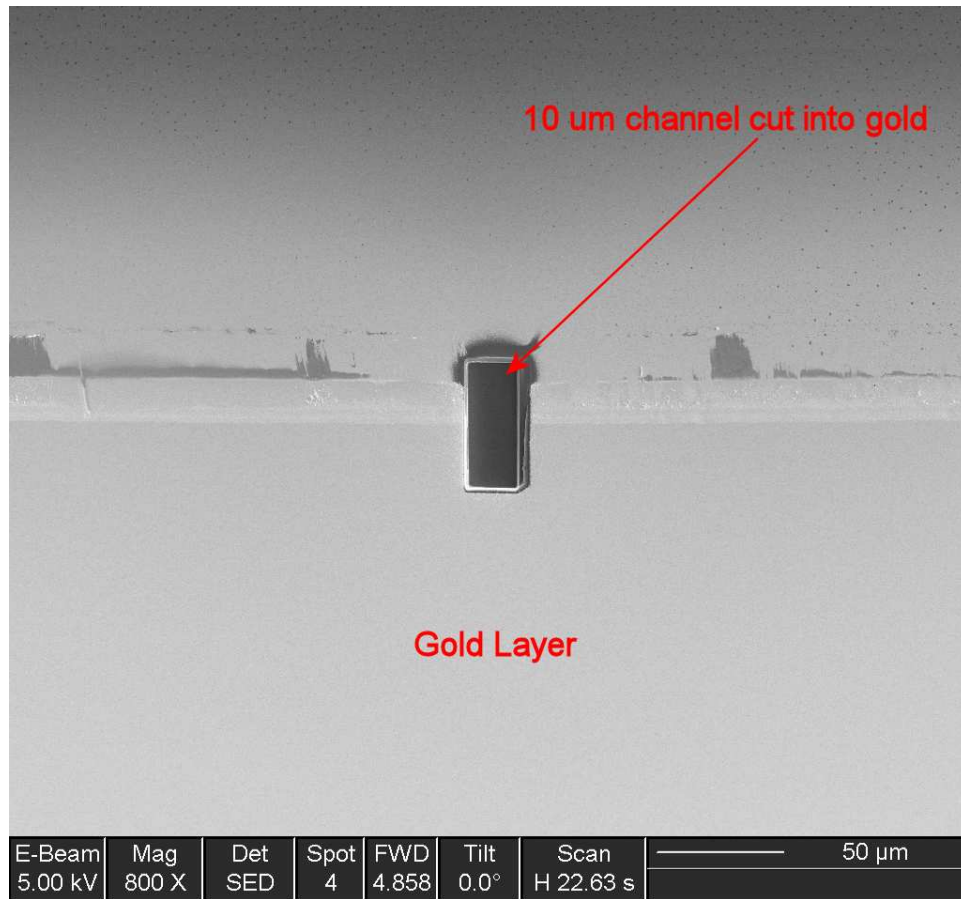
Figure 4.2:   SEM image of gold stripe with a 10-μm wide channel cut part way into gold by the FIB.
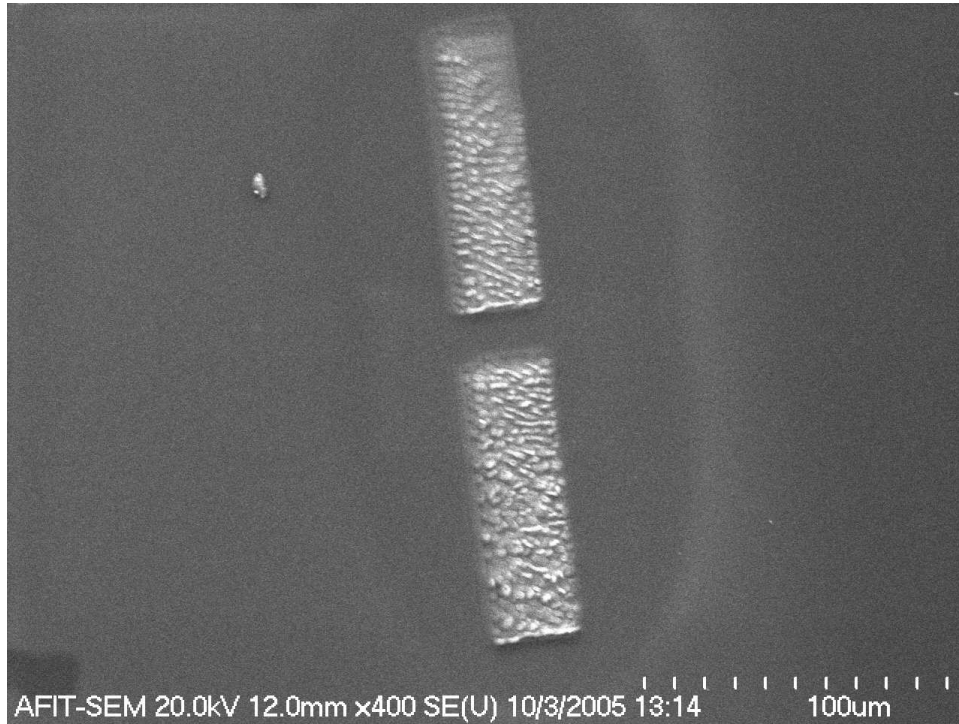
Figure 4.3:   SEM image of APC with large rectangular sections
blasted away leaving a 15-20-μm wide channel between them.

The air mask concept is a one-step process for the FIB technique. After de-
positing the silicon nitride or APC on the wafer, the FIB etches away large pieces of
the material (silicon nitride or APC) leaving a 15-20-μm channel (Figure 4.3) between
the etched areas. Then, the PhC can be etched in the opening of this channel.

Another technique initially attempted was to use the FIB to create a mask to
be used in a photolithography process. The FIB would etch the PhC structure in the
resist on the back of the mask so that the chrome could then be etched and the resist
stripped away. On the second mask, the FIB was used to etch all the way through the
chrome (Figure 4.4). This approach was abandoned due to time constraints; however,
it would appear that diffraction effects, due to the wavelength of UV and feature size
of the PhC, would prevent this technique from producing a PhC of this size

Before going forward with the etching process, several calculations were per-
formed for each material to ensure that light could be waveguided into the material
(able to support at least one mode), and then determine if a PBG can be obtained

51

E-Beam	Mag	Det	Spot	FWD	Tilt	Scan	2 µm
10.0 kV	20.0 kX	TLD-C	4	5.048	52.0°	H 22.63 s	
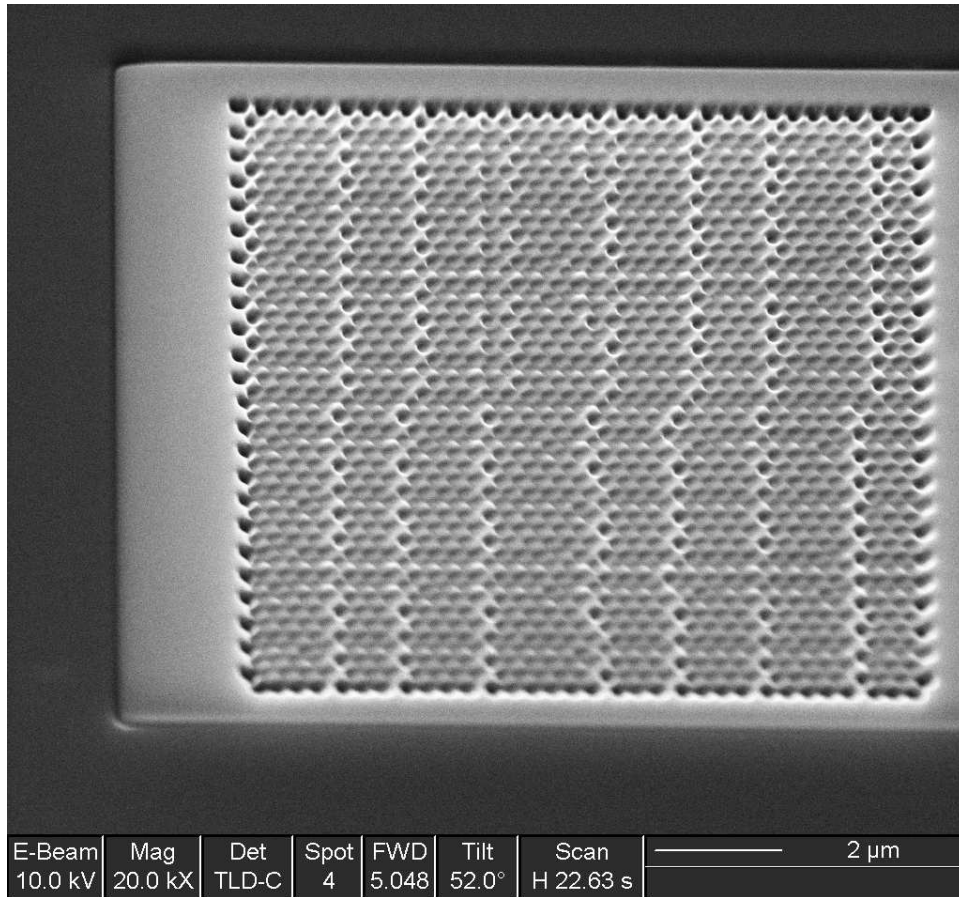
Figure 4.4: SEM image of a 48-period PhC etched into the resist of a photolithography mask by the FIB.
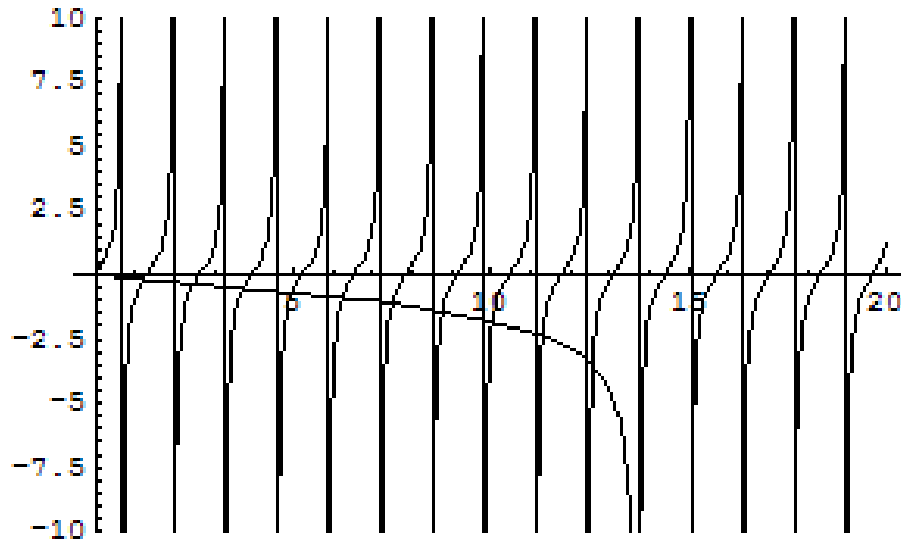
Figure 4.5: MATHEMATICA® graph of modes supported in 2.4 μm thick silicon nitride.

in the same material based on the construct of a two-dimensional PhC for a PBG at 632.8 nm. In order to determine the waveguiding and mode propagating capabilities, a series of equations in MATHEMATICA® was performed (see Appendix A). For silicon nitride that has an index of 2.0 with a thickness of 2.4 μm deposited on top of 3 μm of silicon dioxide (index of 1.457) on a silicon wafer, approximately ten modes are supported (Figure 4.5).

The prism that is used to couple the beam into the silicon nitride must have an index greater than silicon nitride (n = 2.0). A rutile prism has an index higher than that of silicon nitride; however, it is a birefringent crystal. This property of the rutile prism makes it more difficult to use as a waveguide due to the changing indices of the fast and slow axes based on the orientation of the optic axis in the prism and the incident angle of the beam on the prism. The placement of the prism, in regards to its distance from the optics, is critical to determine the proper incident angle into the prism necessary to couple the laser beam into the waveguiding material; these angles are depicted in Figure 4.6. For a more in-depth look into the principals of prism coupling, see Appendix B. The angle determined from the equations in Appendix

53
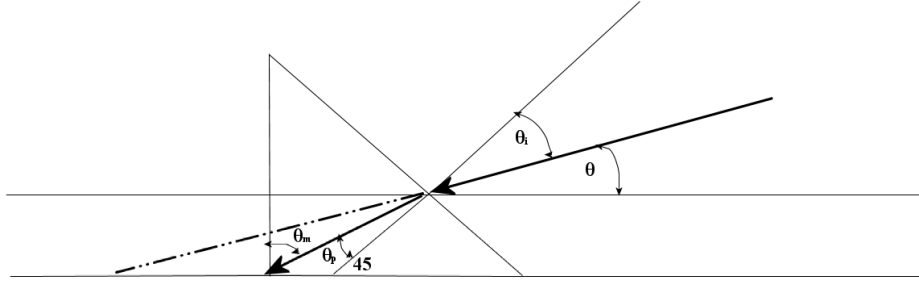
Figure 4.6:   Illustration for calculating angles necessary for determining proper prism coupling.

A is the Θ_m of Figure 4.6. In order to back out the Θ and Θ_i of Figure 4.6, it is necessary to use the following equations from Snell's Law;

$$\Theta_i = \arcsin(n_p(\sin(\Theta_m - 45°)))$$

$$\Theta_i = 45° - \Theta \tag{4.1}$$

where n_p is the index of refraction of the prism. With these angles, the distances and heights required to obtain the proper coupling angles can be calculated.

Once the calculations show that these materials can support a mode and can be prism-coupled into, it is necessary to determine if there exists a band gap for this material in the wavelength range desired. A program created for this thesis to display gap maps for various materials is shown in Appendix C. The gap map for the silicon nitride, with a periodicity of 0.35 μm and varying the radius of the triangular columns from 0.1 to 0.175 μm, can be seen in Figure 4.7. This gap map displays both polarizations' (E and H) band gap positions. The two-dimensional triangular structure with the periodicity, 'a', and radius, 'r', as stated above, has no overlaping/complete PBG in two-dimensions as shown in Figure 4.7. For there to be an overlapping PBG, the gap map would show the PBG of each polarization (TE and TM) overlapping. As shown in Figure 4.7, the TM polarization (gap between the red and blue lines) and the TE polarization (gap between the green and black lines) do not cross over each

54
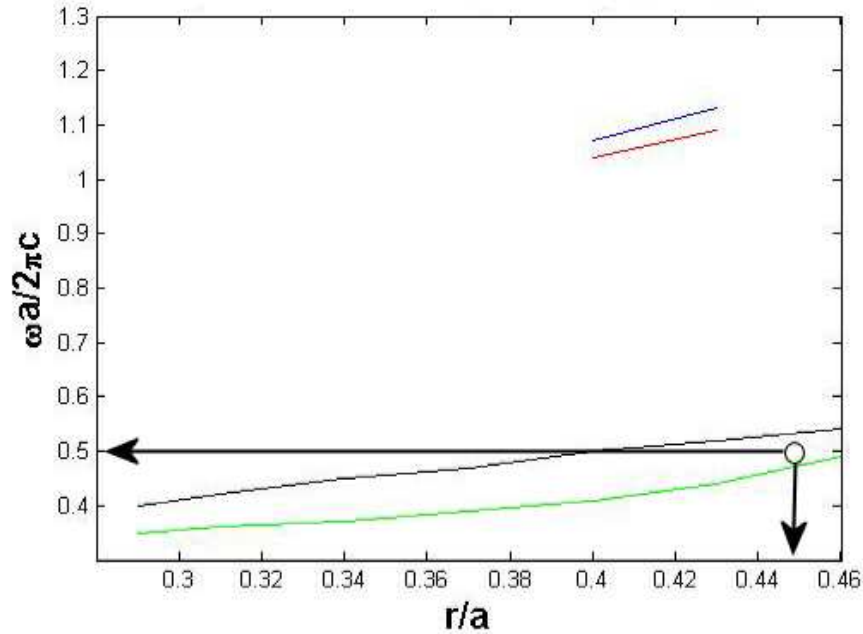
Figure 4.7: Two-dimensional triangular structured PhC gap map of silicon nitride with a periodicity of 0.35 μm and a radius range of 0.1-0.175 μm designed with columns of air ($\epsilon = 1$) in the silicon nitride ($\epsilon = 4$) where the TM field polarization band gap is shown between the red and blue lines and the TE field polarization band gap is shown between the green and black lines.

other. Based on this data, the E field will be chosen on which to base the design of the PhC for silicon nitride. From the gap map in Figure 4.7, if $\omega a/2\pi c = 0.5$, then correspondingly, $r/a = 0.45$. By solving these two equations for a λ of 632.8 nm, the periodicity (a, center to center of the columns) is 316.4 nm and the radius of the columns, r, is 142.4 nm. The band diagram program of Appendix C can now be used to verify these dimensions for both the E and H fields.

The band diagrams displayed in Figure 4.8 show the E and H field polarizations' band diagrams using the periodicity of 316.4 nm and a radius of 142.4 nm in silicon nitride. The numbers of the x axis in these band diagrams correspond to the momentum vector direction in the reciprocal lattice of the crystal. Going from 0 to 20 corresponds to going from K to Γ (in the reciprocal lattice space), 20 to 40

55
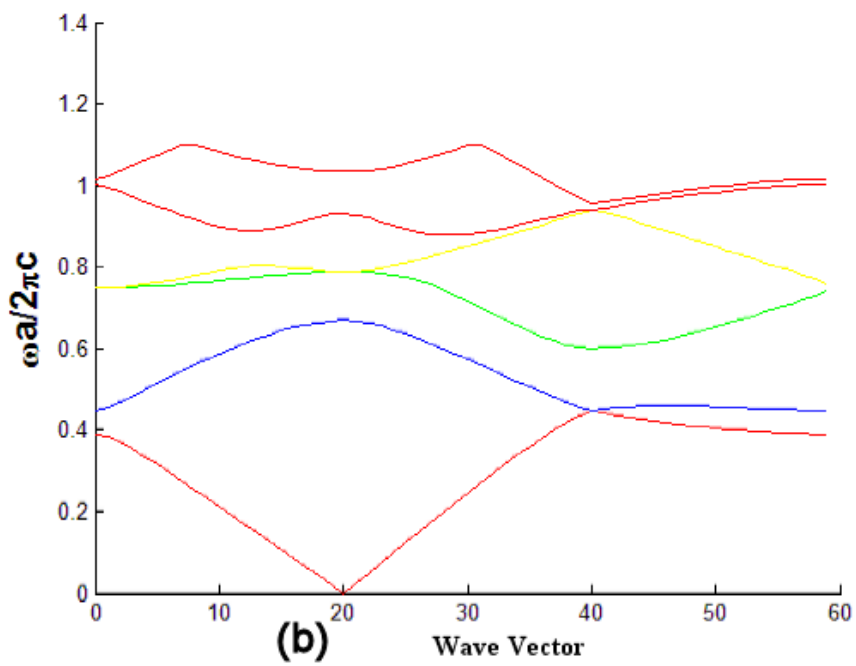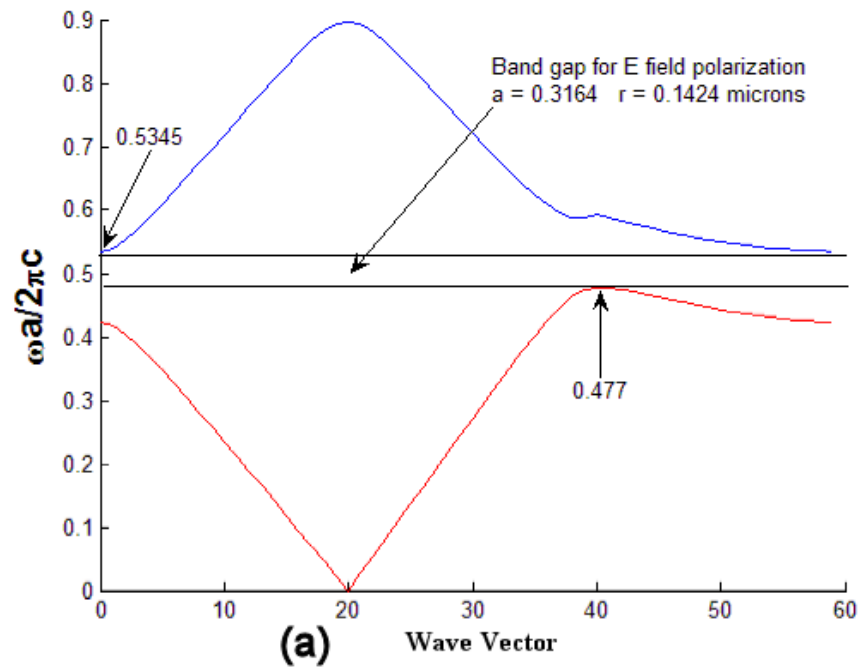
Figure 4.8: (a) Band diagram of E polarization and (b) H polarization for silicon nitride with $a = 0.3165$ μm and $r = 0.1424$ μm, based on columns of air ($\epsilon = 1$) in the silicon nitride ($\epsilon = 4$). Notice there is no band gap for this case.

56
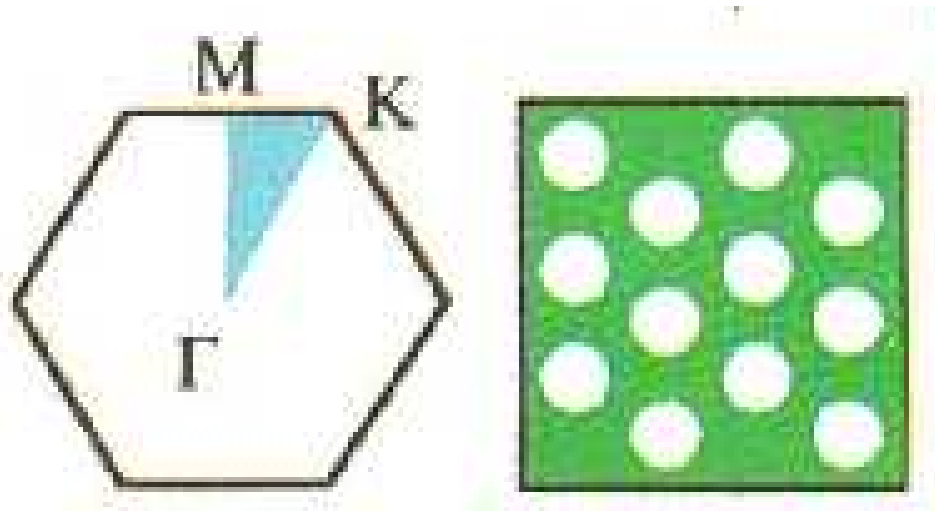
Figure 4.9: Reciprocal lattice space of the crystal; the left picture indicates the wave vector direction observed and the right picture indicates the reciprocal lattice of the two-dimensional triangular structure [12].

corresponds to Γ to M, and 40 to 60 corresponds to M to K. Figure 4.9 illustrates the reciprocal lattice space vectors and image of the crystal. From Figure 4.8, it is evident (as shown by the gap map) that there is a band gap for the E field but none for the H field based on these physical parameters in silicon nitride.

This same process and set of equations hold true also for APC. In this case, the APC was 1-μm thick and had an index of 1.57. By plugging these numbers into the Appendix A program and using a prism that has an index of 1.77 (SFL11), the number of modes that can be supported by the APC is two (Figure 4.10). For APC, the gap map shown in Figure 4.11, depicts E field polarization band gaps. No H field polarization band gap exists with the parameters used for this gap map. Thus, no complete PBG can be acquired in APC for these parameters. This gap map was created based on a periodicity of $a = 1.3$ μm and a radius that varied from 0.5-0.64 μm. To solve for the periodicity and radius needed based on this gap map and the λ desired, choose $\omega a/2\pi c = 0.5$, then correspondingly read down the gap map to get $r/a = 0.3935$. Solving these equations where λ is 632.8 nm gives a periodicity of 316.5 nm and a radius of 124.5 nm. The existence of the band gap for this geometry was

57
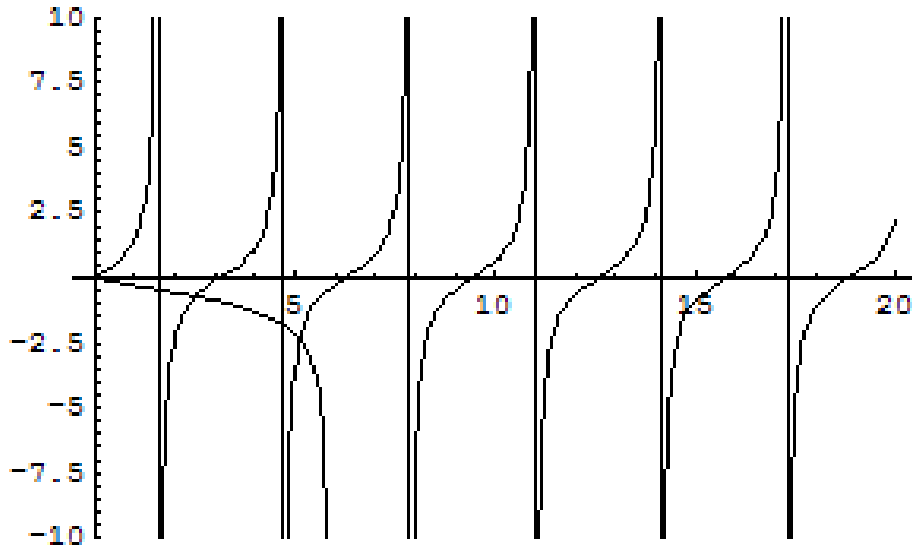
Figure 4.10:   The number of modes supported in APC where the APC
is 1-μm thick.

modified using the band diagram program shown in Figure 4.12.

For the photolithography process, the target material that the etched PhC
was to reside in was a silicon oxynitride material. This was deposited by a plasma
enhanced chemical vapor deposition (PECVD) process [2]. The index of this material
is 1.6 and it is 1.6-μm thick. This index is close enough to APC that the same PhC
geometry should work for it also.

The evaluation of the Crystalwave software also included the modeling of the
band diagrams of multiple materials. Figure 4.13 considers the case of a material with
an index of 1.57 (like APC or silicon oxynitride). The Crystalwave band diagram in
Figure 4.13 (a) can be compared to that produced using the gap map for this material
and is shown in Figure 4.12. Since Crystalwave allows the user to select the band
diagram to be displayed in units of wavelength rather than frequency, Figure 4.13 (b)
shows this band diagram, also.

58
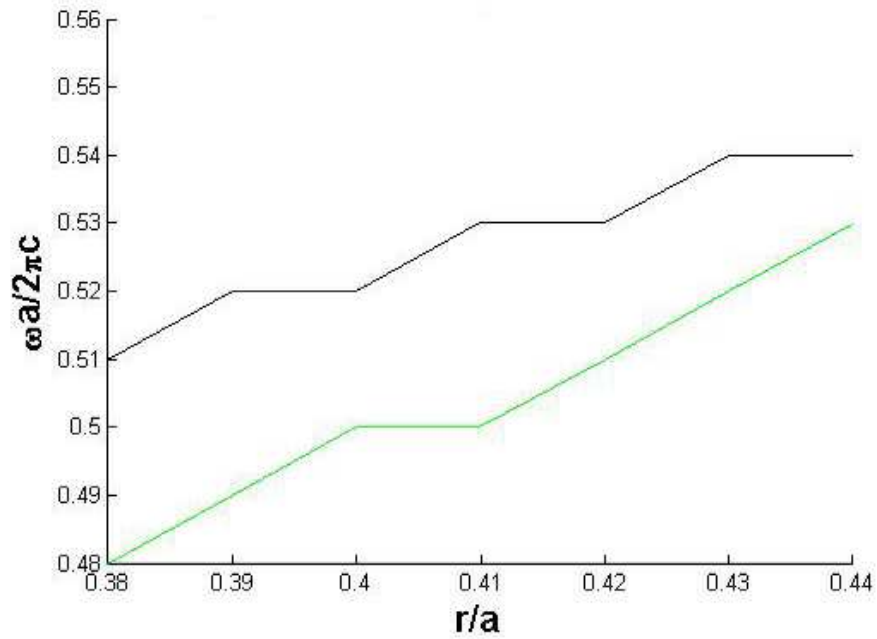
Figure 4.11:   Two-dimensional triangular structured PhC gap map
showing the E field of APC with a periodicity of 1.3 μm and a radius
range of 0.5-0.64 μm, designed with columns of air ($\epsilon = 1$) in the APC (ϵ
$= 2.4649$) where the TM field polarization band gap is shown between
the red and blue lines and the TE field polarization band gap is shown
between the green and black lines.
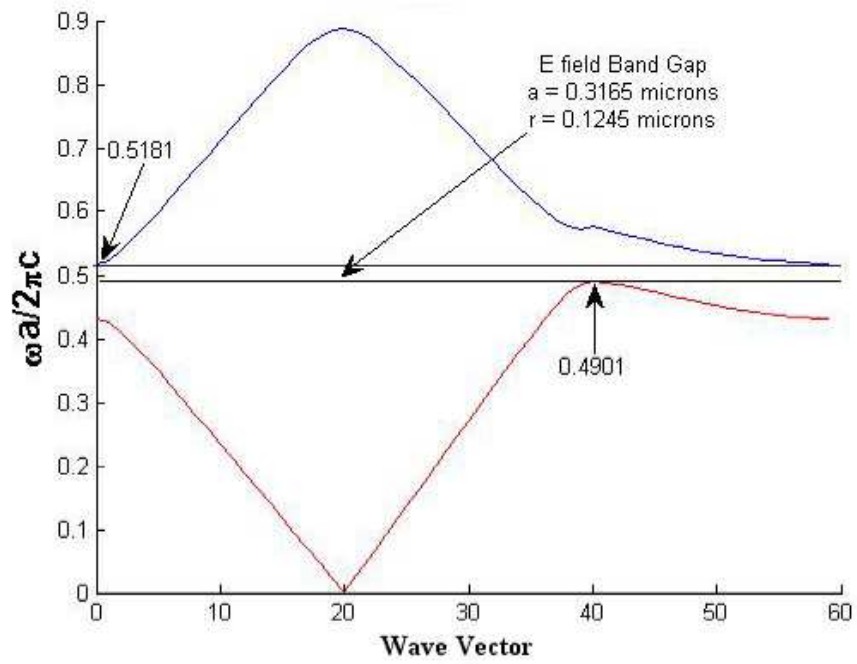
Figure 4.12:   Two-dimensional triangular PhC band diagram of APC for a 1-μm thick layer with $a = 0.3165$ and $r = 0.1245$ based on columns of air ($\epsilon = 1$) in APC ($\epsilon = 2.4649$).

60
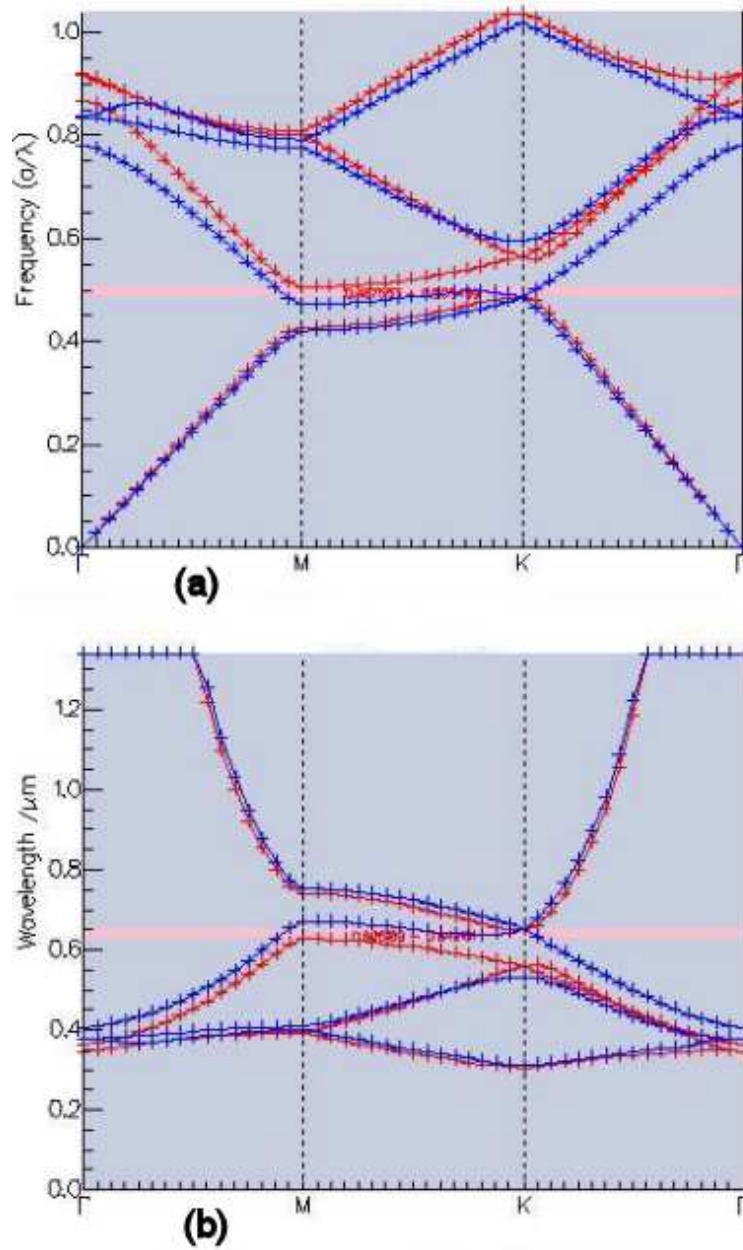
Figure 4.13: Band diagram of a material with an index of 1.57 and a periodicity of 316.5 nm modeled in Crystalwave using a triangular pattern showing only a TE band gap in units of (a) frequency (TE gap of 0.487553-0.505439 a/λ) and (b) wavelength (TE gap of 0.649161-0.626189 $(\mu m)^{-1}$).

61

4.2 Electron Beam Lithography Technique of Two-Dimensional Photonic Crystals

The electron beam lithography technique is being performed by the University of Illinois, Urbana-Champagne. The size crystal that they have produced before is approximately 2 mm x 2 mm, and the thickest that they have etched this type of structure into is around 500 nm. The structure of the wafer that they will etch a PhC into is a GaAs wafer with 400-nm growth of $Al_{0.98}Ga_{0.02}As$ and a 300-nm growth of $Al_{0.6}Ga_{0.4}As$ followed by a cap of 2 nm of GaAs. This wafer was grown by University of New Mexico, where they used a molecular beam epitaxy (MBE) process that is actually grown by a digital superlattice structure of aluminum arsenide (AlAs) and aluminum gallium arsenide (AlGaAs). During this growth process, the atoms will mix due to the elevated temperatures of over $600°$ C. The PhC structure will be etched through the $Al_{0.6}Ga_{0.4}As$ layer into the $Al_{0.98}Ga_{0.02}As$ layer. Then, the wafer will be oxidized so that the $Al_{0.98}Ga_{0.02}As$ layer will turn to aluminum gallium oxide (AlGaO), which will then be selectively etched away without damage to the PhC in the $Al_{0.6}Ga_{0.4}As$ layer. The selective etching of this new oxidized layer is accomplished with a solution of KOH:H2O (1 : 12 volume ratio). This will leave a structure that has the $Al_{0.6}Ga_{0.4}As$ layer with the PhC etched in it suspended in air (Figure 4.14).

This structure will allow the PhC to better confine the modes in the y-direction (the direction out of the top and bottom of the PhC) also providing for a better PBG, based on the light line of the structure. The light line goes as c/λ and is basically the region that separates the fast and slow wave. For a material that is infinite in the direction perpendicular to the direction of propagation, the light line is not considered; however, since this is not the case, the light line needs to be considered, as it will degrade the capability for the light to be contained in the material at the location of the PhC. Taking this into account, the previously mentioned setup will allow the PhC to be waveguided into by edge firing techniques. The technique of edge firing will produce a situation where the beam goes around the material (over the top of the material) and could saturate the detector. To prevent this saturation,
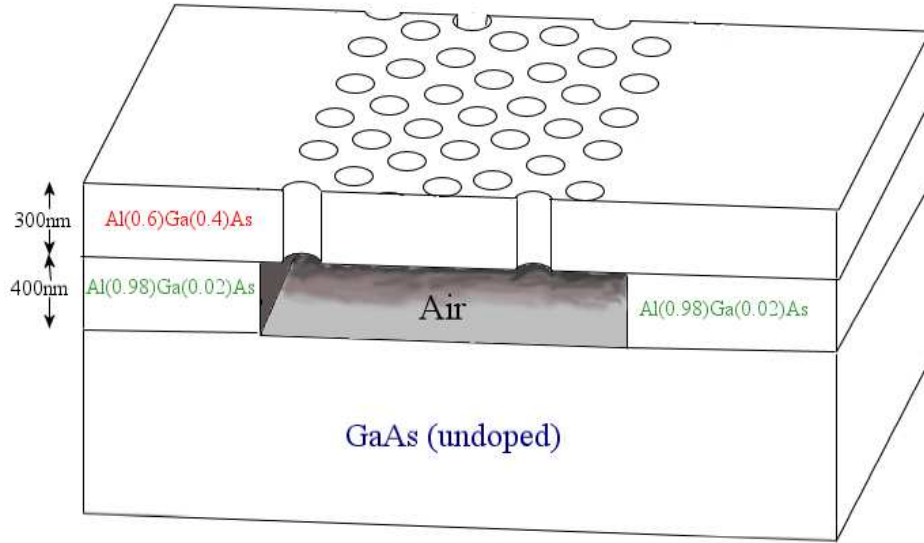
Figure 4.14:   Illustration of the final product of the AlGaAs PhC design.

the $Al_{0.6}Ga_{0.4}As$ layer will be etched into a curved waveguide region so the detector will not be in the line of sight of the edge fire beam (Figure 4.15).

The PhC structure is designed for a PBG at a wavelength of 632.8 nm. The AlGaAs has little to no absorption at this wavelength. The index program for Al-GaAs in Appendix D provides the real and imaginary parts of the index (imaginary corresponds to absorption). For $Al_{0.6}Ga_{0.4}As$ at 632.8 nm wavelength, it returns only a real value of 3.4554, indicating that there is no absorption at this wavelength. To determine if this size structure can support any waveguided modes, the previously discussed set of equations of Appendix A will be used again. Two test cases must be examined to determine that this structure is feasible to support a waveguided mode. The first test case is where the top and bottom cladding of the waveguide material ($Al_{0.6}Ga_{0.4}As$) are air and $Al_{0.98}Ga_{0.02}As$, respectively. Using this design, where $Al_{0.6}Ga_{0.4}As$ is 300-nm thick with an index of 3.4554, air has an index of 1, and $Al_{0.98}Ga_{0.02}As$ is 400-nm thick with an index of 3.1497, gives a total of one waveguided mode for this design (Figure 4.16 (a)). The second case is where the $Al_{0.6}Ga_{0.4}As$ layer is suspended in air. Modeling this situation shows that up to two

63
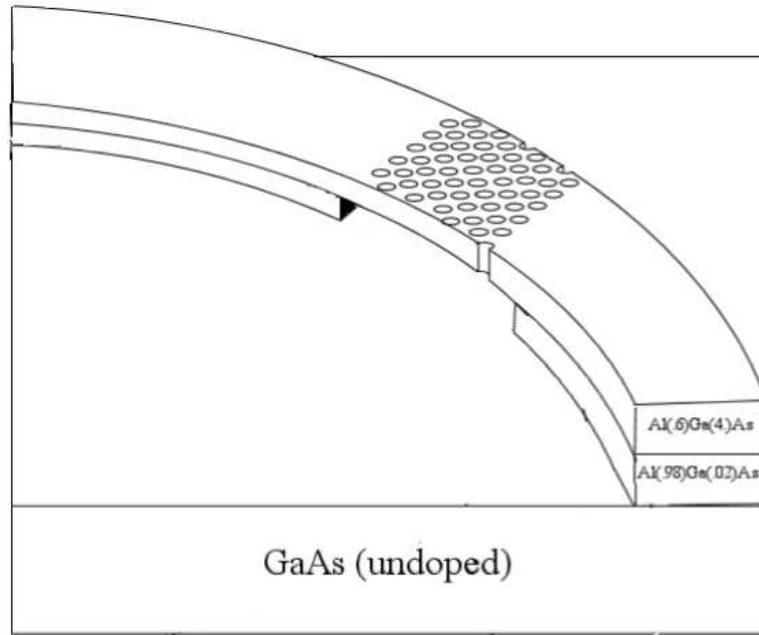
Figure 4.15:   Illustration of the curved waveguide for the AlGaAs PhC design.

modes can be supported (Figure 4.16 (b)).

Since the largest that the University of Illinois can etch is 500 nm, the 300-nm design was chosen. The typical volume fraction of the PhC triangular pattern that the University of Illinois can achieve is about 70 percent. This will drive the values that are picked from the gap map created by the program of Appendix C for this material. The gap map for $Al_{0.6}Ga_{0.4}As$ shown in Figure 4.17 shows that there exists a complete PBG for this material and structure size. In order to preserve this 70 percent University of Illinois design limitation, the values used are $\omega a/2\pi c = 0.676$ and $r/a = 0.3501$. Solving these equations, where $\lambda = 632.8$ nm, gives a periodicity of 427.77 nm and a radius of 149.76 nm. Plugging these values into the band diagram equations of Appendix C shows a complete band gap in the TE polarization and a small band gap for the TM polarization that overlap for this material and design, producing a complete two-dimensional PBG as shown in Figure 4.18.

The modeling of the $Al_{0.6}Ga_{0.4}As$ PhC structure was accomplished with the FDTD software, Crystalwave, as part of the trial evaluation of this software. This

64
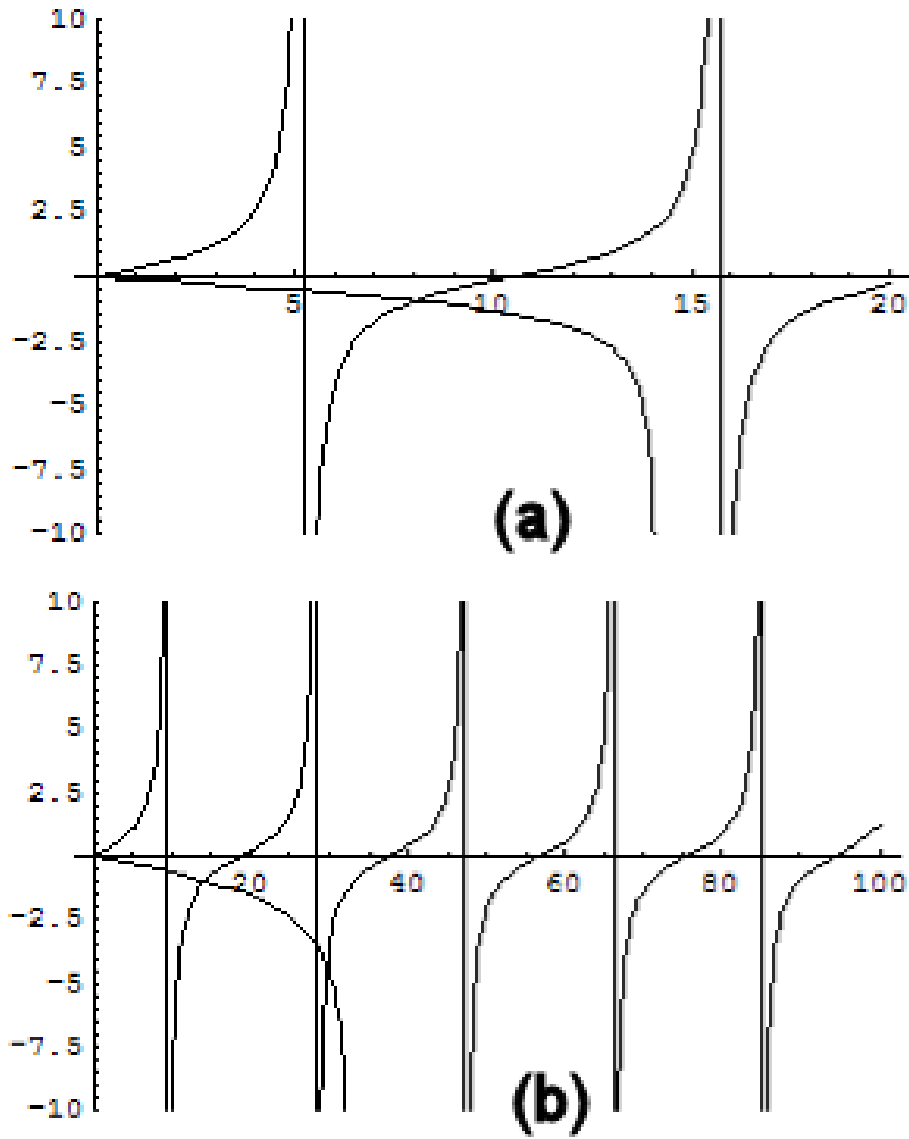
Figure 4.16:   (a) Modes supported in $Al_{0.6}Ga_{0.4}As$ that is 300-nm thick with air on one side and $Al_{0.98}Ga_{0.02}As$ on the other, (b) modes supported in $Al_{0.6}Ga_{0.4}As$ that is 300-nm thick with air on both sides.

65
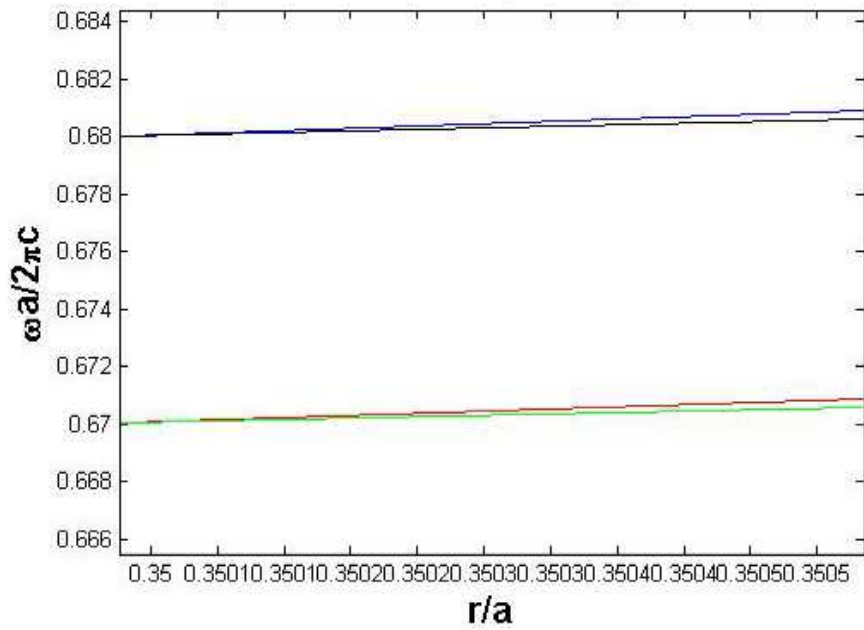
Figure 4.17: Two-dimensional triangular PhC gap map for $Al_{0.6}Ga_{0.4}As$ with $a = 1$ μm and $r = 0.34 - 0.38$ μm, based on columns of air ($\epsilon = 1$) in $Al_{0.6}Ga_{0.4}As$ ($\epsilon = 11.94$) where the TM field polarization band gap is shown between the red and blue lines and the TE field polarization band gap is shown between the green and black lines, showing a complete band gap for this structure.

66
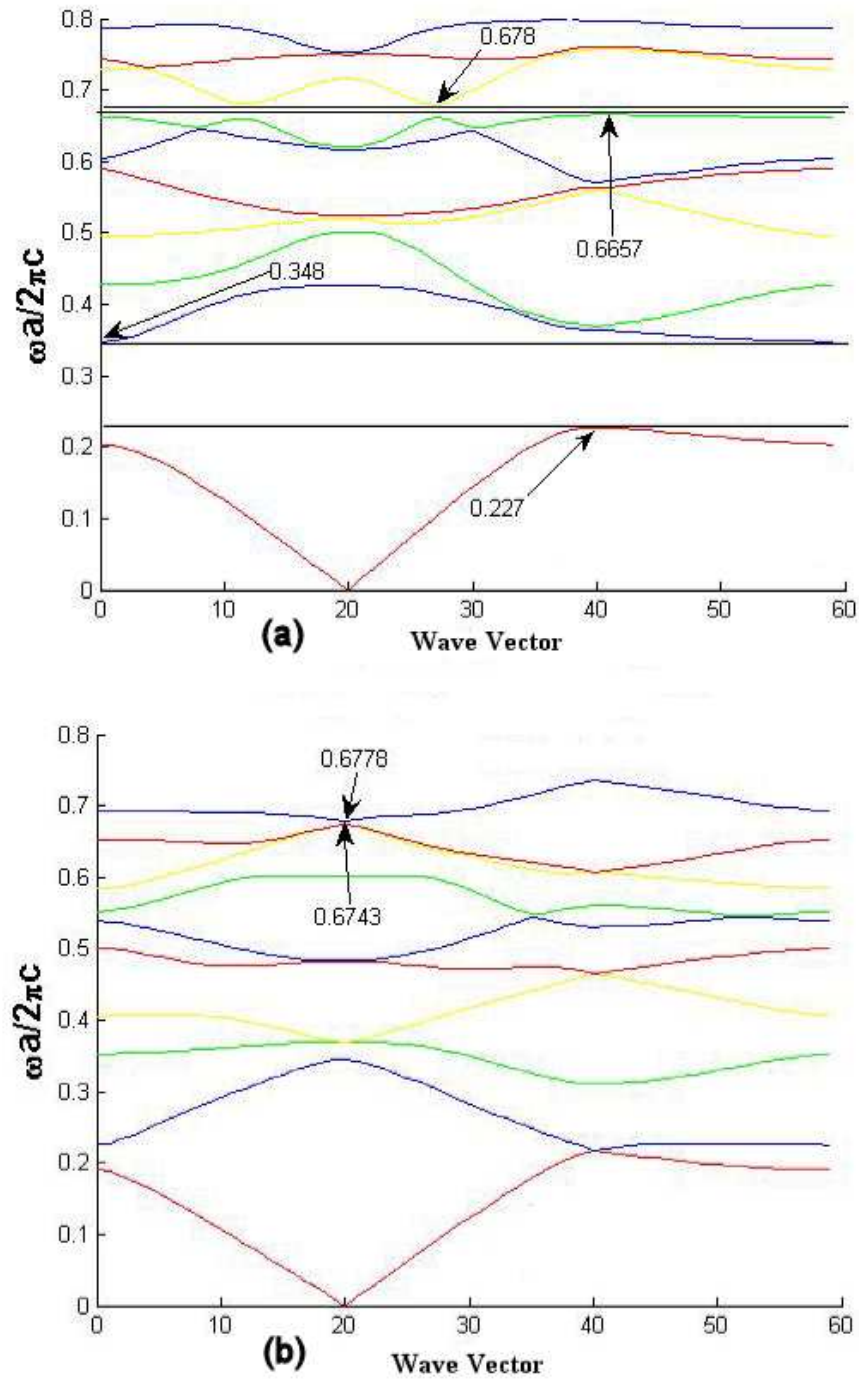
Figure 4.18: Two-dimensional triangular PhC band diagram for $Al_{0.6}Ga_{0.4}As$ with $a = 427.77$ nm and $r = 149.76$ nm, based on columns of air ($\epsilon = 1$) in $Al_{0.6}Ga_{0.4}As$ ($\epsilon = 11.94$) with the band gaps shown, for (a) E field polarization, and (b) H field polarization.

67

structure was modeled with the layers as described in the previous chapter. The simulation took into account that this structure was not infinite in the y-direction. The band diagram, however, still assumed infinite structure in the y-direction. The band diagram that was calculated by Crystalwave for a periodicity of 427.77 nm is displayed in Figure 4.19 and can be compared to that calculated using the gap maps of Appendix C (Figure 4.18) for this material and structure. Crystalwave software can also display this band diagram as a function of wavelength directly, as shown in Figure 4.19 (b).

Figure 4.20 is the Crystalwave GUI as it was created to model this PhC structure. At the time of this modeling, the exact thickness of the $Al_{0.98}Ga_{0.02}As$ layer had not been determined; however, it was known to be between 200-500 nm. In order to "bracket" the modeling possibilities, both of these dimensions were simulated in Crystalwave. In the Figures 4.21-4.24, both of these results will be displayed to show the bracketed capabilities of the PhC. The actual thickness of the $Al_{0.6}Ga_{0.4}As$ layer was modeled at 300 nm, which was as it was grown.

Data was obtained for incident waves at incident angles of 45° and 0°, relative to the input plane for the $Al_{0.6}Ga_{0.4}As$ PhC structure. From this data, it is concluded that for any angle within the two-dimensional plane, there exists a PBG at the 632.8-nm wavelength. Figures 4.21 and 4.22 are the FDTD results of a 45° incidence for E_x, E_z, and intensity for 200-nm and 500-nm air gaps with a 632.8-nm TE continuous wave mode exciter, respectively, and Figure 4.23 is the FDTD results of 0° incidence for E_x, E_z, and intensity of a 200-nm air gaps with a 632.8-nm TE continuous wave mode exciter.

The Fourier transform of the 45° incident angle case for the E_x and E_z fields of the reference and transmitted wave for 200-nm and 500-nm air gaps and a 632.8-nm TE continuous wave mode exciter were also analyzed. Figure 4.24 shows the net flux ratios for the 45° incidence case with the 200-nm air gap sample of the transmitted wave to the reference wave.

Figures 4.21 through 4.24 also show that this design is a good PhC for the TE

Figure 4.19: Band diagram of $Al_{0.6}Ga_{0.4}As$ modeled with Crystalwave software for a periodicity of 427.77 nm in a triangular pattern showing two TE band gaps in units of (a) frequency (TE gap of 0.221144-0.322734 and 0.636743-0.655249 a/λ) and (b) wavelength (TE gap of 1.934351-1.325456 and 0.671809-0.652836 $(\mu m)^{-1}$).

69
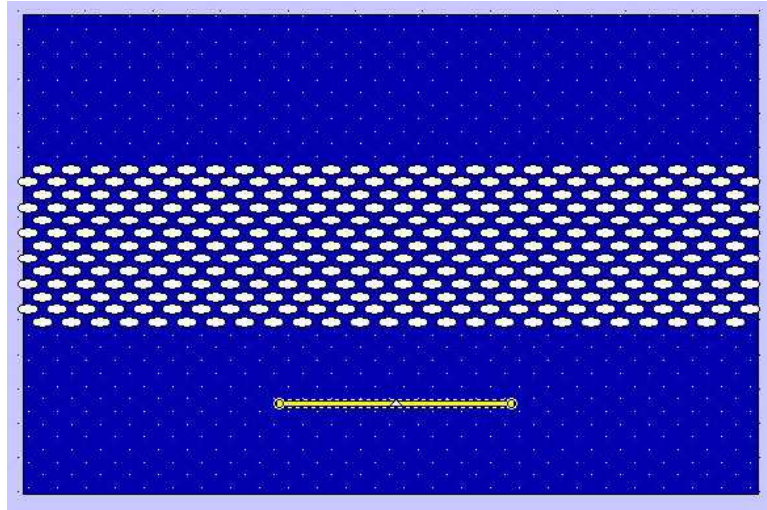
Figure 4.20: Graphical user interface used to model the $Al_{0.6}Ga_{0.4}As$ structure in Crystalwave software.

polarization case in the visible wavelength range.

4.3 Holographic Lithography Technique of Two-Dimensional Photonic Crystals

The holographic lithography process involves a two-stage process to ensure good structures. The first step, after the laser/optic setup is complete, is burning the first sample in a liquid crystal/polymer solution. This allows for a quick and easy determination of the PhC's periodicity. Once this process is complete, the next step is to write this structure into the photo-resist. The holographic process is based on the principal of wave interference. Three laser beams of specific orientation and polarization interfere and create an interference pattern, which is a pattern of high and low intensity areas. The equations for the E fields and propagation vectors were constructed in MATHCAD[®] [20]. The equations and program are displayed in Appendix E. In general, the three laser beams are set at λ-specific angles to the x-y plane and are referenced to the x axis. The sample is in the x-y plane. The beams are tilted off the perpendicular z axis by a specified angle, and each beam is given a specific polarization. One of the polarizations is TM polarized (in the plane of incidence), while the other is TE polarized (perpendicular to the plane of incidence).

70
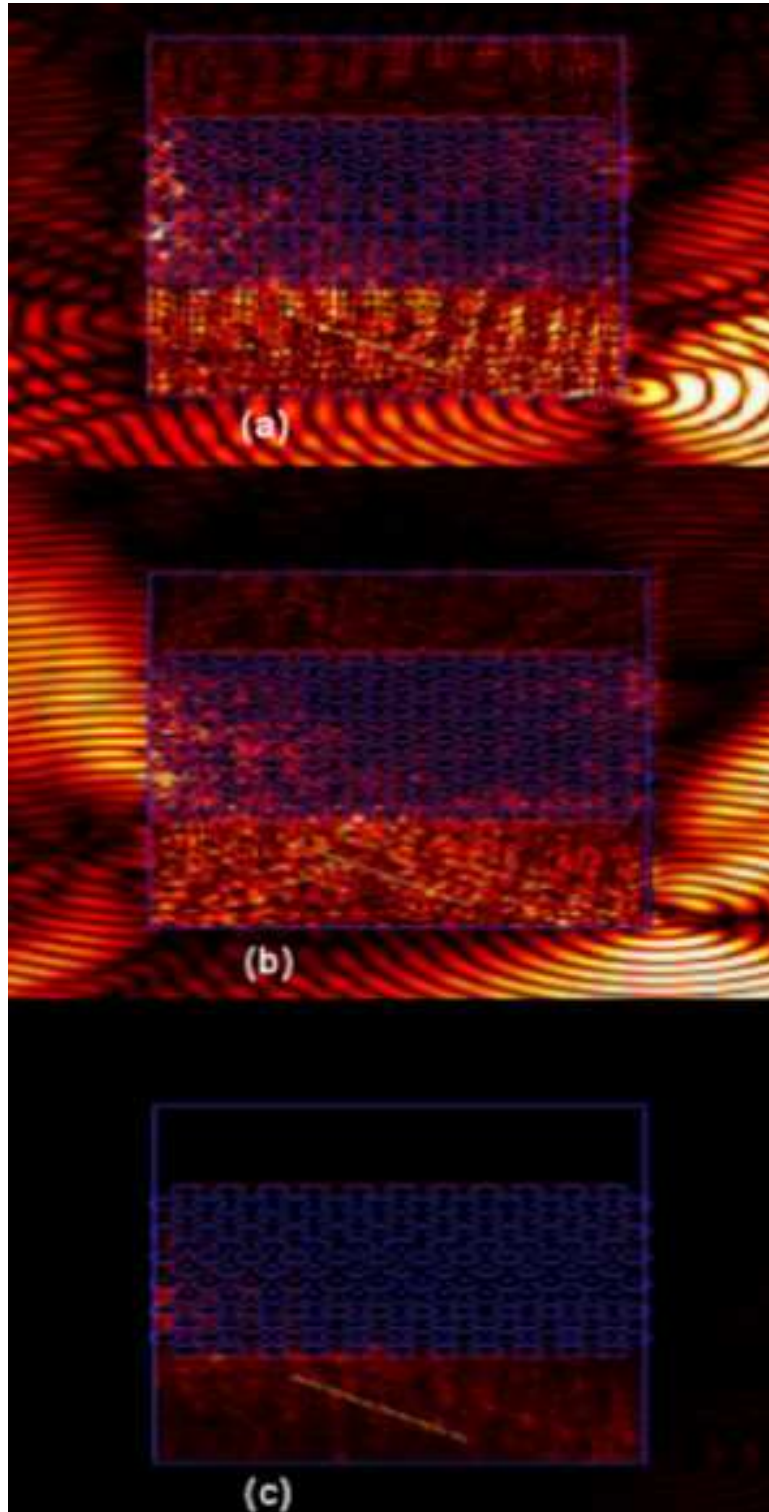
Figure 4.21: FDTD results of a 632.8-nm TE mode exciter at 45° incidence angle with a 200-nm air gap incident on a triangular structure PhC with a periodicity of 427.77 nm and a radius of 149.76 nm for (a) the E_x field and (b) the E_z field and (c) the intensity.

71
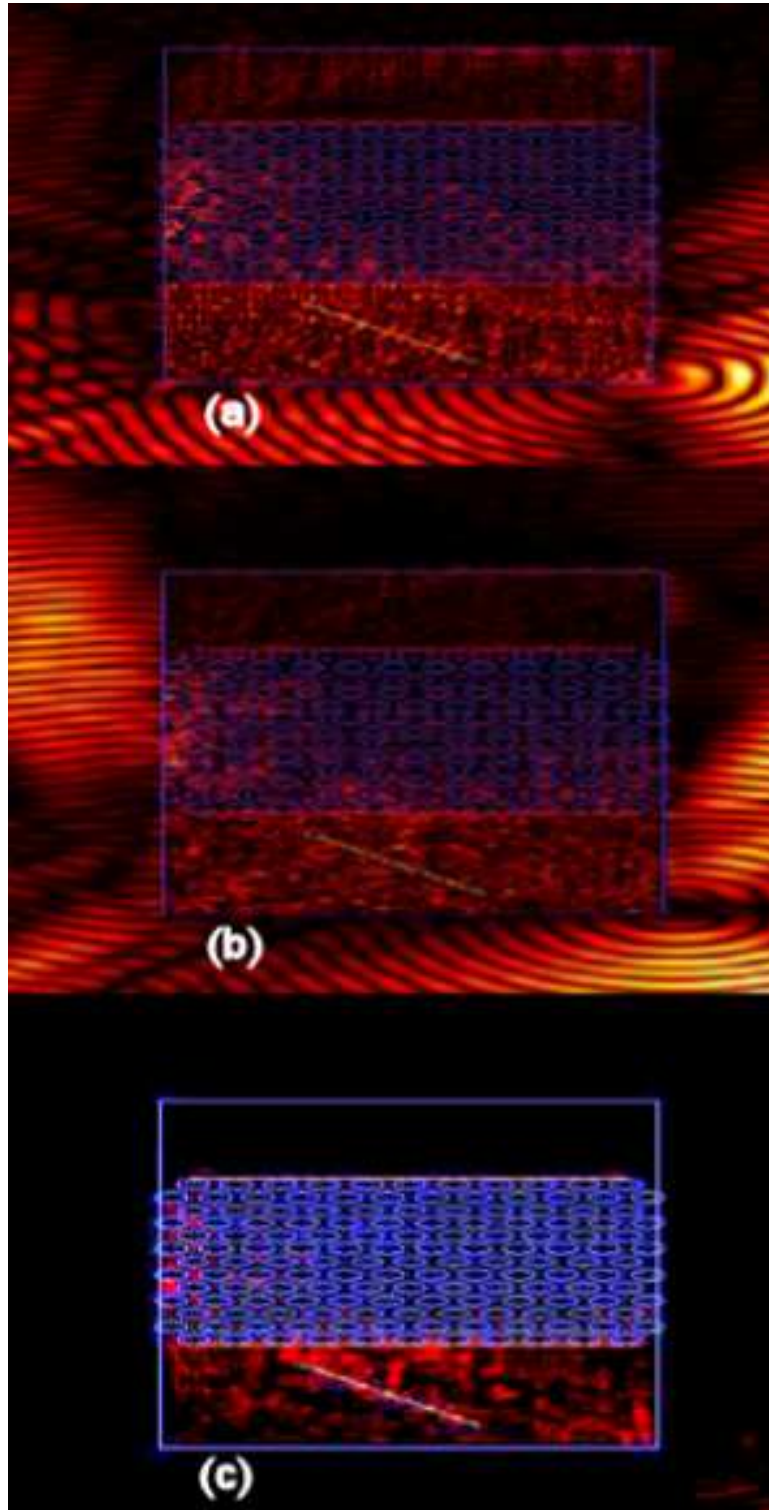
Figure 4.22: FDTD results of a 632.8-nm TE mode exciter at 45° incidence angle with a 500-nm air gap incident on a triangular structure PhC with a periodicity of 427.77 nm and a radius of 149.76 nm for (a) the E_x field and (b) the E_z field and (c) the intensity.
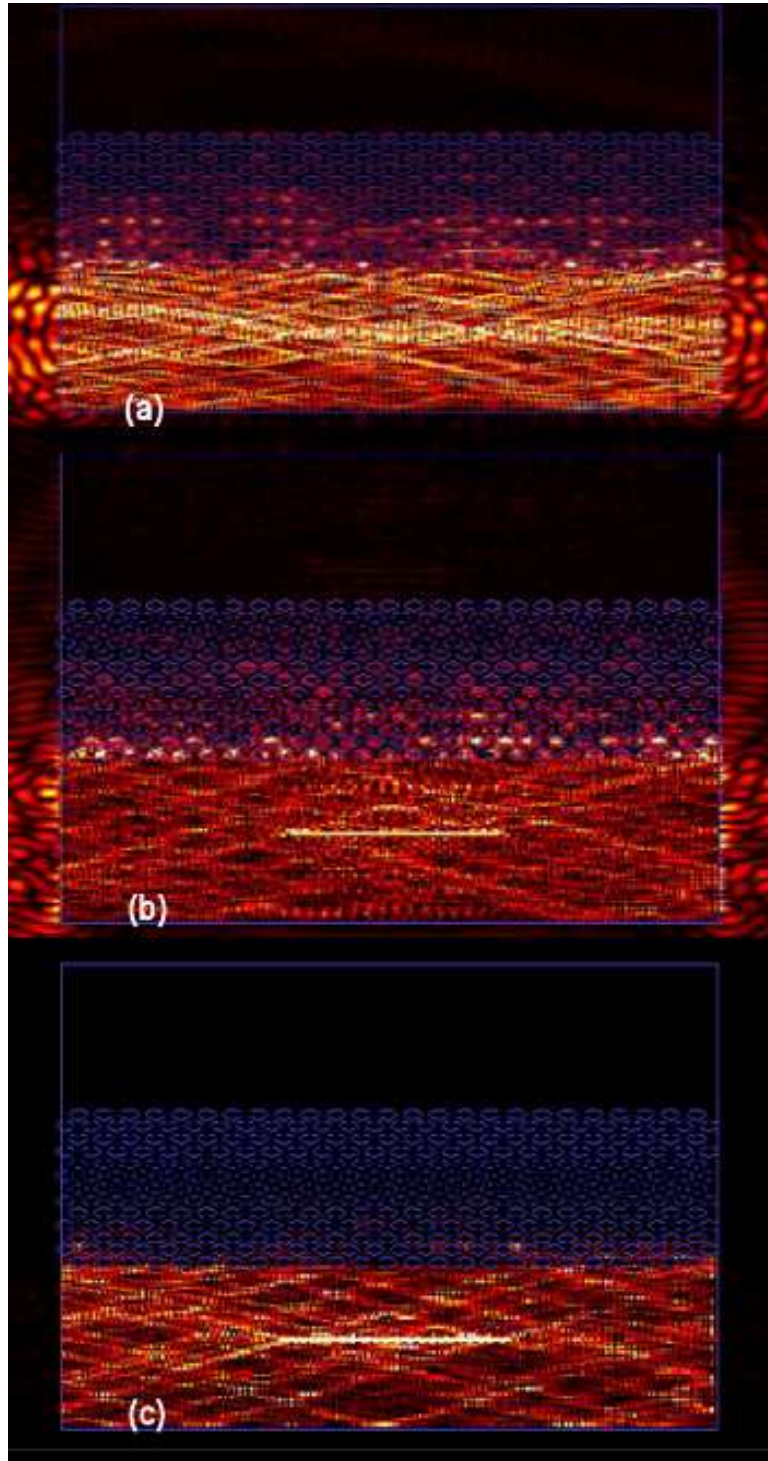
Figure 4.23: FDTD results of a 632.8-nm TE mode exciter at 0° incidence angle with a 200-nm air gap incident on a triangular structure PhC with a periodicity of 427.77 nm and a radius of 149.76 nm for (a) the E_x field and (b) the E_z field and (c) the intensity.
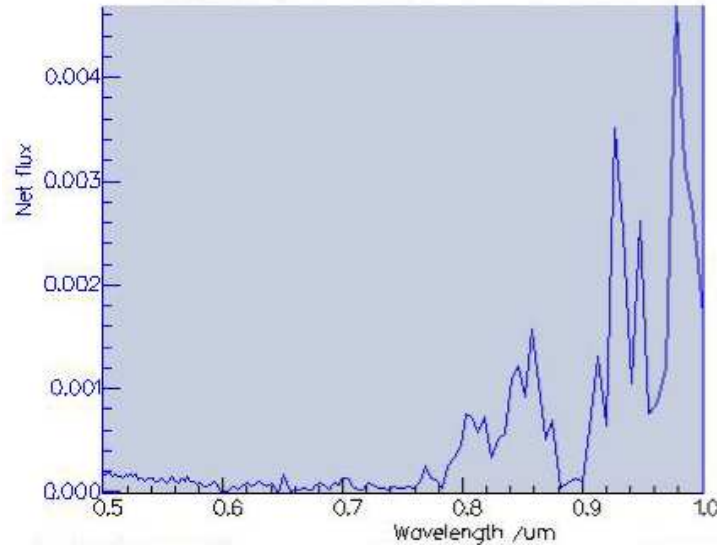
Figure 4.24: FDTD results of a 632.8-nm TE mode exciter net flux at a 45° incidence angle with a 200-nm air gap as a ratio of the transmitted flux to the reference flux on a triangular structure PhC with a periodicity of 427.77 nm and a radius of 149.76 nm.

The third beam is given an offset angle relative to the TE polarization. Figure 4.25 shows the geometry of this setup. This pattern is also dependent on the wavelength of the beam used to write the structure. By changing the angles, ϕ, θ (as shown in Figure 4.25) and the polarizations of the three laser beams, the proper geometry of the interference pattern can be achieved.

The material used for the final structure was SU-8 2010, a negative photoresist. This material has a dielectric constant at 10Mhz of 3.2 and a dielectric loss at 10Mhz of 0.007 per the manufacturer of the photoresist. Using the following set of equations, the index at the wavelength, 632.8 nm, can be determined [13].

$$k = -(L)(2/\pi)$$

$$\epsilon(f) = \epsilon_0 (f/f_0)^{-k} \tag{4.2}$$

74
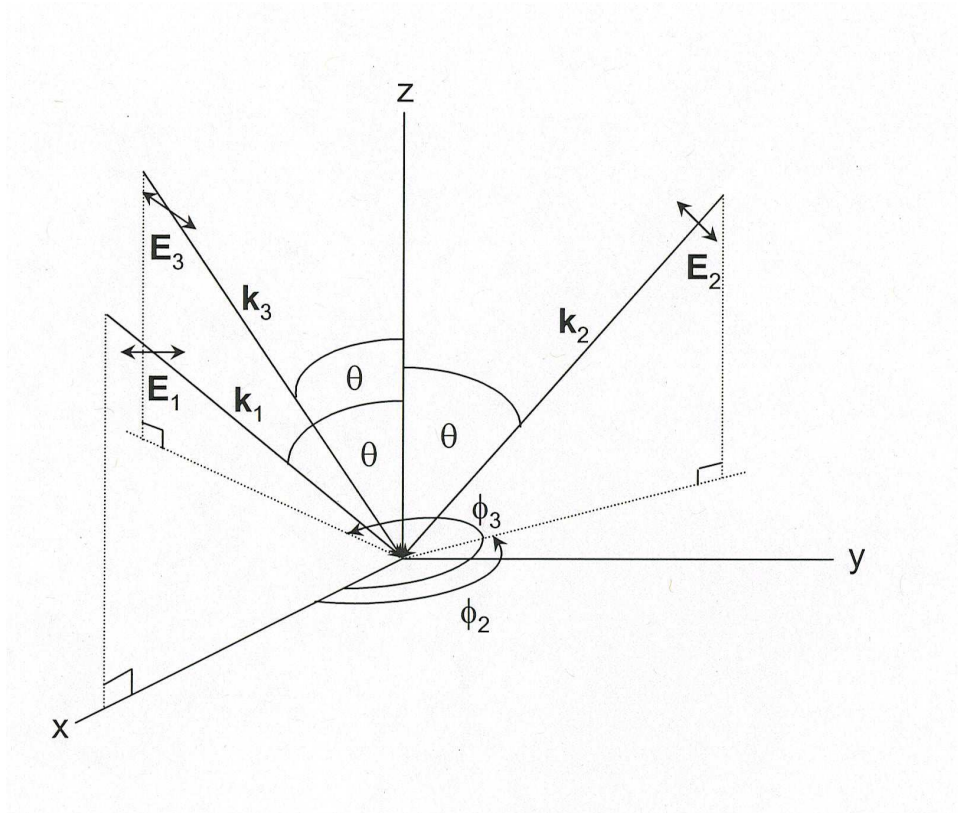
Figure 4.25: Holographic laser beam setup for two-dimensional structures used in this thesis, with the propagation vectors of the three laser beams displayed as K_{1-3} [20].

where L is the loss number, k is rate of deterioration constant, ϵ_0 is the magnitude of the dielectric constant at 10Mhz, f_0 is 10Mhz and f is the target frequency. Plugging in the numbers to these equations and solving for n by the equation, $n = \sqrt{\epsilon}$, results in an index of 1.719 at a wavelength of 632.8 nm. The prism coupling technique will be used to test this PhC design, and the MATHEMATICA® equation stated in Appendix A will provide the proper angles for prism coupling and the number of modes that can be propagated in this material. From these equations, the number of modes that can be propagated with a thickness of 15 μm is over thirty, with $\theta_m = 74°$. According to the gap map for SU-8 photo-resist, there exists an E field polarization gap and an H field polarization gap, but not a complete two-dimensional PBG (Figure 4.26). The E field polarization band gap will be used and is shown in Figure 4.26, where the periodicity and radius are 320 nm and 134 nm, respectively.

Now that the periodicity and radius have been determined, the laser beam angles for the holographic process must be determined. From Appendix E, Figure 4.27 was generated, providing a periodicity of 320 nm and an outer intensity ring that provides a radius of columns to be 134 nm that is based on the following angles: $\theta_{1,2,3} = 50°$, $\phi_2 = 120°$, $\phi_3 = 240°$ and $\alpha = 10°$. The angles θ and ϕ are evident as shown by Figure 4.25, and α is the polarization of one of the laser beams. For a more in-depth understanding, reference Appendix E.

For this holographic technique, a UV laser beam of wavelength, 364.8 nm, was used. The liquid crystal/polymer solution has a 25 percent solution of liquid crystal. Thus, for the liquid crystal/polymer solution, the best separation that could be attained is a volume fraction of 25 percent. This particular solution has acetone in it which evaporates the liquid crystal once the intensity of the interference pattern causes the liquid crystal to separate from the polymer. This reaction creates the columns of air; however, due to the low volume fraction, a PBG will not be realized. The liquid crystal/polymer solution is simply a quick and cheap means to determine the periodicity of the structure. The desired volume fraction should be able to be accomplished by using this final setup with SU-8 photo-resist. The liquid
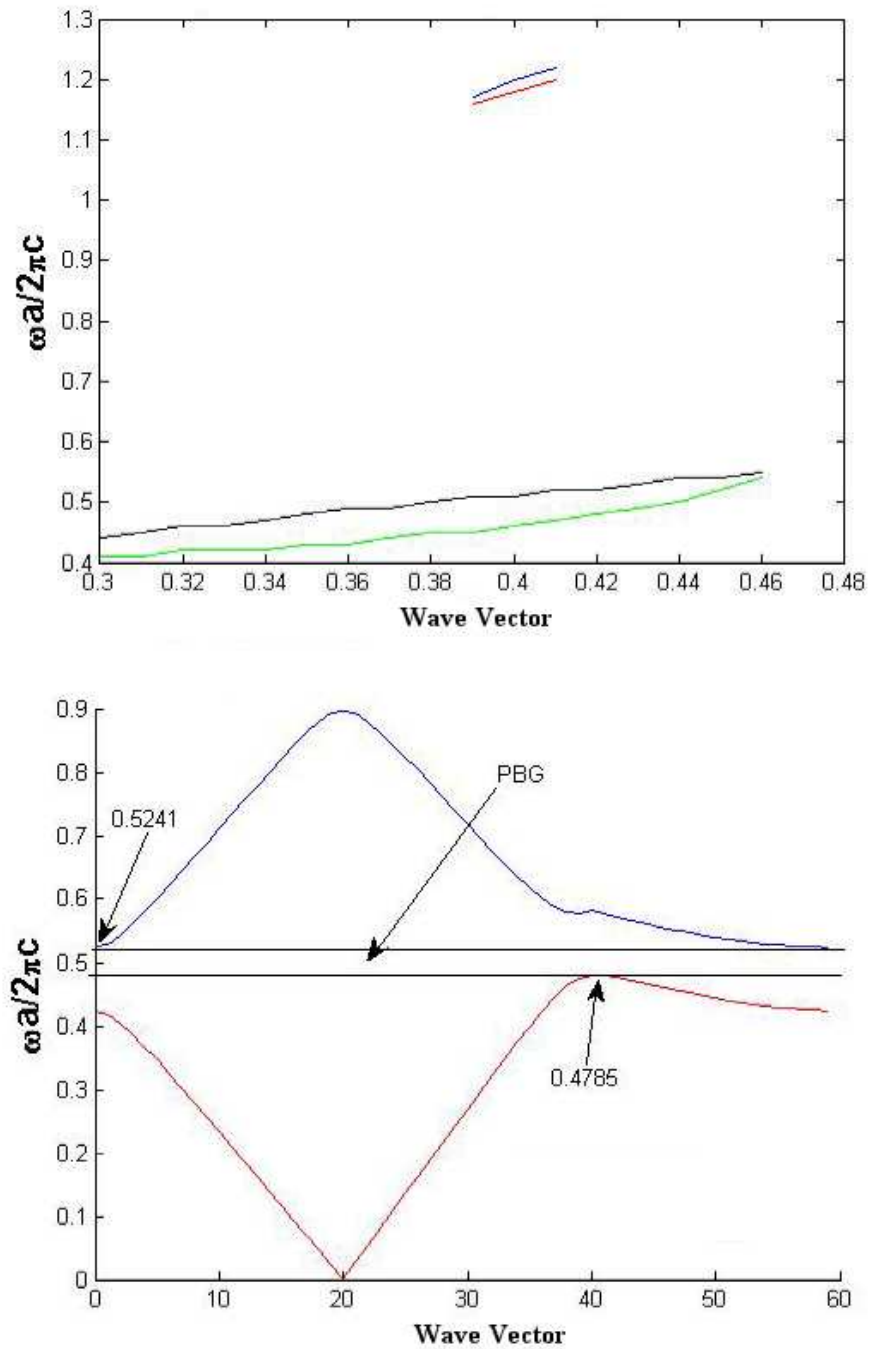
Figure 4.26: Two-dimensional triangular PhC gap map and band diagram for SU-8 negative photo-resist. (a) Gap map with a periodicity of 1 μm and radius range of 0.3-0.5 μm, where the TE field polarization band gap is shown between the green and black lines and the TM field polarization band gap is shown between the red and blue lines. (b) Band diagram of columns of air ($\epsilon = 1$) in SU-8 ($\epsilon = 2.957$) for a specific periodicity of 320 nm and a radius of 134 nm

77
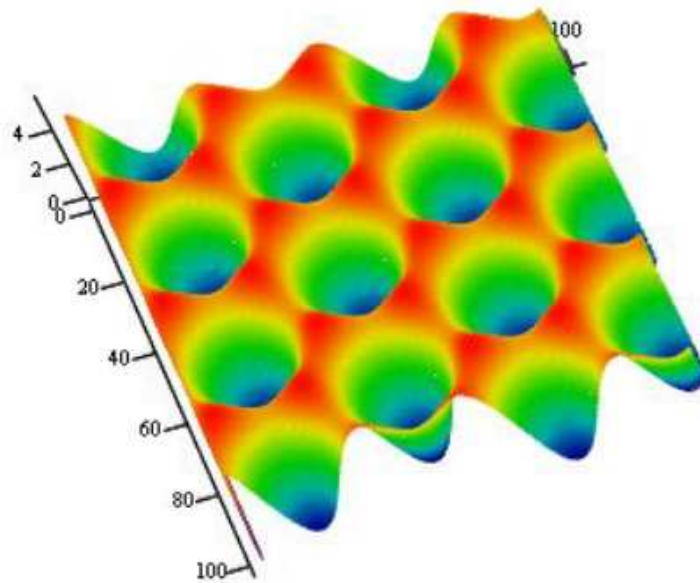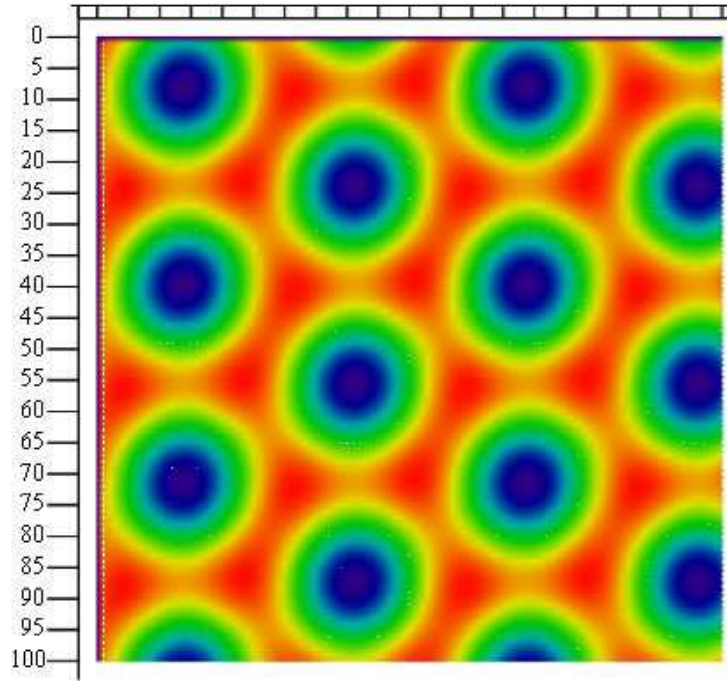
Figure 4.27: Image generated in MATHCAD® for $a = 320$ nm and $r = 134$ nm in SU-8 photo-resist, created from equations in Appendix E for the holographic laser setup used to create a two-dimensional triangular PhC design, the top and bottom pictures are different perspectives of the same graph.

78
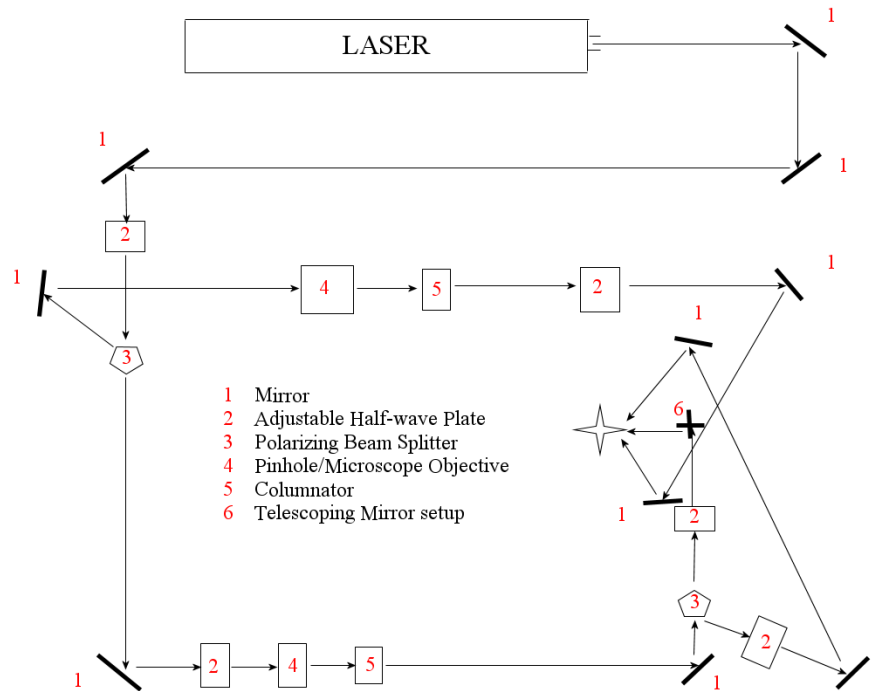
Figure 4.28: Diagram of the optical setup used in the holographic polymerization/lithography process [22].

crystal/polymer solution is 25 percent acetone, 25 percent TL213 (liquid crystal), and 50 percent DPHDA (penta-acrylate polymer), NPG (a cross linking polymer) and Ciba-geigy 4265 (photo-sensitive dye). Furthermore, upon exposure and time, this material also experiences a 3 percent shrinkage.

The optical table setup for the holographic lithography process is shown in Figure 4.28 [22]. The ultraviolet UV laser beam is basically split into two beams, then one of those beams is split again; this process creates a total of three beams. The UV laser beam is initially run through an adjustable half-wave plate that allows the polarization of the beam to be adjusted to any polarization. This will be necessary to allow for all three beams to end up with the same power at the sample surface. After the first half-wave plate, the beam is split by a polarizing beam splitter. The 's' (horizontal) beam is reflected back to a mirror, while the 'p' (vertical) beam is transmitted through the splitter. The reflected beam (this ends up being beam 2

79

or k_2 from Figure 4.25) from this optic is then fed through a microscope objective, pinhole and collimator, which provides a nice, clean, large-diameter beam. After this, it is passed through an adjustable polarizer (half-wave plate) to allow for final adjustment to the polarization of the beam incident on the sample surface. The rest of the optics are mirrors used to achieve the proper angles as designed earlier. The transmitted beam from the first splitter goes through an adjustable half-wave plate again. This is offset to a 45° angle to provide two equal polarizations for the next polarization splitter. After this, it is also run through a microscope objective, pinhole and collimator. The clean large-diameter beam is now fed through the last polarizing beam splitter. The transmitted beam ('p' polarized) becomes beam 1 or k_1 of Figure 4.25. This beam is fed through another adjustable half-wave plate to put fine tuning on the polarization as it is incident on the sample surface. Note that this beam should be polarized as a TE beam as it hits the sample surface; the mirrors used after the last beam splitter rotate the polarization so that it is TE upon the sample surface. The reflected beam ('s' polarized) from the last beam splitter becomes the third beam or k_3 of Figure 4.25, and is fed through an adjustable half-wave plate, allowing the unique offset polarization to be accomplished as it is incident on the sample surface.

A $45 - 45 - 90$ prism mounted on an adjustable z-axis plate that is on a rotational stage was used to get the alignment of the 50° angle, θ and ϕ. The prism was adjusted by 5° with the z-axis control, and that allowed for proper alignment of the beams by aligning the back reflection directly with the incoming beam; this process was accurate to within 2°. The polarization was checked by placing a polarizer, adjusted to block the desired polarization, at the sample position, and then adjusting the last-in-line half-wave plate of the beam until the beam was completely blocked. Finally, by placing a power meter at the sample location, each beam's intensity was checked and equalized to each other by adjusting the first-in-line half-wave plate. Each beam was measured to be 3.3 mW/cm^2 $\pm$ 0.1 mW/cm^2.

Again, as part of the evaluation of the FDTD software, Crystalwave was used to model two-dimensional PhC's in SU-8. These calculations used a Gaussian con-
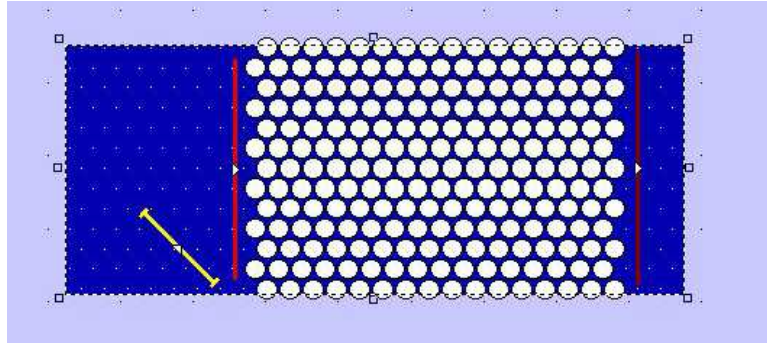
Figure 4.29: Graphical interface display in Crystal-wave software for the SU-8 design.

tinuous wave mode exciter as the source, and all the calculations were accomplished assuming the boundary conditions to be infinite in the y direction (*i.e.*, infinite column lengths). The GUI of the setup showing the mode exciter at a 45° incidence is shown in Figure 4.29.

The results of the modeling at 0° and 45° degree incidence were calculated. Figures 4.30-4.34 are various FDTD depictions and Fourier analysis graphs for this PhC in SU-8. Due to the boundary conditions of the simulation, it is shown in Figure 4.31 (a) and (b) that, for the E_x case, due to extra bounces outside of the PhC, the transmitted probe could be higher than the reference reading; however, it is shown in Figure 4.30 (a) that the wave is greatly attenuated as it transits through the PhC. These figures indicate that this is a good design for a PBG at 632.8-nm in SU-8 photoresist. The band diagram for the structure in the SU-8 material was also modeled in the Crystalwave software as another verification of the software being evaluated. Figure 4.34 shows the band diagram of the SU-8 material with a periodicity of 320 nm and a radius of 134 nm using a triangular structure. Again, this figure can be compared to that obtained using gap maps in Figure 4.26 for the same structure. This band diagram is also shown with units of wavelength in Figure 4.34 (b).

81
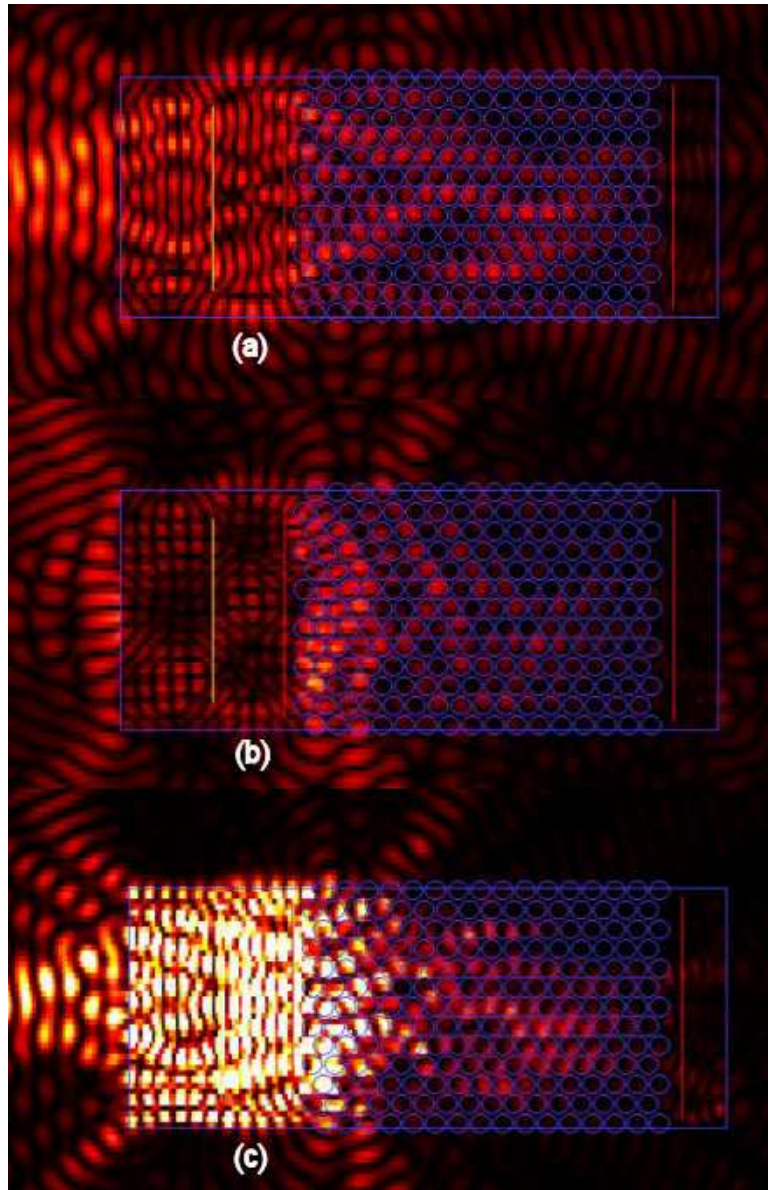
Figure 4.30: PhC design in SU-8 with a periodicity of 320 nm and a column radius of 134 nm excited by a 632.8-nm Gaussian mode at a 0° incidence showing the (a) E_x field and (b) E_z field and (c) intensity.
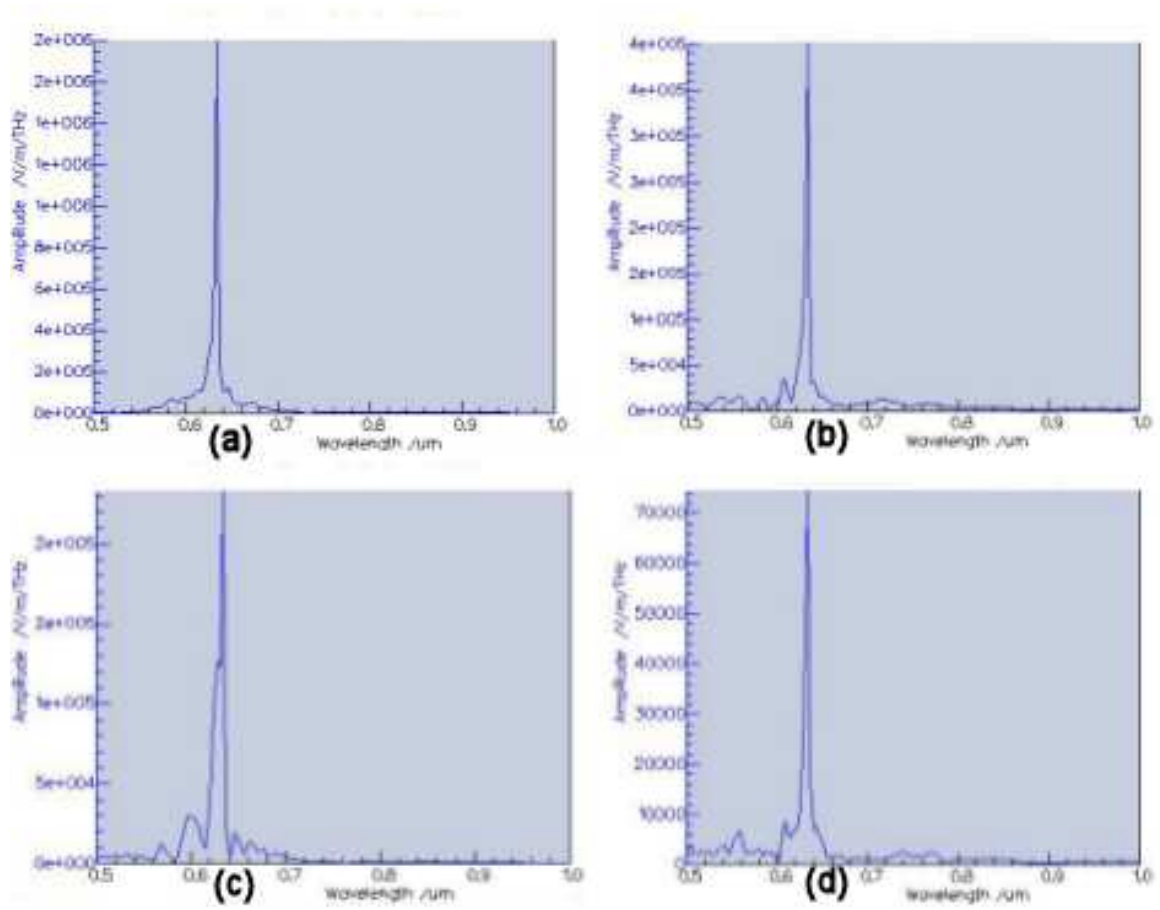
Figure 4.31: PhC design in SU-8 with a periodicity of 320 nm and a column radius of 134 nm excited by a 632.8-nm Gaussian mode at a 0° incidence showing (a) the reference E_x amplitude and (b) the transmitted E_x amplitude and (c) the reference E_z amplitude and (d) the transmitted E_z amplitude.
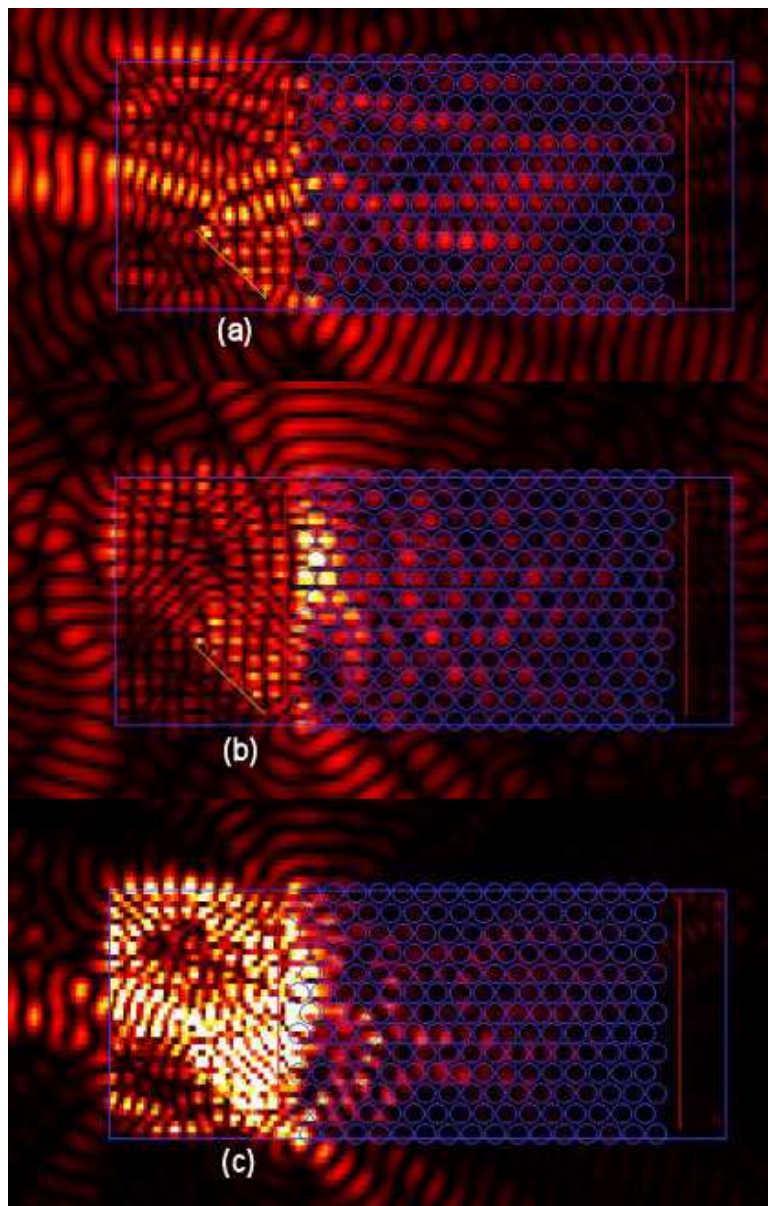
Figure 4.32: PhC design in SU-8 with a periodicity of 320 nm and a column radius of 134 nm excited by a 632.8-nm Gaussian mode at a 45° incidence showing the (a) E_x field and (b) E_z field and (c) intensity.
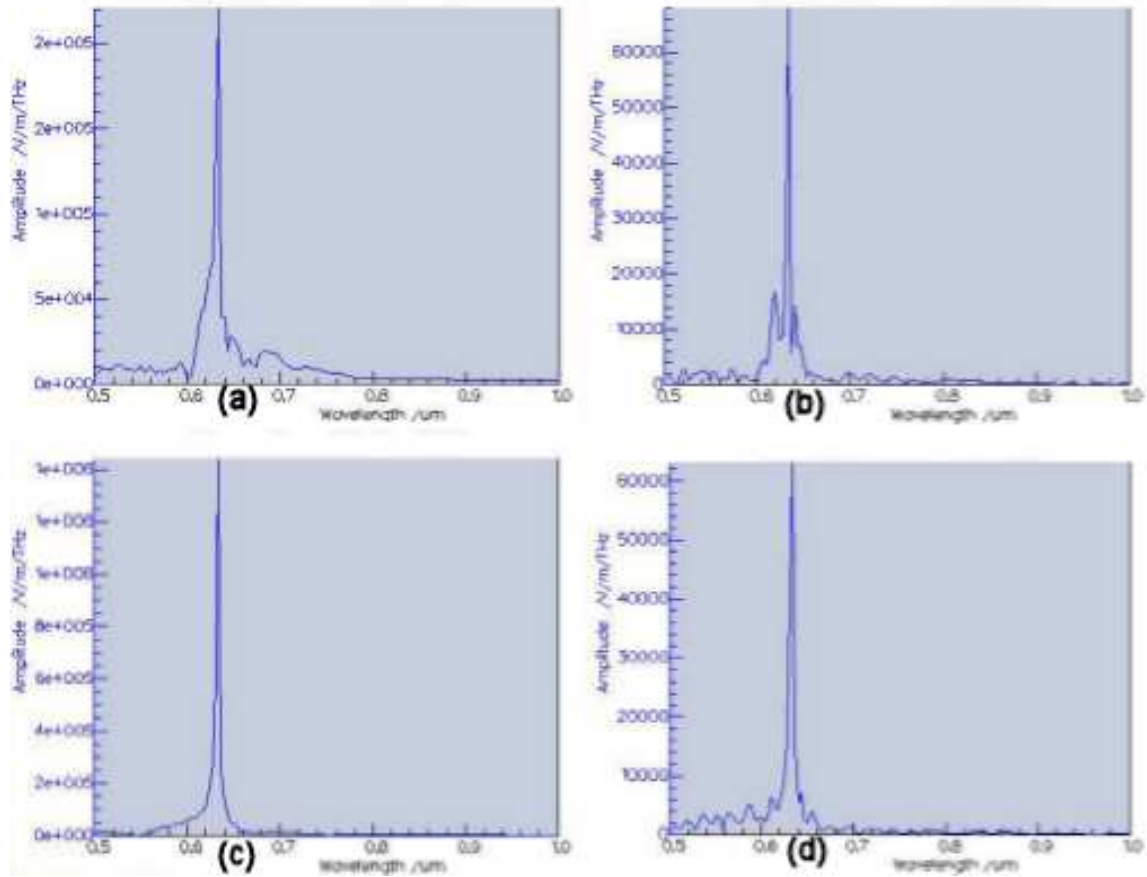
Figure 4.33: PhC design in SU-8 with a periodicity of 320 nm and a column radius of 134 nm excited by a 632.8-nm Gaussian mode at a 45° incidence showing (a) the reference E_x amplitude and (b) the transmitted E_x amplitude and (c) the reference E_z amplitude and (d) the transmitted E_z amplitude.

85
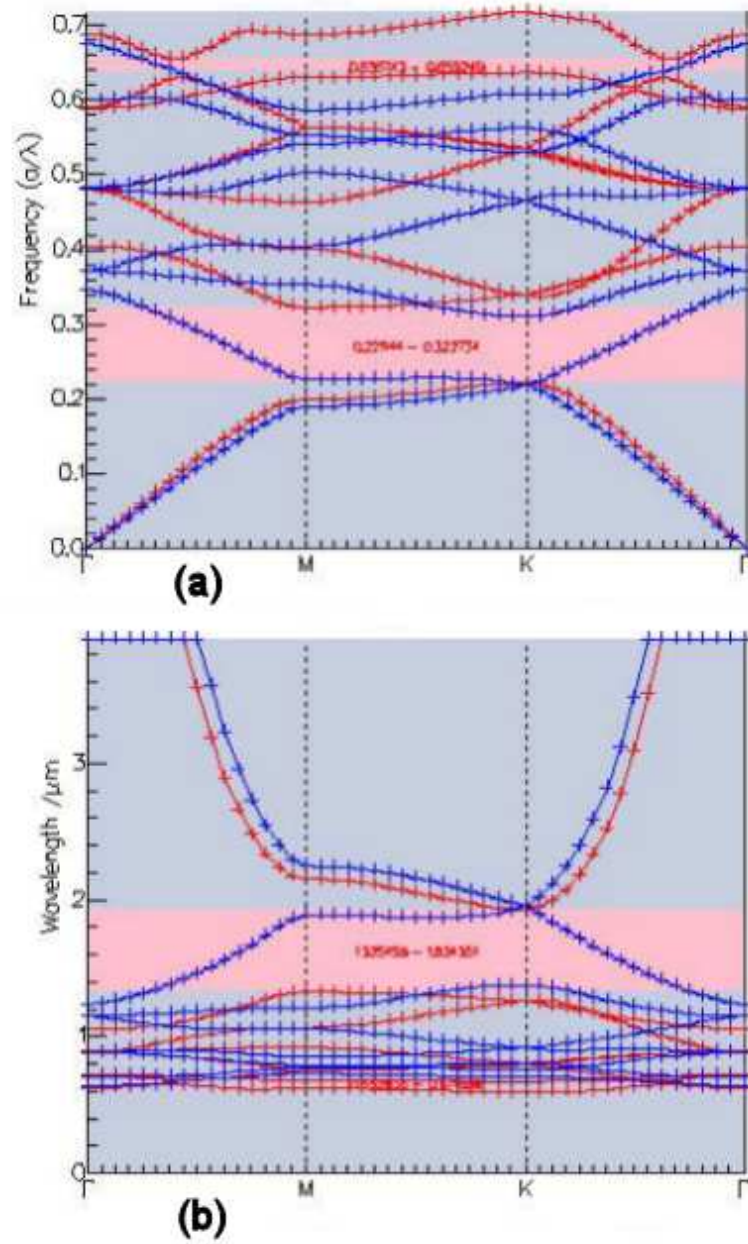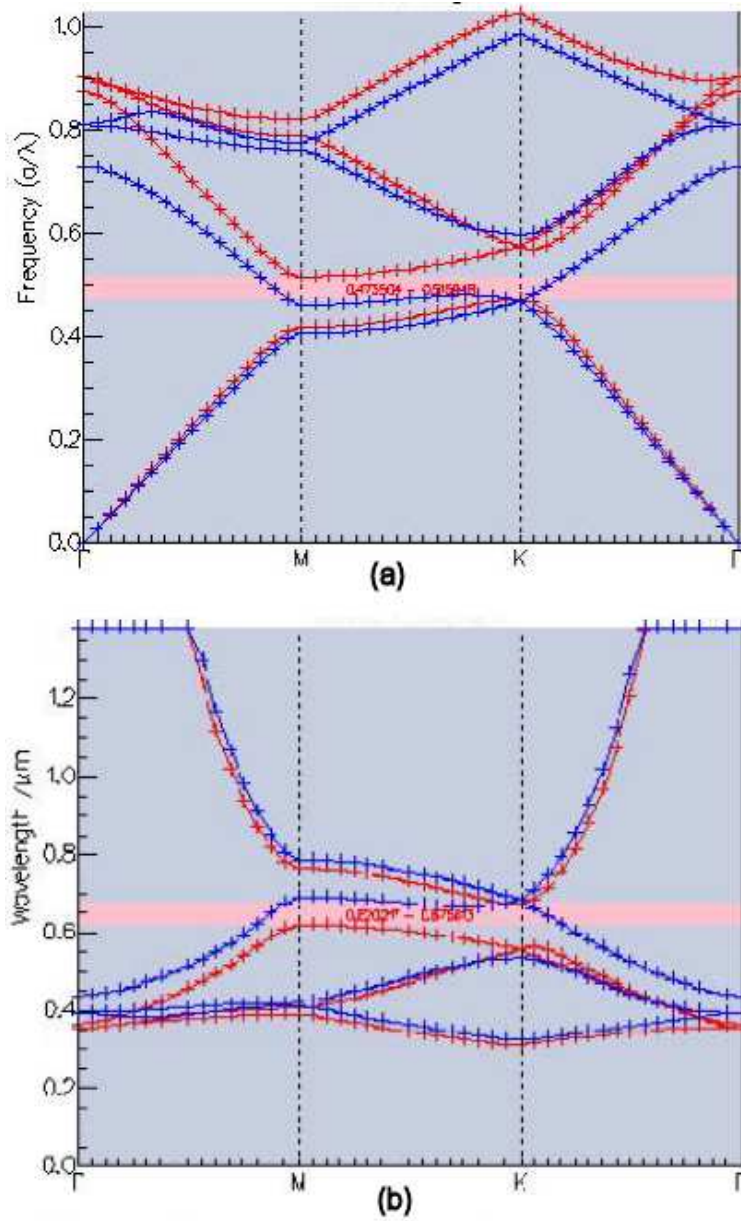
Figure 4.34: Band diagram of SU-8 modeled with Crystalwave software for a periodicity of 320 nm in a triangular pattern showing a TE band gap in units of (a) frequency (TE gap of 0.473504-0.515948 a/λ) and (b) wavelength (TE gap of 0.675813-0.620217 $(\mu m)^{-1}$).

4.4 Holographic Lithography Technique of Three-Dimensional Face-Centered-Cubic Photonic Crystals

Hybrid Technologies of Amherst, New York, uses a holographic lithography technique to create three-dimensional fcc structures [3]. They use an "umbrella" technique with their setup, incorporating two different polarizations of the beams. Their design is adopted from Miklyaev *et al.* [26] and Meisel *et al.* [6]. The basic setup of the design is based off of four laser beams. Three of the beams are set up in much the same way as the previous holographic technique for two-dimensional PhC's (with only two different polarizations). The fourth beam is perpendicular to the sample. Figure 4.35 shows the recording geometry used by Hybrid, where k_1, k_2 and k_3 are the wave vectors of the three side beams, and k_o is the perpendicular beam [3].

These beams form a tetrahedron with a base parallel to the x-y plane. The height of the tetrahedron is governed by the fourth beam, k_0. The samples they created are PhC's designed for the infrared range. Each side beam of the tetrahedron forms a 39° angle (in the air) with the central beam [3]. With regard to the polarization, two different setups are used. The first setup is shown in Figure 4.35 (a); the second setup is shown in (b). The first setup illustrates the polarization of each beam as it is oriented so that their projections on the x-y plane form a 30° angle with the x direction. The second setup has the center (perpendicular) beam polarized in a circular manner, and the three side beams are polarized with respect to their plane of incidence. Figure 4.36 is an SEM of the FCC structures created by the "umbrella" technique in SU-8 negative photo-resist. The expected PBG for these structures is around the 2.5-2.9-μm wavelength range.

4.5 Conclusion

The exploration of fabricating a PhC with a PBG in the visible range is necessary for continued advancement the field of PhC's. In this chapter, the design of two-dimensional triangular PhC's for fabrication by focused ion beam, holographic polymerization/lithography, and electron beam lithography techniques were shown.
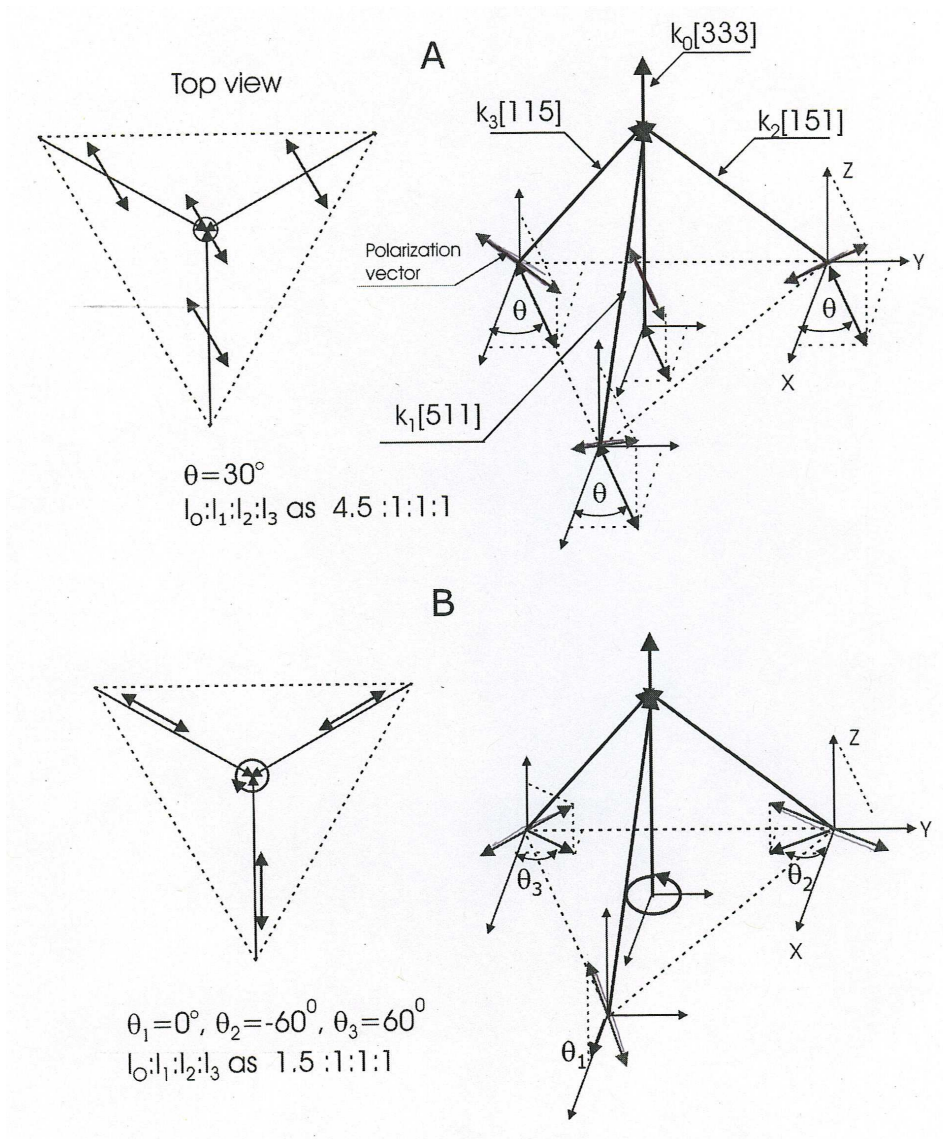
Figure 4.35: Hybrid Technologies laser beam recording geometry for three-dimensional FCC PhC's. (a) Shows the setup for the polarization of all the laser beams projected polarization on the x-y plane forms a 30° angle with the x axis; (b) shows the setup for the polarization of center beam to be circular where as the projection of the side beams (1, 2, and 3) on the x-y plane form a 0°, −60° and 60° angle respectively, with the x axis. [3].
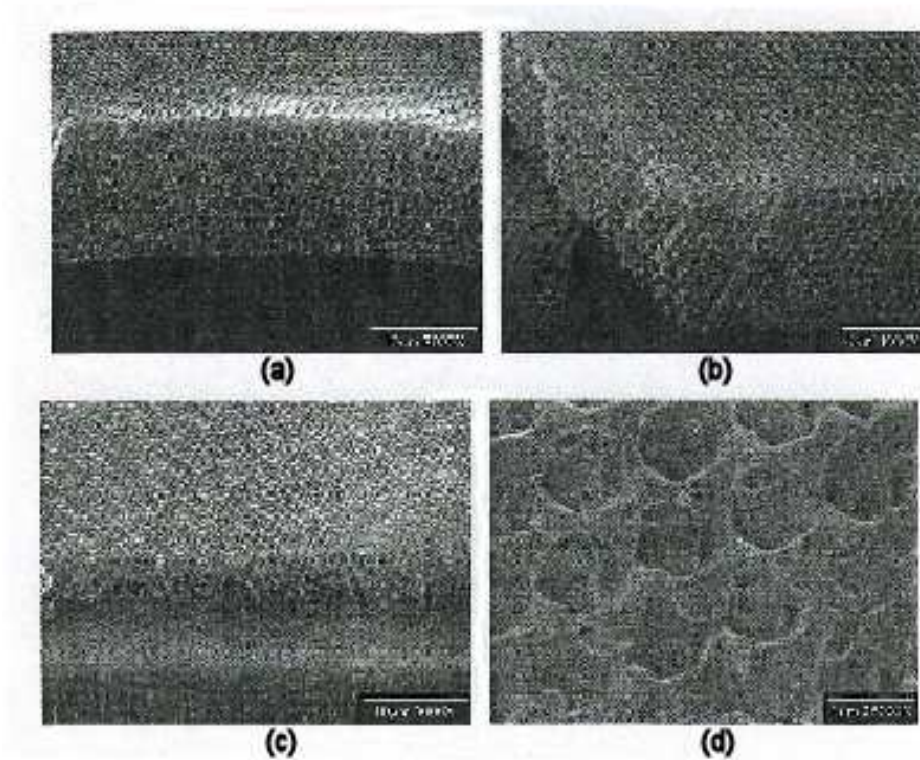
Figure 4.36:   SEM images of FCC structure created in SU-8 by Hybrid Technologies using holographic process, (a), (b), (c), and (d) are different views and magnifications of a sample PhC they fabricated [3].

89

Depending on the type of characterization that is going to be used on these PhC's, the type of design implemented must be determined. Therefore, depending on the fabrication process, certain preliminary steps must be accomplished prior to the creation of the PhC. The focused ion beam fabrication technique required the fabrication of a mask for the guided beam, *i.e.*, the reason for the gold strip as was shown in this chapter. The main point to grasp from this chapter is that to obtain a PhC with a PBG in the visible wavelength range requires the size of the PhC features to be on the nanometer scale. The possibility for these designs to produce a PhC with a PBG in the visible wavelength range was shown to be possible in theory. Next chapter will explore the results of fabricating these two-dimensional triangular structured PhC's designed in this chapter for the techniques previously listed. Some discussion into the setup for the different testing techniques will be discussed, as will the results of the PhC's that were able to be fabricated.

V. Fabrication and Testing Results and Analysis of the Focused Ion Beam, Electron Lithography and Holographic Lithography Fabrication Techniques

The theoretical possibility for PhC's to be fabricated by the processes listed in Chapter IV, were shown to be viable. Chapters I and II presented the history, theory and previous experiments of PhC's and were used as a basis for the calculations of Chapter IV. Chapter III introduced a necessary design tool, FDTD software, used to model PhC designs to prevent wasted time and money during the fabrication stage. To actually use the techniques considered in this thesis to fabricate the PhC's designed in Chapter IV will be explored in this chapter. The results of testing these PhC's depended on the ability to fabricate these structures. The rest of this chapter details the results of each fabrication technique outlined in the previous chapter and displays these results.

5.1 Focused Ion Beam Fabrication and Testing Results

The process for the FIB technique was outlined in the previous chapter. The results displayed in the previous chapter are of the more successful attempts; however, the process involved to obtain these results is not so obvious. The first gold channel that was deposited due to shadow masking was extremely wide and deep. The second attempt required making a much finer shadow mask and decreasing the deposition thickness to lessen the channel cutting time of the FIB. This better sample had a gold line that was approximately 56-μm wide and 1.5-μm deep. Figure 5.1 is a magnification of Figure 4.1 which shows that the FIB cut down into the substrate on the first sample, not just through the gold strip. This unevenness to the waveguide layer could cause mode loss or decoupling properties.

On subsequent trials, more care was taken to only cut down to the substrate to help prevent any problem this may cause. Also, from Figure 5.1, it can be seen that the gold appears to have bubbled away from the indium tin oxide (ITO) layer. The manufacturer of the FIB machine advertises that there is no heating with the

91
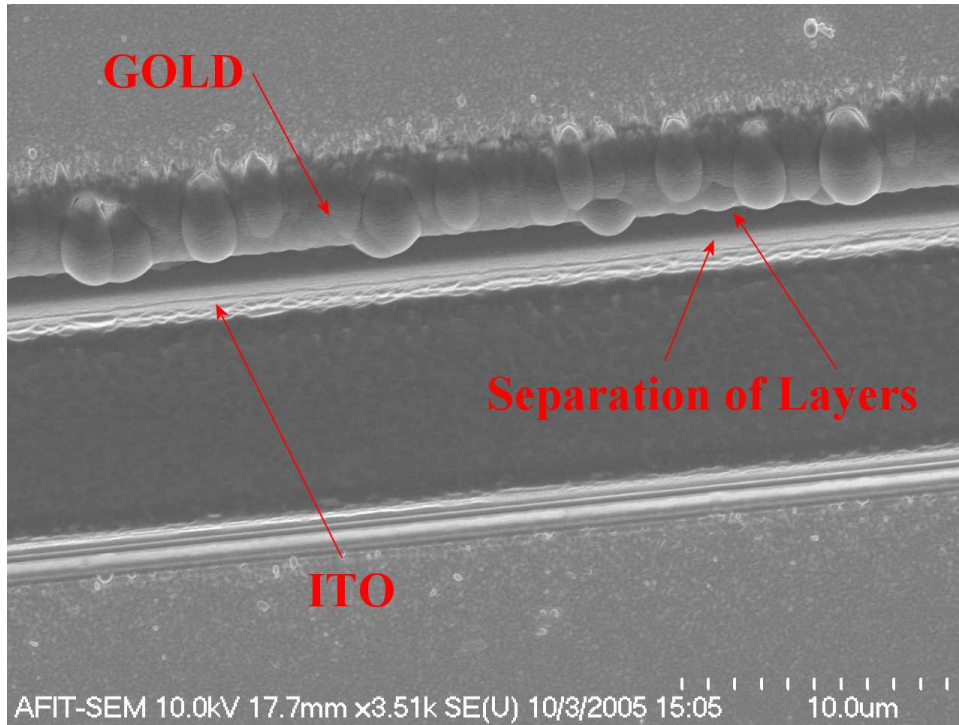
Figure 5.1:   SEM image of gold channel used in the FIB process, showing the layers penetrated by the FIB. It is shown that the gold layer actually bubbled and separated from the indium tin oxide (ITO) layer below it.

FIB process. This image suggests that at some level there is enough heating effect to cause the problem seen in Figure 5.1. This effect may be lessened or negated if the ion beam power is decreased. The ion beam was set to 5,000 pA for the cutting of the channel and the channel cutting process was continually monitored to determine when the gold was cut through. Figure 5.2 shows the initial cut of the channel; notice the irregularities of the gold surface. The deposition of the gold was not as high a quality as normal. The cutting of the gold channel left some residual gold at the ends; this was cut away by dropping the power of the ion beam to 300 pA and isolating that area so as not to cut down into the substrate. Figure 5.3 is the final channel cut into the 56-μm wide gold stripe. A comparison of Figure 5.3 to the first gold channel cut, Figure 4.1, shows the quality of the new channel is obviously better.

The previous fabrications were designed so that the gold would act as the mask for the waveguided beam. Another attempt was to replace the gold stripe with air for this purpose. In other words, there would be a channel of material (APC or silicon nitride) between large expanses of air. This was attempted with APC and is shown in Figure 5.4. The reason for the mess of Figure 5.4 is due to charging in the FIB which caused drift and the re-deposition of material. The average drift for which this FIB is rated is 7 nm per minute. The drift shown in Figure 5.4 was much greater than that; however, even 7 nm per minute is enough to destroy the PhC that is being created due to its small size. There was a line of ITO under the APC area that was being etched by the FIB; however, the charging effect due to the APC was too great. Applying a carbon coating in order to control the charging effect was not an option as it would hinder the ability to prism couple a beam into the APC layer. Through subsequent trials, the drift was used to aid in the etching process instead of hindering it, until the proper channel width and air gap was achieved. Figure 5.5 shows this progression. However, being able to manipulate the charging effect to benefit the experiment may be possible for a rectangular object of this large size, but for circular objects on a small scale (300 nm), it is a different matter. For this reason, it was not possible to fabricate PhC structures of a visible wavelength range in this material by

93
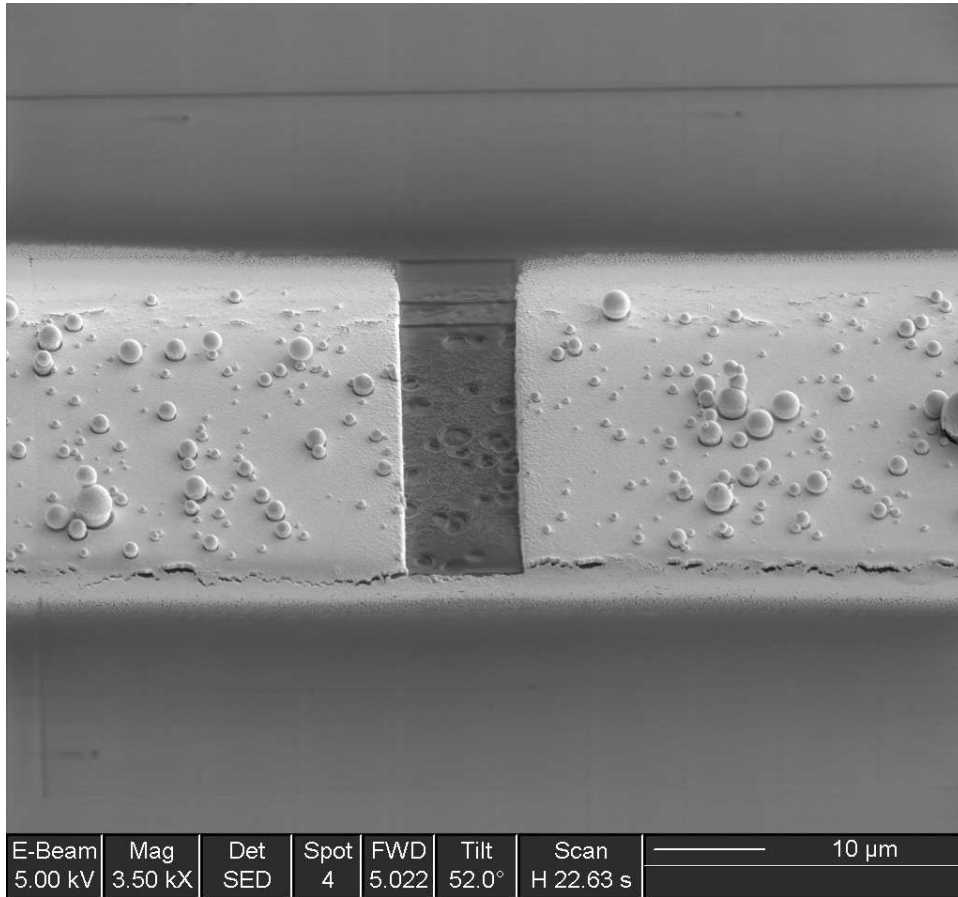
Figure 5.2: SEM image of the gold channel after initial cutting; notice the gold residue left in front of the channel that must be cut away using 300 pA power.
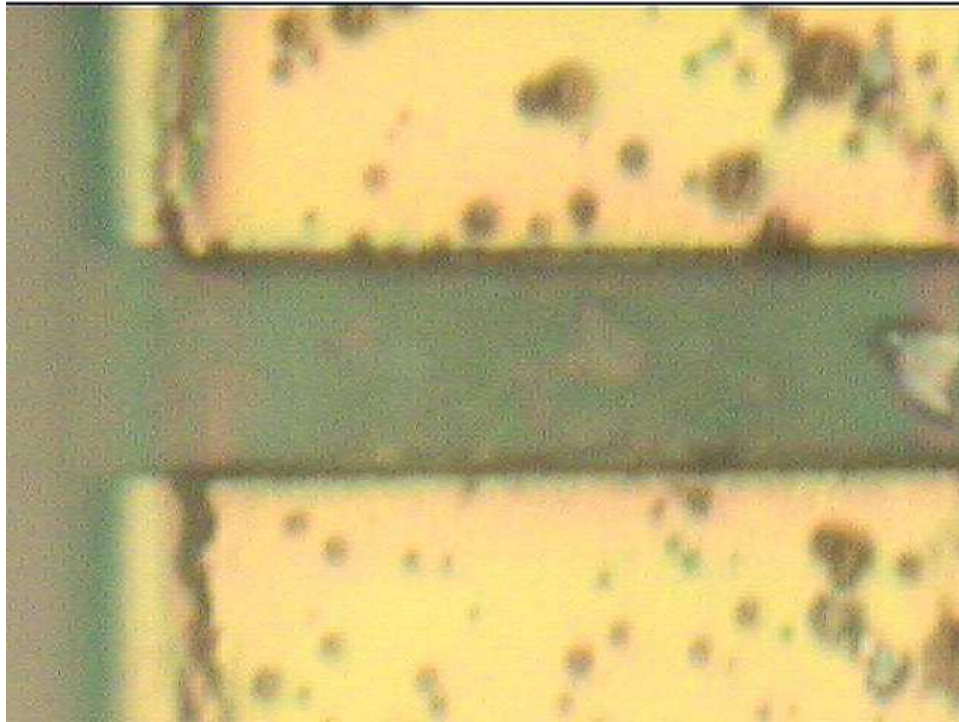
Figure 5.3:   50X microscopic image of the gold channel after the residue was blasted away.

the FIB.

One of the PhC attempts with the FIB was creating a metalloid PhC (a PhC in the gold). The purpose of this was two fold. First, since creating a PhC in the waveguiding material directly was impossible, this would demonstrate the ability of the FIB to create a PhC on that scale. The second was to create a PhC of the visible wavelength that, instead of using the PBG to block a specific wavelength region, capitalizes on one of the unique properties of PhC's which is the enhanced transmission at the band edges of the PBG. It is known that gold would block this range of the visible spectrum; however, due to the PhC, there can be transmission through the gold. Figure 5.6 shows an attempt that was made in the first gold strip sample. This attempt was created by etching the channel first and leaving some gold at the end, then etching the PhC in the remaining gold. As can be seen from Figure 5.6, not only did the PhC get etched too deeply, but the gold that was left was not a straight side wall. The deposition left slanted sides, as well as did the FIB process.

95
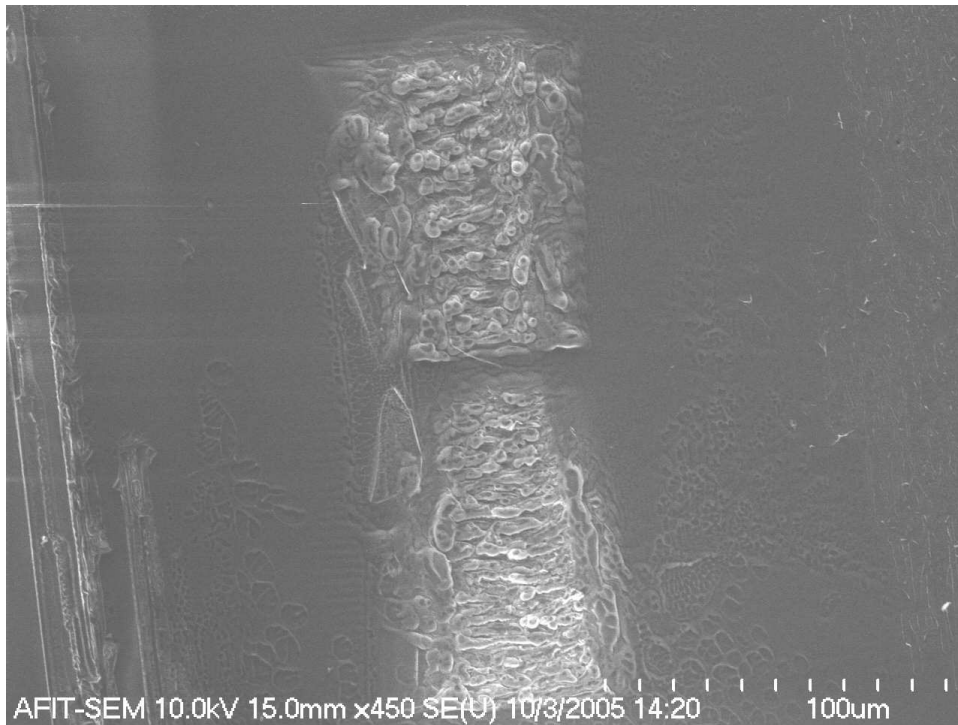
Figure 5.4: SEM image of the attempt to use air as a mask for the beam leaving a 10-μm wide channel. Due to bad drift and re-deposition of material, it can be seen that the FIB process contains too high of charging for this material and the effects of drift cause the results seen here, $i.e.$, a non-usable mess.

96
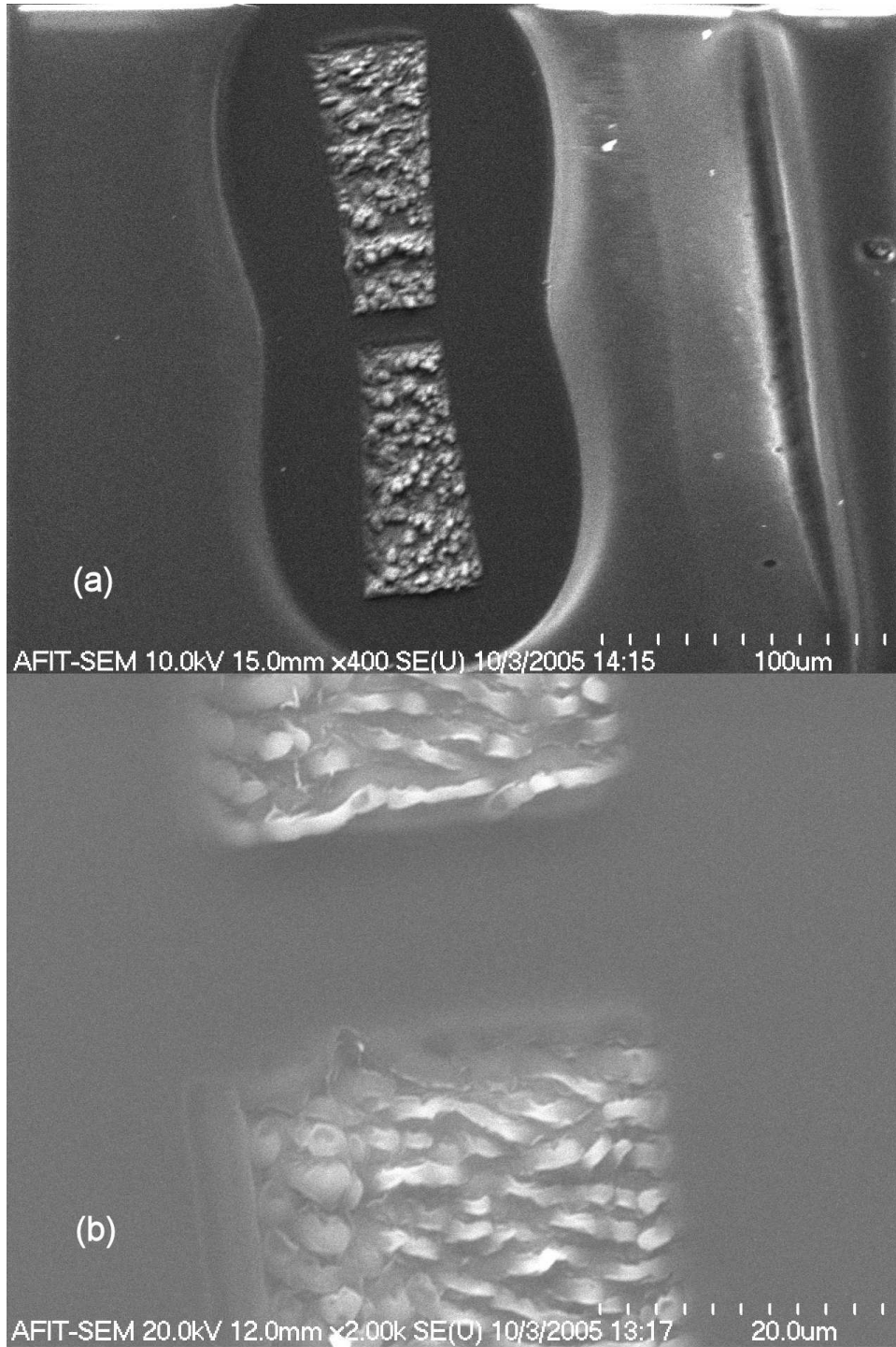
Figure 5.5: SEM image of APC channel in air, (a) with better drift correction and (b) with best drift compensation to achieve approximately 15-μm channel of APC in air. (b) Is also magnified to a 20-μm scale.

Figure 5.6 also shows a top-down view of this occurance; notice the stitching errors and the random mistakes of the columns created by the FIB process. This is most likely due to the power selected for the ion beam during etching.

Figure 5.7 is the top-down view of the second trial attempt with the 1.5-μm deep gold line sample. The stages for this fabrication started with the fine etching away of the slanted gold side left from the deposition. Next, the PhC was etched into the gold (Figure 5.8), which shows how the FIB etching process unevenly eats away at the top of the structure as the etch goes deeper. Finally, the etching of the channel in the gold was accomplished as shown in Figure 5.8.

The first test sample received a deposition of silicon nitride, and the second test sample (1.5 μm of gold) received coatings of APC as their waveguiding media. Unfortunately, the second test sample was destroyed in the coating process and could not be put back into the FIB for the final etching of the PhC structures in the APC; however, it could still be evaluated to determine the waveguiding characteristics into the channels and up to the gold PhC. The first test sample was never taken back for its final etching process; due to charging effects, the PhC's would not be able to be produced. However, it too could be evaluated by waveguiding into the silicon nitride and observing the effects as it is incident on the structures. The process of prism coupling, as shown in Appendix B, portrays the necessity to have the prism at a higher index than that of the waveguide material. For silicon nitride, this means an index higher than 2.0. While there are several prisms that can achieve this, the least expensive is a rutile prism. However, due to the birefringence of this crystal, waveguiding into this sample was unable to be accomplished. Waveguiding into the APC (index of 1.57) is easier, as a non-birefringent prism could be used. The test setup for waveguiding a helium neon laser using a prism coupling technique is illustrated in Figure 5.9.

The helium neon laser is fed through a pin hole and a collimator; then, it is fed through an adjustable polarizer that is set to only pass horizontal waves (for this set up, creating the TE polarization). An adjustable aperture is used to decrease the size
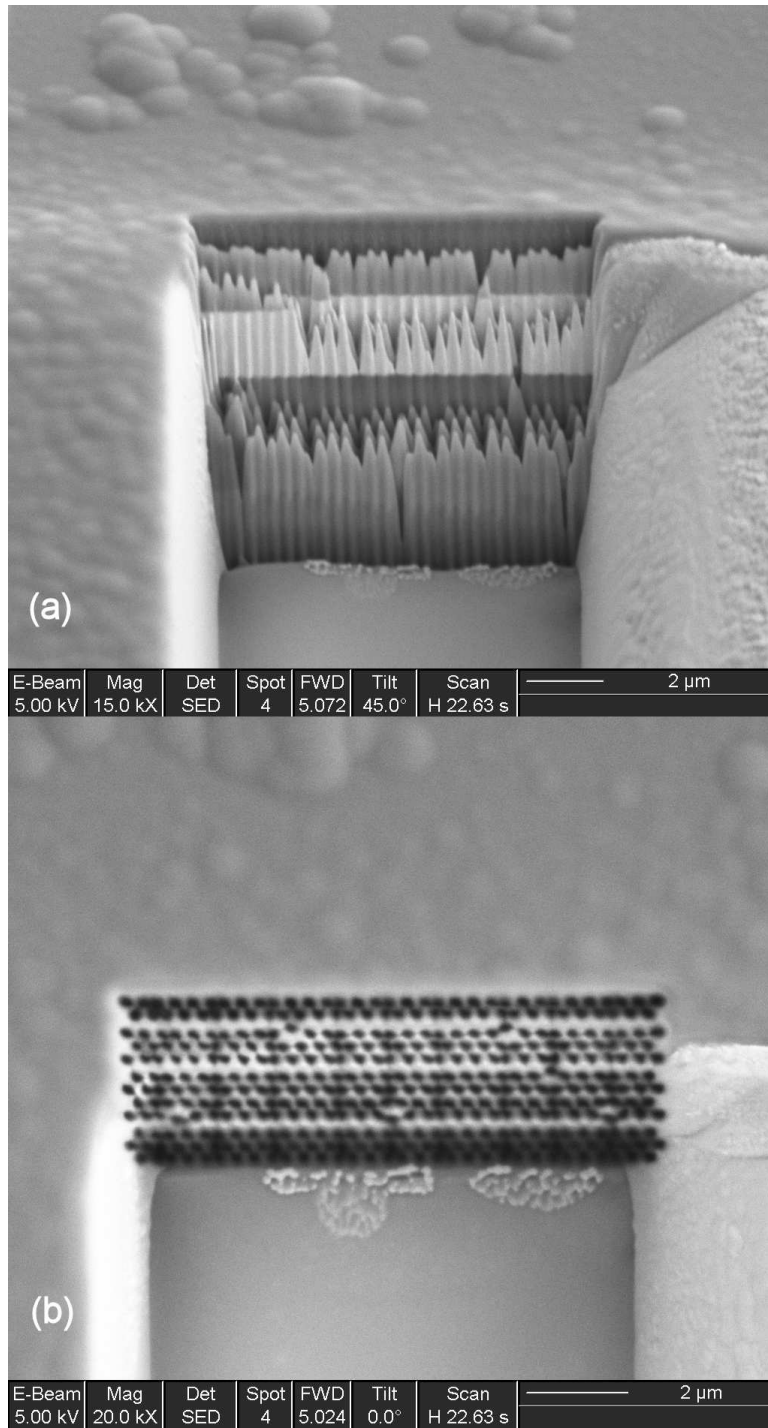
Figure 5.6: SEM image of metalloid PhC in gold, (a) 45° look angle at the metalloid PhC in gold and (b) top-down view of metalloid PhC in gold.
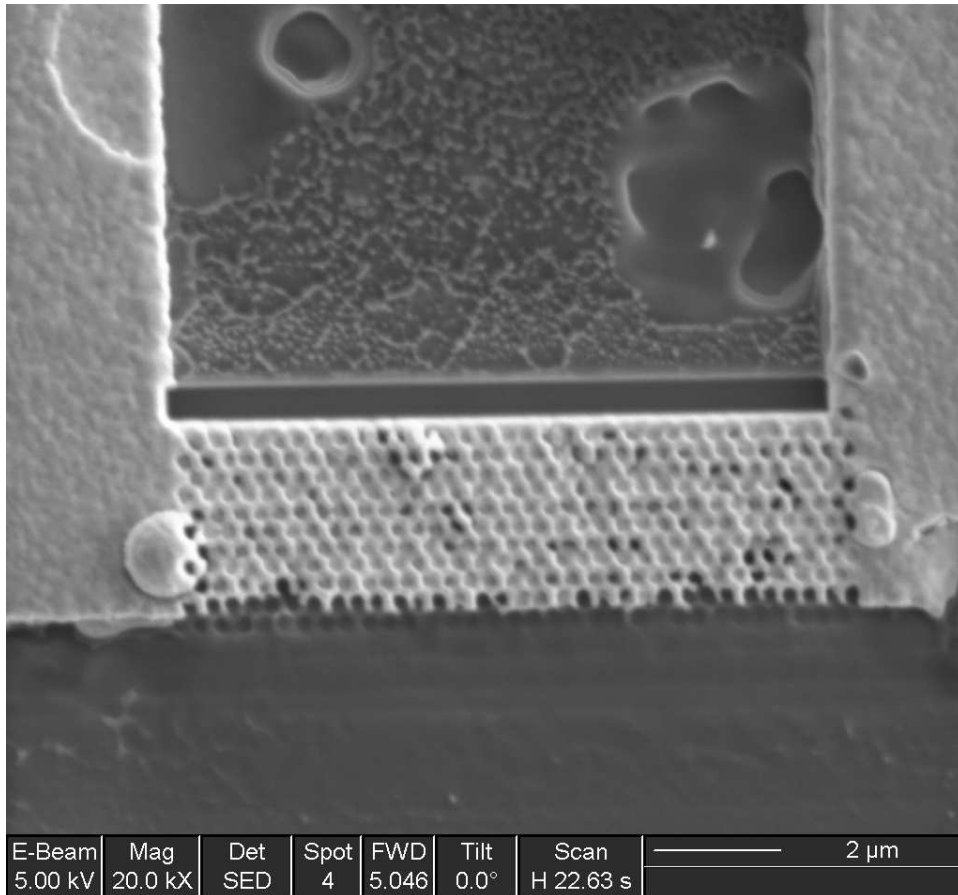
Figure 5.7: SEM top-down image of PhC in gold where the gold strip was of better quality and the etching process was at a much lower power and more care was taken to try and not etch deeper than the gold layer.
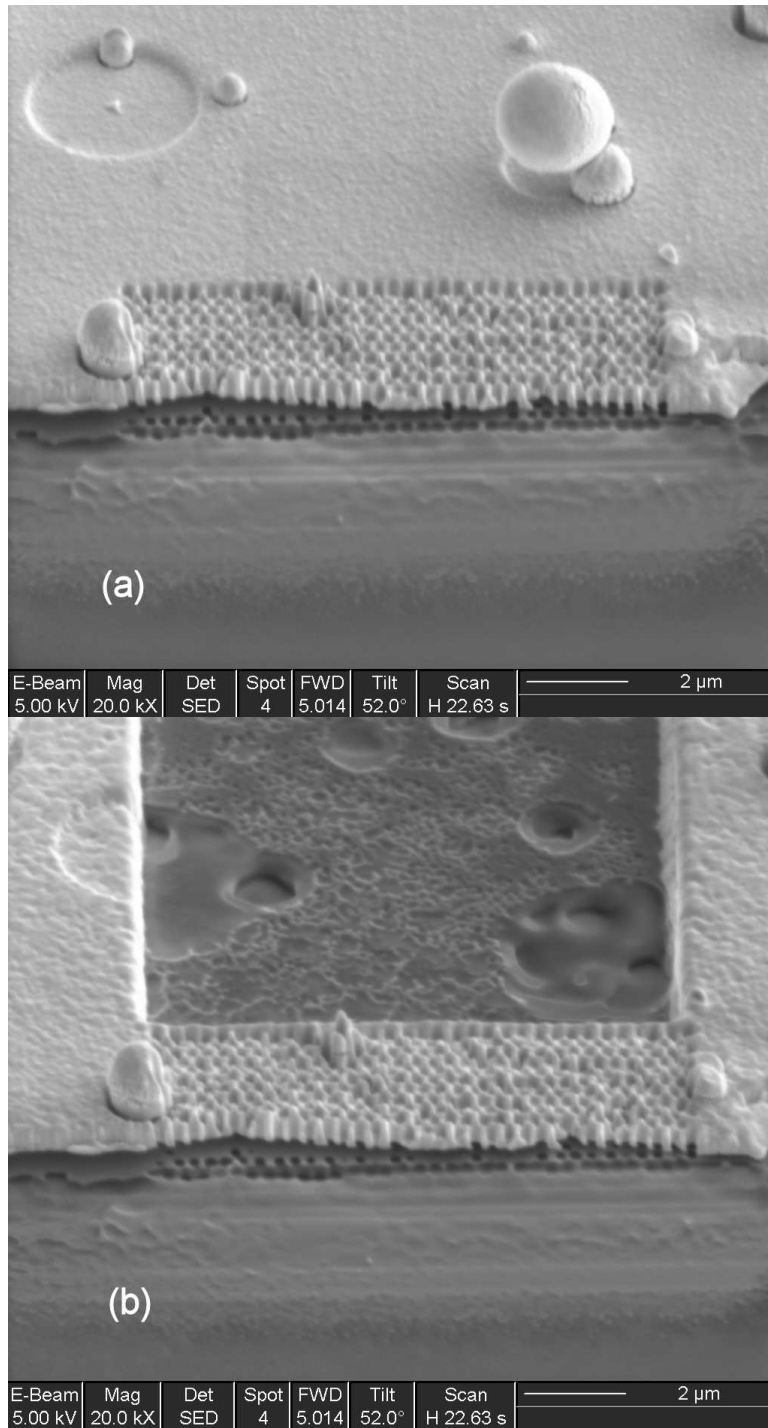
Figure 5.8: SEM image of a couple of stages of the FIB process for the PhC of Figure 5.7, where (a) shows the initial etching away of the gold over spray and the etching of the PhC, and (b) shows the final stage of the channel being etched away behind the PhC.

101
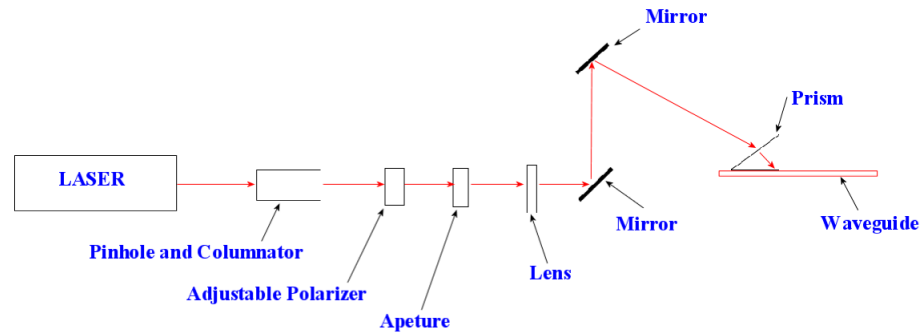
Figure 5.9:   Side view of the optical setup for prism coupled waveguiding.

of, and clean up, the beam. Figure 5.10 shows a Beamcode image of the beam being used. Next, a 150-mm focal length lens is used to focus the beam to a point. The focal length should be longer than the distance needed to couple into the prism. Two mirrors in a penscope configuration are used to raise the beam to obtain the proper angles necessary for the prism coupling effect. The top mirror is on a micrometer adjustable stage for fine control of the angle. Figure 5.11 shows the channel in gold as it is being waveguided to by a 632.8-nm helium neon laser with an incident angle of approximately 30°, using a 50X objective on the microscope. Figure 5.11 (a) shows the channel in the gold with the light on and (b) shows the same channel with the light off. Notice the trash in the channel from Figure 5.11 (a); this should give a good specular reflection if the beam is guiding in the channel. From Figure 5.11 (b), it can be seen that there is no scatter detected from the channel. This could be due to the detectivity of the camera used to record this image. A near-field scanning optical microscopy might be able to detect the presence of a guided mode in the channel, or light may not be guiding down the channel. Waveguiding to the channel with a normal incidence angle also showed no scatter down the channel, indicating no mode was successfully propagated down the channel.

If the wave is not propagating down the channel, it could be due to the coupling of the slab waveguide to the channel waveguide. This situation was simulated and
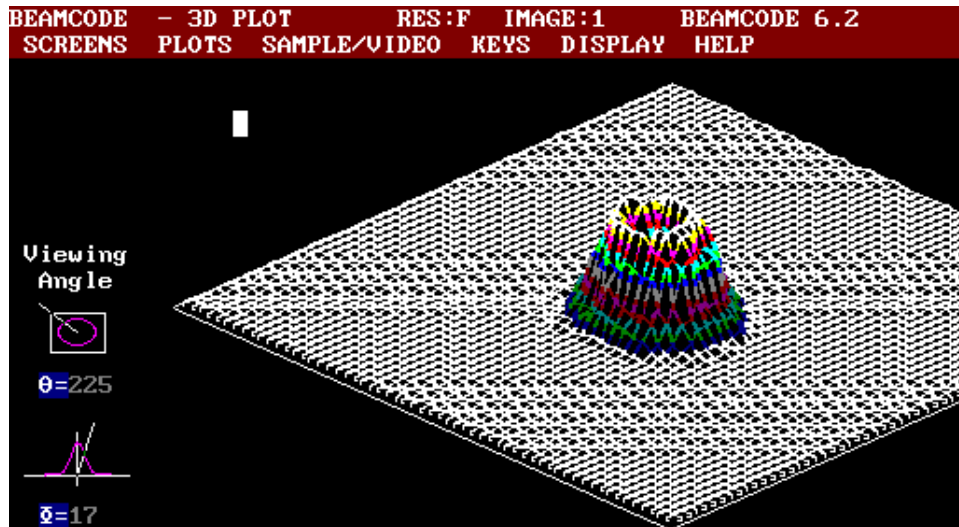
Figure 5.10: Beamcode image of the HeNe laser beam used for prism coupling.

the results of that simulation suggest that the waveguided mode should couple into the channel. Part of the evaluation of the FDTD software included the modeling of waveguiding. The modeling results of the coupling the slab waveguided beam to a channel, in the gold, is illustrated in Figure 5.12. Figure 5.12 (a) is the E_x field (b) is the E_z field and (c) is the intensity, all at a $0°$ incidence on the gold channel. The graphs of Figure 5.13 shows the amplitude of the E_x wave at $0°$ incidence as the beam enters the channel, as shown in (a), and the amplitude of the beam as it exits the channel, as shown in (b). Likewise, Figures 5.13 (c) and (d) show the amplitude of the E_z wave at $0°$ incidence as it enters and exits the channel, respectively.

Figure 5.14 (a) is the E_x field (b) is the E_z field and (c) is the intensity, all at a $10°$ incidence on the gold channel. The graphs of Figure 5.15 shows the amplitude of the E_x wave at $10°$ incidence as the beam enters the channel, as shown in (a), and the amplitude of the beam as it exits the channel, as shown in (b). Likewise, Figure 5.15 (c) and (d) show the amplitude of the E_z wave at $10°$ incidence as it enters and exits the channel, respectively. Figure 5.16 (a) is the E_x field (b) is the E_z field and (c) is the intensity, all at a $45°$ incidence on the gold channel. The graphs of Figure 5.17 shows the amplitude of the E_x wave at $45°$ incidence as the beam enters the channel,

103
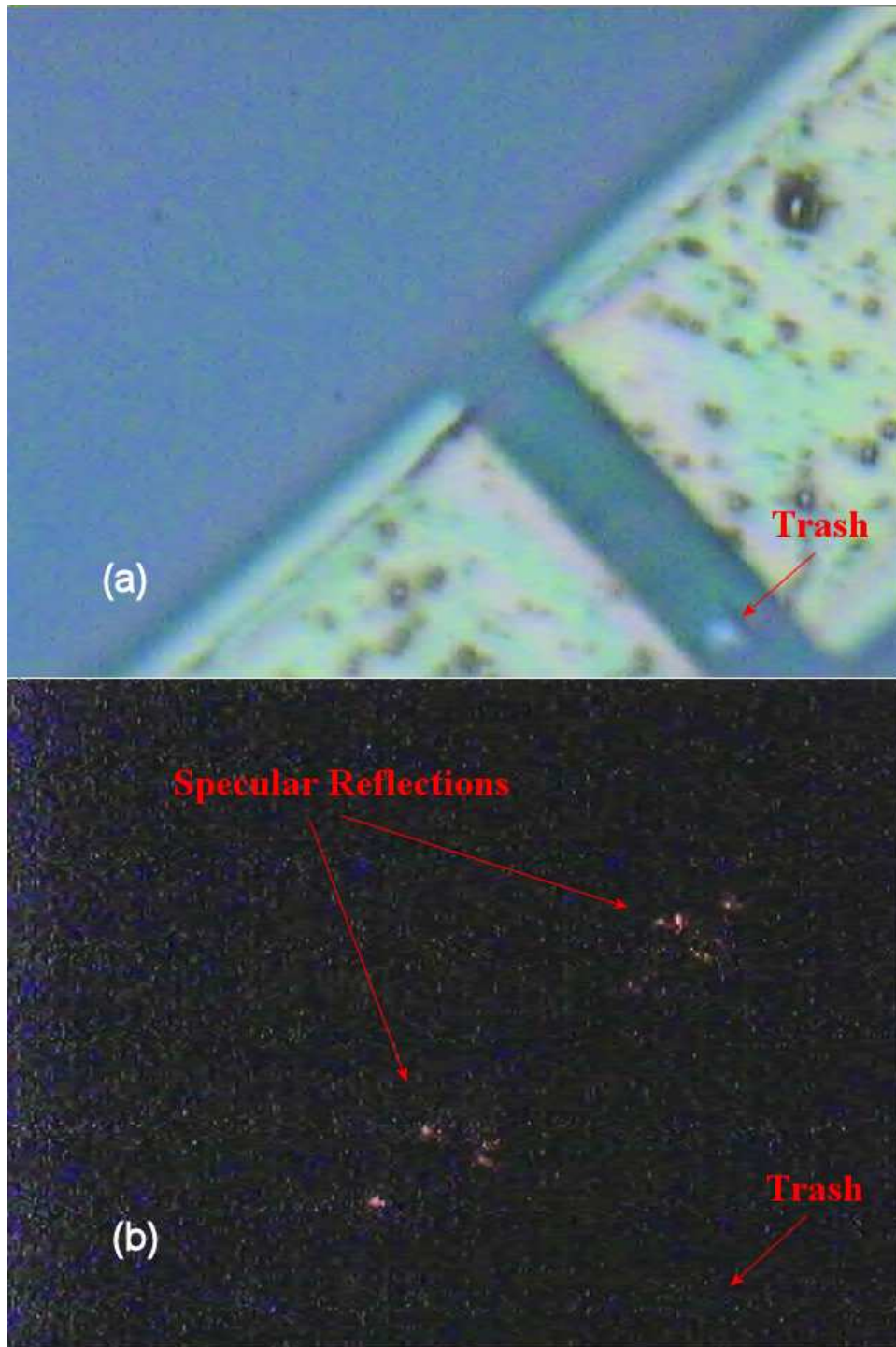
Figure 5.11: Gold channel and APC under 50X magnification with helium neon laser beam waveguided to the channel with (a) microscope light on bright and (b) microscope light off.
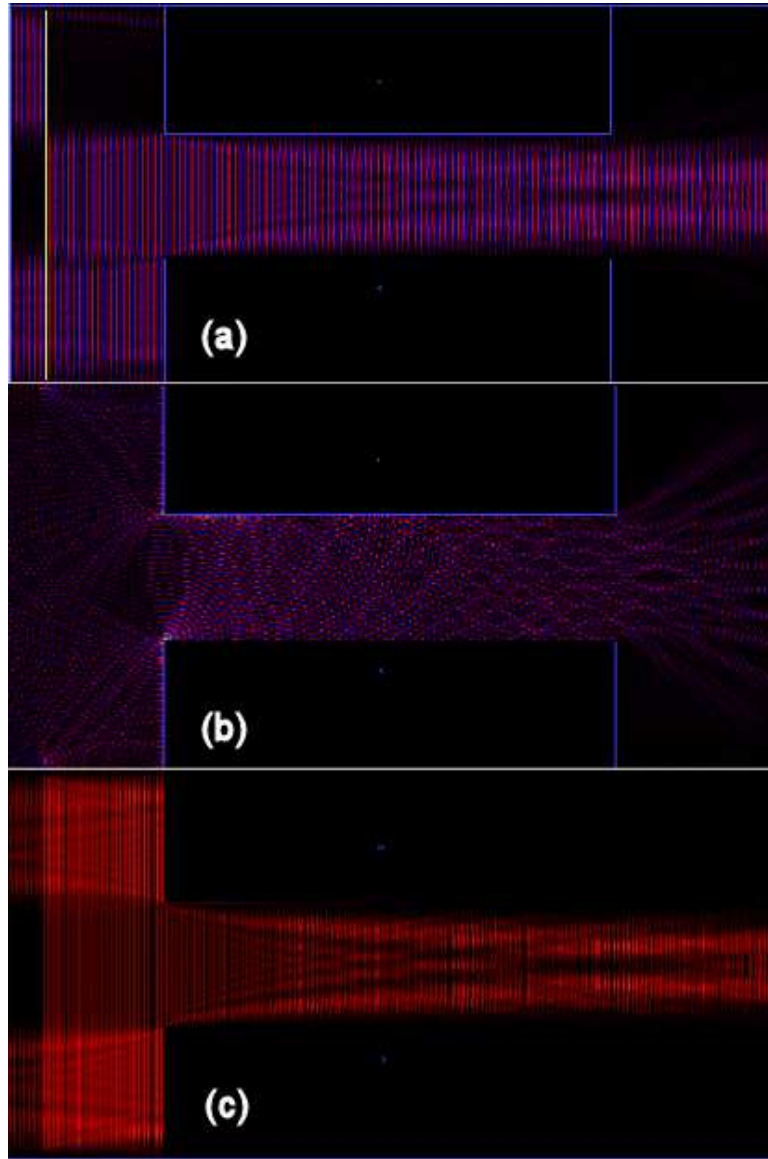
Figure 5.12: Crystalwave modeling results of the coupling of the slab waveguide to the gold channel where (a) is the E_x field (b) is the E_z field and (c) is the intensity at a 0° incidence on the gold channel.

105
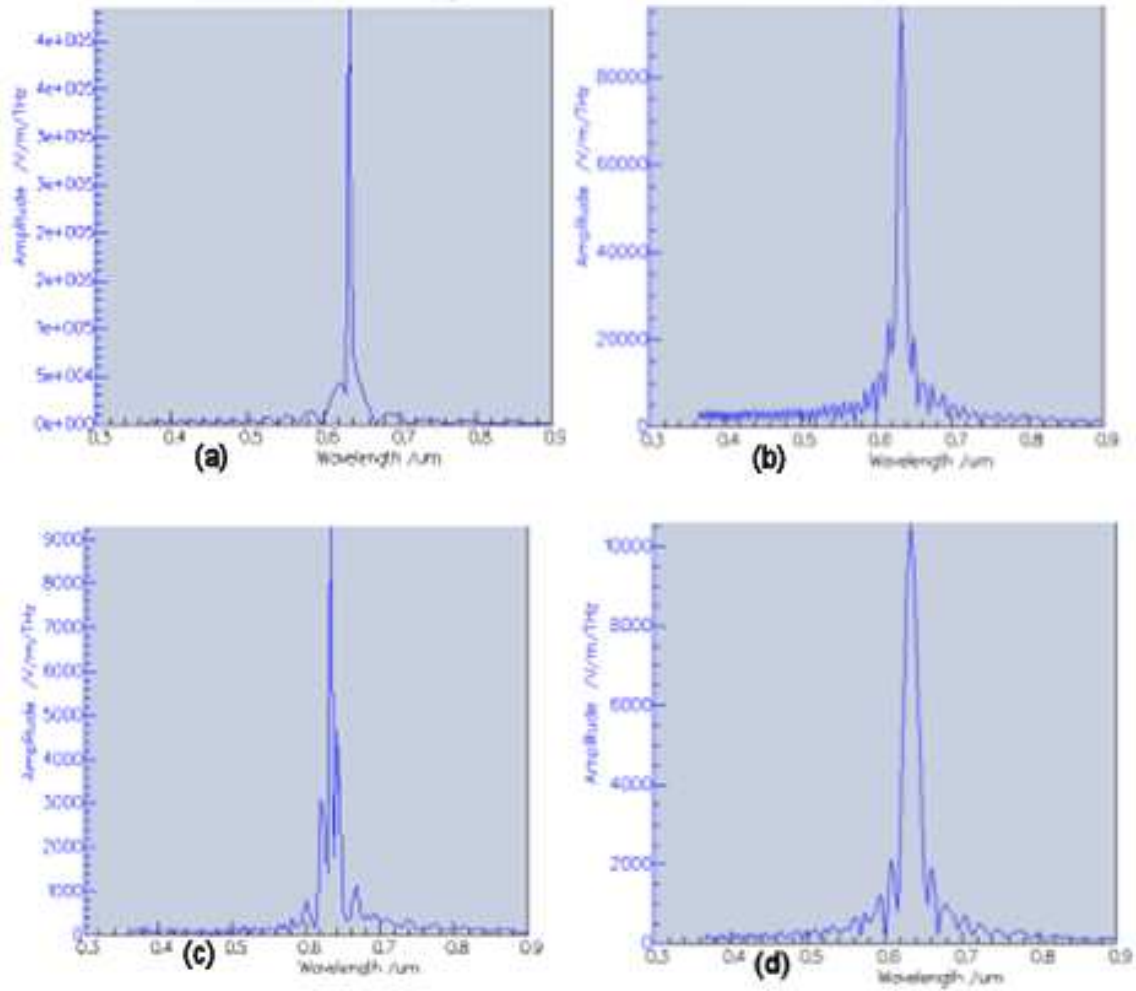
Figure 5.13:   The amplitudes of (a) the reference E_x field (b) the transmitted E_x field (c) the reference E_z field (d) the transmitted E_z field, all at 0° incidence on the gold channel.

106
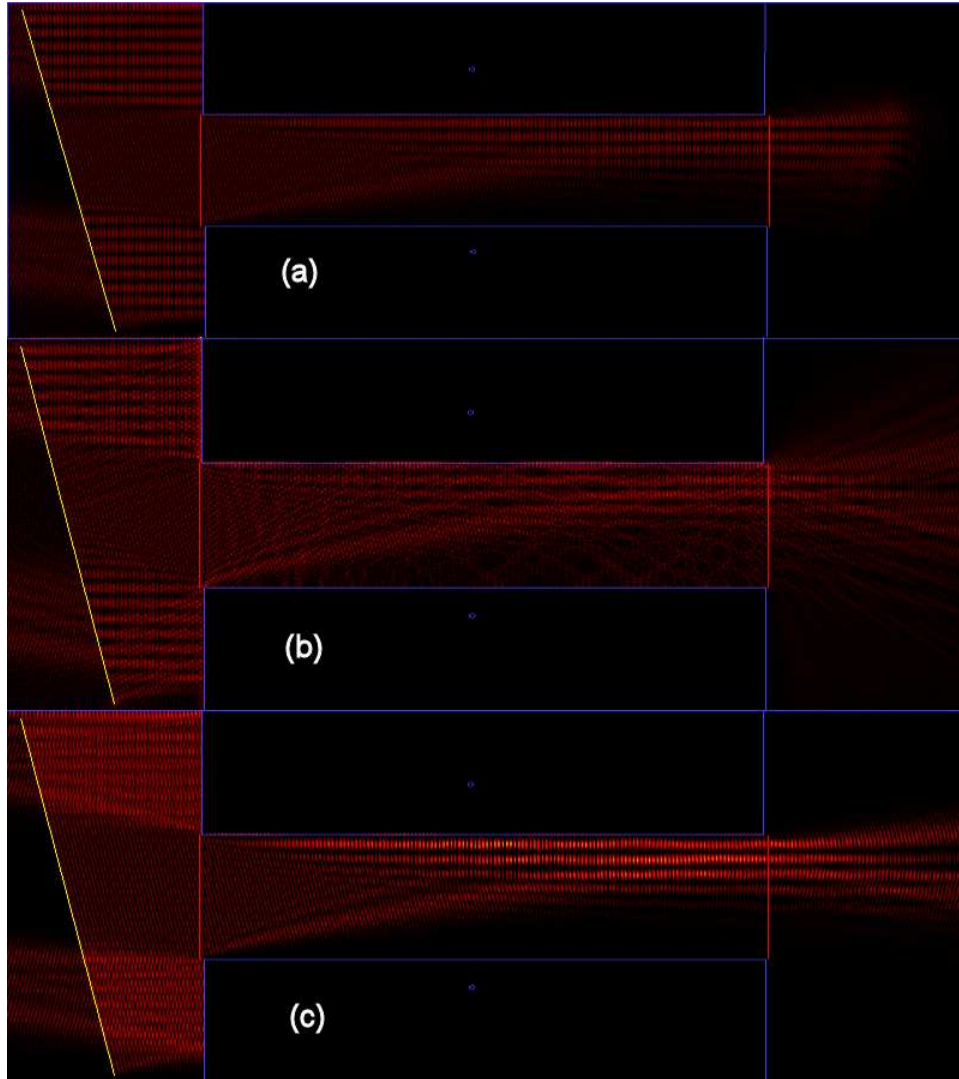
Figure 5.14: Crystalwave modeling results of the coupling of the slab waveguide to the gold channel where (a) is the E_x field (b) is the E_z field and (c) is the intensity at a 10° incidence on the gold channel.
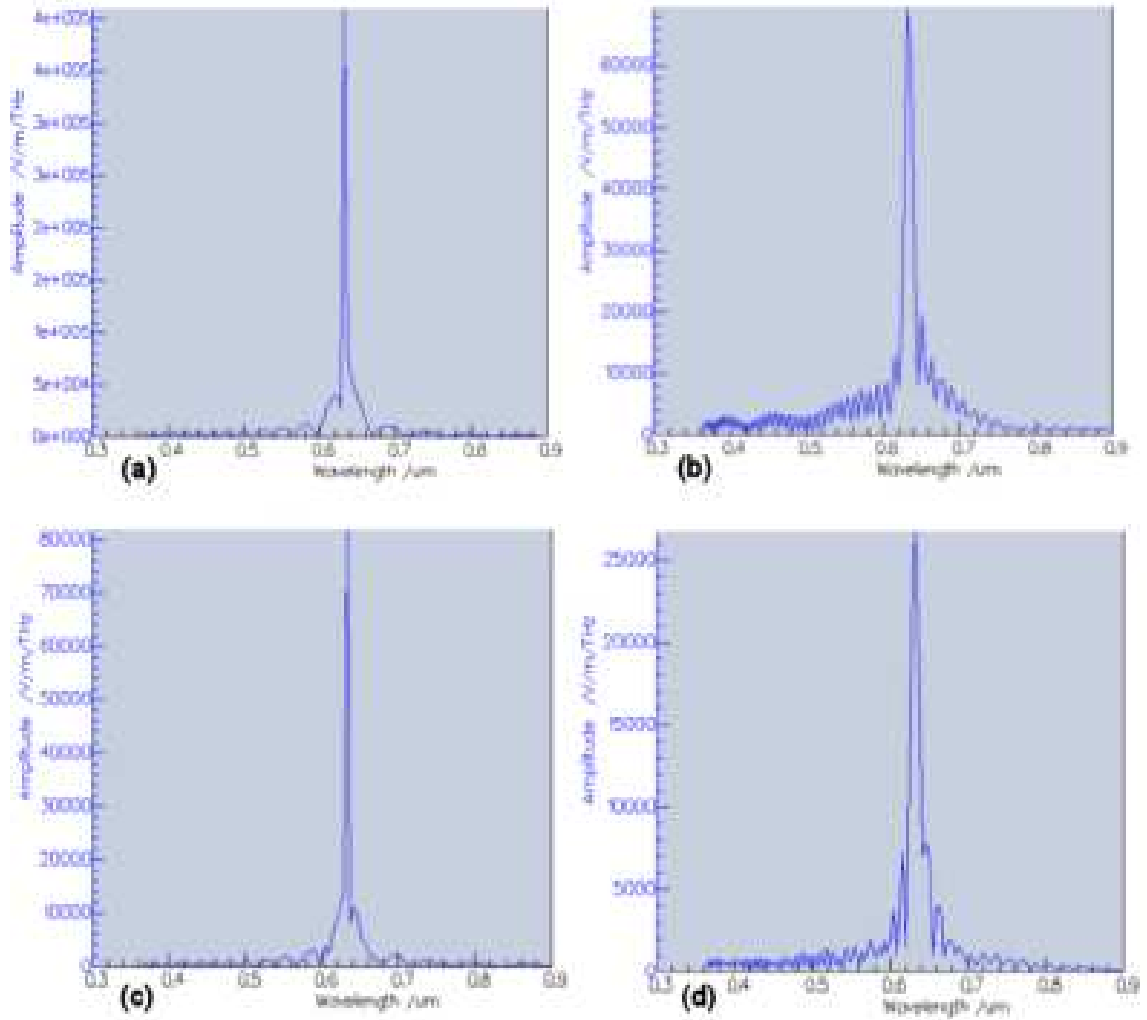
Figure 5.15: The amplitudes of (a) the reference E_x field (b) the transmitted E_x field (c) the reference E_z field, and (d) the transmitted E_z field, all at 10° incidence on the gold channel.

108
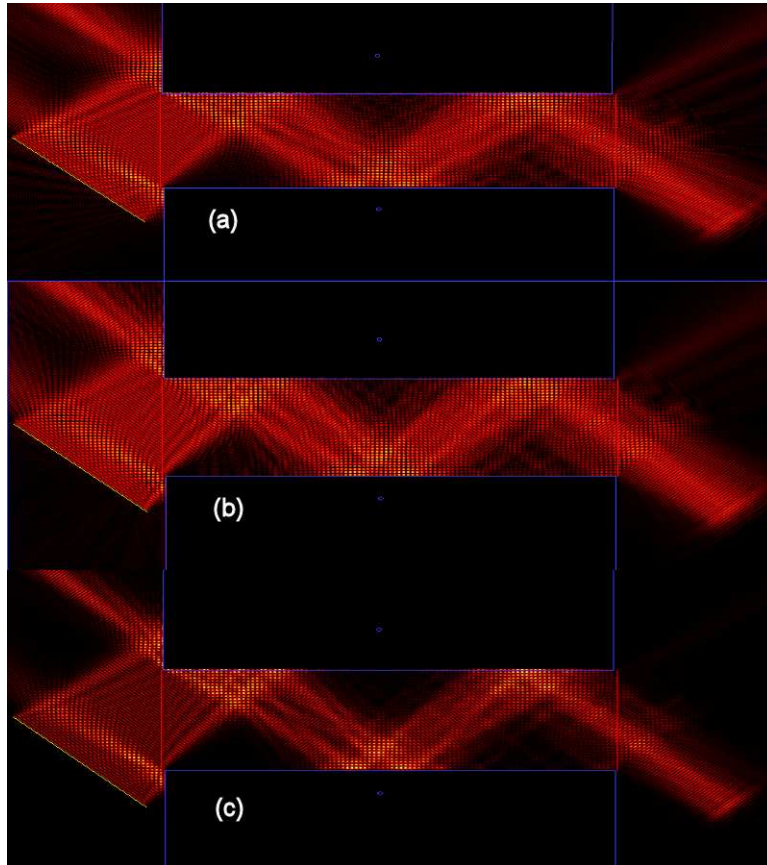
Figure 5.16: Crystalwave modeling results of the coupling of the slab waveguide to the gold channel where (a) is the E_x field (b) is the E_z field and (c) is the intensity, all at a 45° incidence on the gold channel.

as shown in (a), and the amplitude of the beam as it exits the channel, as shown in (b). Likewise, Figure 5.17 (c) and (d) show the amplitude of the E_z wave at 45° incidence as it enters and exits the channel, respectively. Figures 5.12 Through 5.17 show that the slab waveguided mode should clearly couple into the channel; however, it is also evident that the magnitude of these coupled waves is dramatically decreased and might possibly require a better detector to observe the scattering effects in the gold channel that was tested. The modeling depicts the beam to be propagating down the channel even at various angles to the opening. Figure 5.18 is a three-dimensional image of the intensity of the beam propagating down the gold channel. The source was modeled as a continuous Gaussian wave at 632.8 nm.

109
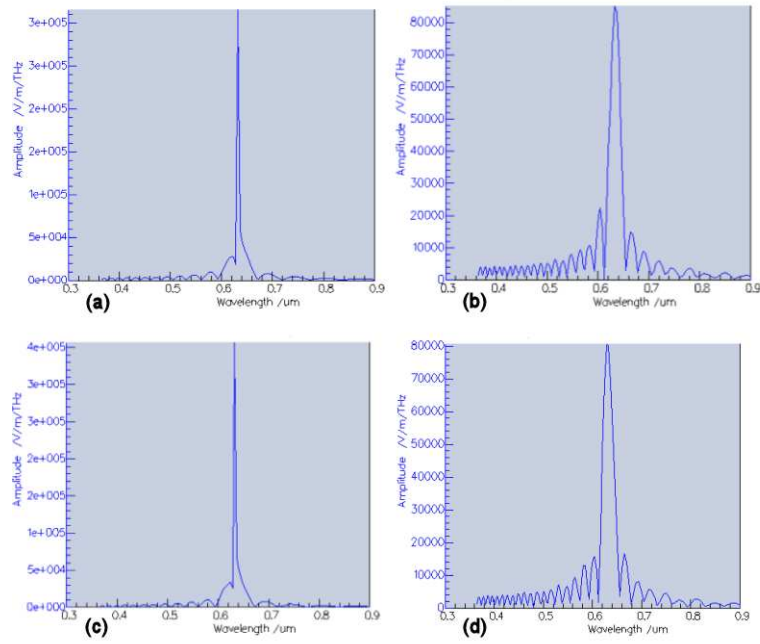
Figure 5.17: The amplitudes of (a) the reference E_x field (b) the transmitted E_x field (c) the reference E_z field, and (d) the transmitted E_z field, all at 45° incidence on the gold channel.
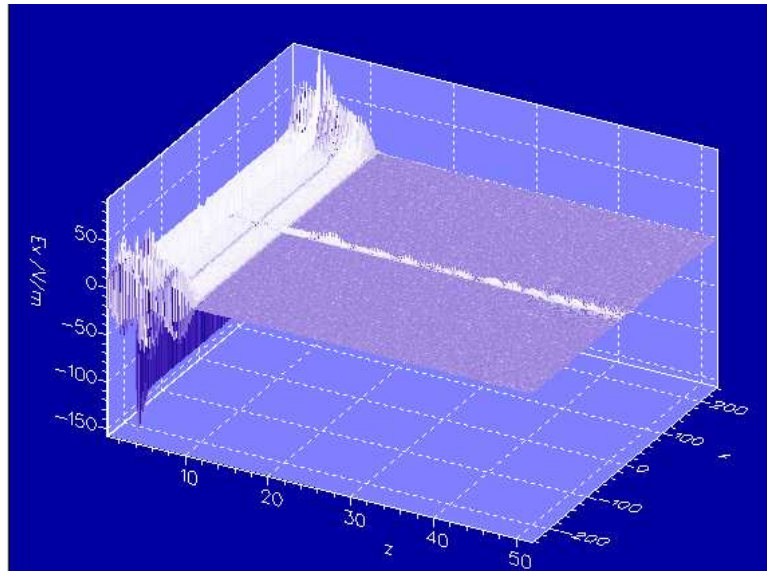
Figure 5.18: A three-dimensional look at the intensity of the wave propagating down the gold channel.

110
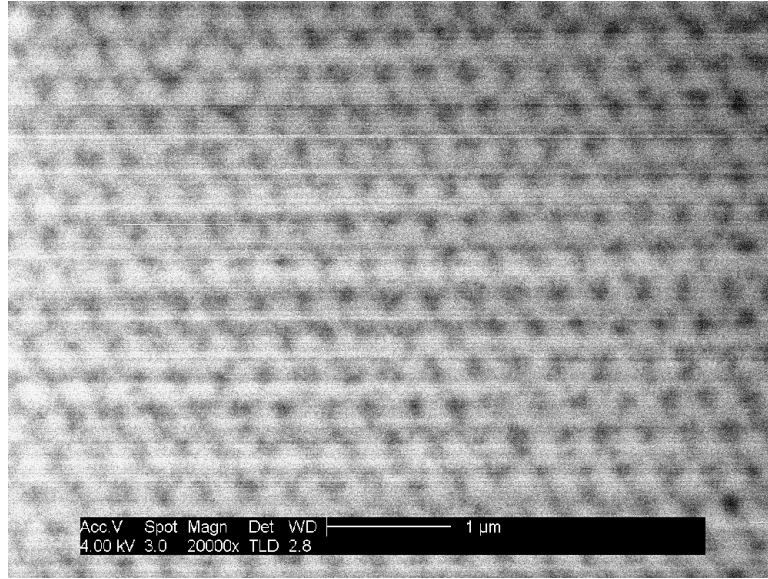
Figure 5.19: SEM image of the liquid crystal/polymer sample showing the periodicity and structure of the holographic setup.

5.2 Two-Dimensional Holographic Lithography Fabrication and Testing Results

The holographic technique, as outlined in the previous chapter, is a two-step process involving a liquid crystal/polymer substrate for initial setup justification, then SU-8 photo-resist for final structure realization. The liquid crystal/polymer material is suspended between two plates of microscopie slides with glass cylinders of 15-μm diameters mixed in to provide the proper thickness. The sample was exposed to the UV laser beam for 30 seconds. The top glass is peeled off and the structure left on the other slide is then imaged. The structure was coated with carbon to help prevent charging; Figure 5.19 shows an SEM of the structure obtained from the holographic setup. As was previously mentioned in Chapter IV under the "Holographic Lithography Technique of Two-Dimensional Photonic Crystals" section, the air columns obtained are not of the size to achieve a PhC with the desired PBG. However, this structure is used to determine the center-to-center periodicity and geometric structure of the holographic setup. Figure 5.19 shows that the periodicity is around 320 nm in a triangular pattern.

111
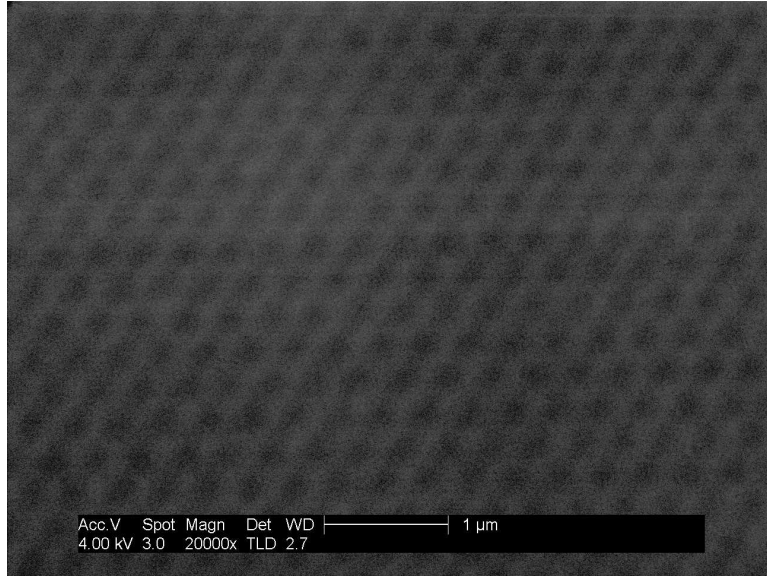
Figure 5.20: SEM image of the SU-8 photo-resist structure created by a 9.19-second exposure with the holographic setup.

For SU-8 photo-resist samples, the required spin-on procedures to achieve the 15-μm thickness are listed in Appendix F, as are the procedures for development and the exposure time chart. The actual thickness of the photo-resist was verified using an interferometer technique. The average thickness was determined to be 10 μm. This will change the waveguided modes and prism coupling angles desired to waveguide into this material. The programs in Appendix A will be run again with this new thickness to determine the exact angles required. The exposure chart for SU-8, displayed in Appendix F, is based on SU-8 deposited on silicon; silicon is too reflective at the UV wavelength used to write this structure and destroys the interference pattern; therefore, a glass substrate is used. Since glass is transparent at these wavelengths, the exposure times from the chart must be multiplied by a minimum factor of 2 as a basis, based on the advice of the company that makes the SU-8. The exposure times were increased from 5 seconds to 10 seconds in steps of 0.25 seconds. It was found that 9.19 seconds gave the best structure of air holes to material, as can be seen in Figure 5.20.

In order to use the SU-8 as a waveguiding medium and guide to the PhC created

112

by the exposure of the SU-8, two masks will be created and two different exposure periods will be necessary. The first mask masked off the entire area except where the three beams overlapped, creating a circle where the PhC exists. The second mask is an inverse of the first in order to expose the rest of the photo-resist to a regular beam (no pattern) so that it would not develop away during the developing period. Thus, all that is developed away are the air columns of the PhC. The SEM picture with an exposure time of 9.19 seconds is shown in Figure 5.21 (a). The ruggedness of the features in this image may be indicative of an imperfect beam quality. The periodicity and triangular structure that were desired are evident from Figure 5.21 (a); however, the columns of air do not penetrate the entire thickness of the photo-resist. This might be attributed to the process used to scrape the sample off the glass substrate and place it on the slide for the SEM. During this process, due to the small size of the crystal features, the entire underside of the crystal could be caved in on itself. A different exposure time may be required; however, Figure 5.21 (b) shows an exposure of 9.49 seconds, in which it is obvious that the structure is now being exposed away. The thickness of the sidewalls indicate that a shorter exposure time is required.

5.3 Testing Results of the Three-Dimensional Holographic Lithography Technique

The three-dimensional samples provided by Hybrid Technologies were characterized by performing FTIR measurement set up for directional hemispheric reflection measurement. The instrument used was a Bomen DA3 FTIR [5]. The sample was set at a 20° angle off of the incident beam to minimize any loss reflected back down the path of the beam. The results of the test are shown in Figure 5.22. It is shown that there is a 37 percent reflection around 3.1 μm. This is not a band gap; however, if it were a band gap, there would be 100 percent reflection instead of only 37 percent. This can be accounted for due to the imperfect fcc structure that Hybrid Technologies created. Since Snell's law was not truly accounted with their setup, the fcc structure is slightly ascued. The other contributer to this less-than-perfect reflection coefficient

113
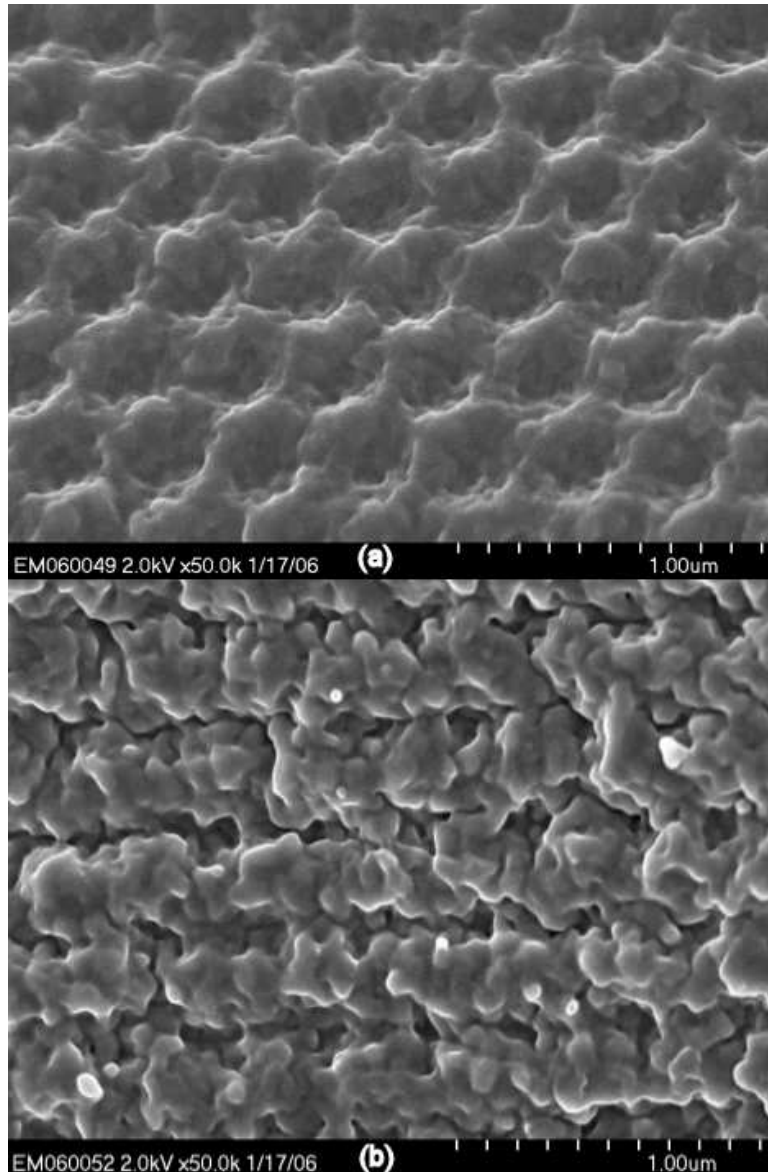
Figure 5.21: SEM of two-dimensional PhC in SU-8 fabricated by holographic lithography technique with an exposure time of (a) 9.19 seconds and (b) 9.49 seconds.

114
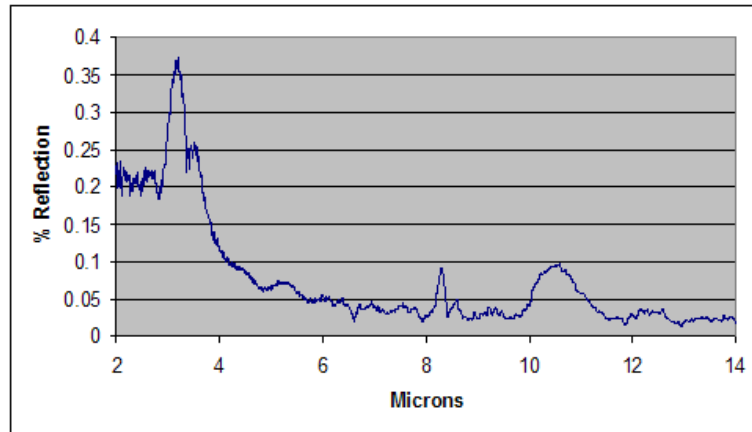
Figure 5.22: FTIR directional hemispheric reflection results of the three-dimensional sample from Hybrid Technologies.

could be due to the number of periods of the PhC. After approximately ten periods, there is enough attenuation of the wave to produce a PBG, less than that and it may not have enough periods to produce a PBG.

5.4 Conclusion

The results of the FIB fabrication for PhC's with a PBG on the order of visible wavelength was shown to not have the fidelity necessary to handle the charging effects in any suitable material for propagating a visible beam. However, it was shown that the FIB had the technical accuracy to create a PhC on that scale in materials in which charging was not a problem. The two-dimensional holographic technique was shown to be able to produce a structure of the correct dimensions necessary to produce a PBG in the visible as shown by the modeling in the previous chapter. However, the two-dimensional PhC that was created with the holographic technique lacked columns of air that extended all the way through the material. This can be attributed to the method that was used to transfer the sample from the glass slide to the post used in the SEM. The three-dimensional sample provided by Hybrid Technologies has some reflection properties indicating that it contains some properties of a PhC with a PBG; however, it does not contain a PBG or there would be total reflection for the PBG

115

region. In the next chapter, the results of this thesis will be summarized, providing the most important and relevant lessons learned. Future work and recommendations will also be discussed to continue this research and further the knowledge in this field.

VI. Conclusions and Recommendations

This chapter summarizes the results obtained in the previous chapters and outlines follow-on work in this field. The goal was to explore certain fabrication techniques for their viability to produce two-dimensional triangular PhC's with PBG's in the visible range and to further the knowledge base in this field regarding PhC's with PBG's in the visible range. As detailed in this thesis, the two-dimensional fabrication processes pursued were FIB, electron lithography, and holographic photopolymerization/lithography techniques. The fabrication techniques and materials used to create the PhC in part determined the characterization technique required to investigate the PBG. Characterization techniques examined included: the coupling of a beam by means of a prism into a wave-guiding medium in which the PhC has been fabricated and Fourier transform infrared spectrometer. The edge firing technique was considered for the electron beam lithography process. The FIB and holographic lithography techniques required a prism guiding technique to evaluate the PhC fabricated, however, as shown, the FIB lacked the fidelity to create PhC's in the required material needed to accommodate this characterization. The holographic lithography fabrication process proved to be capable to create a PhC in the proper material, however, time constraints prevented further characterization of this PhC.

The design of the PhC was based on a program created to display gap maps for triangular structures and then the PBG of the structure, designed from the gap maps, was modeled using another program created to display band diagrams for triangular structures, which was compared to the commercial FDTD softwares evaluated in this thesis. FDTD softwares, Crystalwave and OptiFDTD, were used to compare the modeling and simulation to the design. Finally, a three-dimensional PhC was tested with the FTIR technique, however, a complete PBG was not discovered for this sample either. There was some merit to the results obtained.

6.1 Fabrication using the Focused Ion Beam

The fabrication of the 10-μm channel in the gold strip was successful; however, the waveguide testing conducted showed no transmission of the coupled wave into the channel. This is contrary to the modeled results and is believed to be a detectivity problem of the camera being used. The data from the modeling showed a drop of about 77 percent for the E_x field at a 0° incident angle and a 82 percent decrease for a 10° angle of incidence. The PhC's that were attempted in the required material for prism waveguiding were unable to be fabricated due to drift problems caused by charging of the material. This charging effect was too great even at a low FIB power setting of 300 pA. It was shown that, technically, the FIB process can create PhC's of the dimensions required for a PBG in the visible range; however, a material that is not transmittable to the visible wavelength range was required. Overall, the FIB process is incapable of producing a PhC of this size in a material in which a visible wave can be guided, due to charging effects that lead to drift problems.

6.2 Electron Beam Lithography Fabrication

Although, at this time, a PhC of this design has not been fabricated, the modeling data shows that the design will be PhC with a 37 percent PBG. The modeling demonstrated around a 95 percent attenuation for the incident angle of 45° for the E_x field of the incident wave. The slight amount of wave that was transmitted could actually be an anomaly of the modeling software. The defined boundaries allowed for reflection bounces; this could account for the slight amplitude shown at the transmitted boundary of the PhC.

6.3 Holographic Two-Dimensional Fabrication

This technique is a viable process to produce a PhC with feature sizes capable to produce a PBG in the visible wavelength range. It was shown that a two-dimensional triangular structure of the correct periodicity and column radii was fabricated in a negative photo-resist material (SU-8). The columns may have been collapsed due to

118

the developing process, where by, a razor blade was used to lift-off the PhC while still emerged in isopropyl alcohol. The image of the final result shows the proper periodicity and approximately the correct volume fraction with an exposure time of 9.19 seconds. The actual spin-on techniques for a 15-μm thickness were shown to produce approximately a 10-μm layer. The exposure times had to be increased from the charts in Appendix F due to the substrate that the chart was based on. The silicon substrate is what the photo-resist depicts for its exposure times, which for the UV wavelength used to create the PhC, is very reflective; this would negate the interference pattern desired for the holographic technique. Thus, glass was used as the substrate. Glass will transmit the UV beam, and thus, some power will be lost that the chart assumed would not be lost. This accounts for the increased exposure times required to create this design on a glass substrate. The PhC design which was created in the photo-resist has been shown by the modeling software to produce an 8.5 percent PBG for the TE wave, with an 82 percent attenuation of the E_x field at a 0° incident angle.

6.4   Testing of the Three-Dimensional PhC

The testing conducted using the FTIR shows that there is some reflection properties of this crystal sample. The results show approximately a 37 percent reflection at the wavelength of 3.1 μm. The holographic lithography fabrication technique can produce a three-dimensional PhC as shown, however, the sample tested was not a true fcc structure, which is obvious due to Hybrid Technologies fabrication process; thus, there is no true PBG. Due to the feature size of this PhC structure, the existence of a PBG, if one existed, would be in the near infrared, which is in line with the reflection properties shown in the test result. While there is merit to the three-dimensional PhC designed by Hybrid Technologies, more work in this area is required to be able to produce a true three-dimensional PBG with this process. Eventually, the desire will be to use this process to create a three-dimensional PhC with a PBG in the visible wavelength range.

119

6.5 Evaluation of the FDTD Modeling Software

Both softwares evaluated were more than adequate for the PhC design of this thesis, excluding the three-dimensional PhC design; however, great care should be taken before purchasing a particular software. Both gave similar results for the designs attempted; however, the presentation, user-friendliness and analysis features were very different. Crystalwave was very user-friendly, presented colorful presentations, and presented some unique special feature applications (*i.e.*, thin oxidation walls around the PhC columns, randomization feature to simulate real world fabrication process, optimizer to select the proper size and placement of columns based on the desired design goals, *etc.*). OptiFDTD seems to be more flexible on the input of the structures, yet not as user friendly, and the special features are not as abundant at this time. Both companies claim to be constantly upgrading and improving their software capabilities. Support for both softwares throughout the trial period was excellent.

6.6 Future Recommendations

For follow-on work, finishing up the characterization of the holographic and electron beam techniques should be accomplished. The holographic lithography process needs to be set up as a dedicated table with quality equipment that is kept clean. The laser needs to have the best beam quality possible. Once these parameters are obtained, using the setup outlined in this thesis along with the power settings and the 9.19-second exposure time, a new sample should be fabricated. In order to prevent damaging the sample in developing, instead of lifting-off the sample to place it on the slide for the SEM, the sample should be left on the glass substrate and the glass substrate should be cut down to the proper size to place the glass with the PhC on the SEM slide. After verification of the PhC, the next sample should be fabricated using the same circular mask as before, however, this time after exposing the PhC area, the PhC area should be masked off and the rest of the photo-resist exposed to regular UV intensity light. This will allow only the columns of air to be developed away during the developing process and then the PhC can be tested by use of the

120

prism coupling described in this thesis.

In regards to the electron beam lithography process, the samples of $Al_{0.6}Ga_{0.4}As$ that have been sent to the University of Illinois should have a channel waveguide of 5-15-μm width etched into it and then have the PhC as designed in this thesis etched into the waveguide. The sample should then be oxidized and selectively etched to produce the structure suspended in air as described in this thesis. Edge firing techniques should be used to determine the PBG of the PhC designed.

A software package like the ones evaluated in this thesis should be purchased and then can be used to compare the test results of the previously mentioned testing to validate the software. Once this is accomplished, great work can be accomplished using the software to create other PhC designs to guide light, stop light, block light, determine new PhC designs that utilize new fabrication techniques and ultimately discover a new process for producing large quantities of PhC's. Along these lines, the software could be used to further the work started in designing a VSCEL structure that couples longitudinally. The idea is that the highly efficient VSCEL laser can be coupled in a wave guide channel with other VSCEL beams of sightly different wavelengths. Also, designing PhC's to have a broad PBG would be of significant importance to future work.

Appendix A. Prism Coupling/Wave-Guiding Calculation Program

This is the Mathematica® program that calculates the number of modes allowed to propagate in a given medium depending on its thickness and the indices of the core and cladding layers. This program then determines the roots and applies them to the prism coupling calculations required and detailed in appendix B, to determine the incident angle necessary to accomplish total internal reflections (TIR) in the prism allowing wave coupling into the core of the waveguide.

A.1   Program for Prism Coupling

This program is courtesy of Emily Heckman. The inputs are 'nc' the index of the core, 'nf' the index of one of the claddings, 'ns' the index of the other cladding, 'h' the thickness of the core. After the first part of the program is executed, then execute the second part (finding the root), note: the value which is assigned to look for the root must be close to the crossing point of interest based on the graph above it. The result of root is input into the square root of the next part. The equation following that result has the prism index as an input (the denominator of the Arcsin, and the result of the previous set of equations is placed in the numerator. The answer that results is the θ_m of the prism wave-guiding computations.

$nc = 1.457;$

$nf = 1.71;$

$ns = 1;$

$k = \frac{2\pi}{0.6328};$

$\beta[kappa_-] := \sqrt{k^2 nf^2 - kappa^2};$

$gammac[kappa_-] := \sqrt{\beta[kappa]^2 - k^2 nc^2};$

$gammas[kappa_-] := \sqrt{\beta[kappa]^2 - k^2 ns^2};$

$h = 2.0;$

$y1[kappa_-] := Tan[h\ kappa];$

122

$$y2[kappa\_] := \frac{(gammac[kappa] + gammas[kappa])}{(kappa(\frac{1 - gammac[kappa]gammas[kappa]}{kappa^2}))};$$

$$Plot[\{y1[kappa], y2[kappa]\}, \{kappa, 0, 20\}, PlotRange \to \{-10, 10\}]$$

Run the program to get the plot. Then execute the rest of the program.

$$FindRoot[y1[kappa] == y2[kappa], \{kappa, 1\}]$$

Execute this command to get desired result of:

$$\{kappa \to 1.43835\}$$

Now plug this number into equation below.

$$NSolve[\sqrt{k^2 nf^2 - 1.43835^2}]$$

Run this segment to get the following answer.

$$NSolve[16.9179]$$

Put this value into the equation below along with the prism index of 1.77 in this case.

$$NSolve[ArcSin[\frac{16.9179}{k\,1.77}]\frac{180}{\pi}]$$

Execute the above command and the answer is the θ_m shown below.

$$NSolve[74.2871]$$

123

Appendix B. Prism Coupling Theory

T his appendix explains the theory behind prism coupling.

B.1   Theory

Prism coupling is accomplished in order to couple a wave into a waveguiding medium in the transverse direction; this is usually accomplished when the ability to couple into the waveguide *via.* edge fire or butt coupling is not applicable. In order for the proper coupling to occur, the phase velocities of the waves in the prism and the waveguiding medium must have the same velocities in the z-direction [10]. This phase matching requirement means that:

$$\beta_m = kn_1 \sin(\theta_m) = 2\pi/\lambda_0 n_1 \sin(\theta_m) \tag{B.1}$$

The propagation constant β_m (z-component of the waveguided mode in the waveguide medium) must satisfy the expression $\beta_m > kn_1$ for waveguided modes. Where $k = 2\pi/\lambda$, n_1 is the index of the cladding that the coupling is occurring through and θ_m is the angle between the normal to the waveguide modes propagation and the input wave. Figure B.1 shows a depiction of this situation with no prism involved.

Combining the above two equations; shows that $\sin(\theta_m) > 1$, which is a mathematical impossibility. This is the reason a prism must be used to accomplish the coupling procedure. The prism must have an index that is higher than that of the adjacent layer to the prism (usually the cladding just above the waveguide layer) and the waveguiding layer as well. If a beam is directed into the prism hypotonus as shown in Figure B.2 [10], with an input angle such that the angle between the incident beam on the inner surface of the prism adjacent to the cladding layer achieves total internal reflection (TIR), a standing wave is set up in the prism. This mode is moving in the z-direction with a constant phase of β_p. Assuming the waveguide region has

124
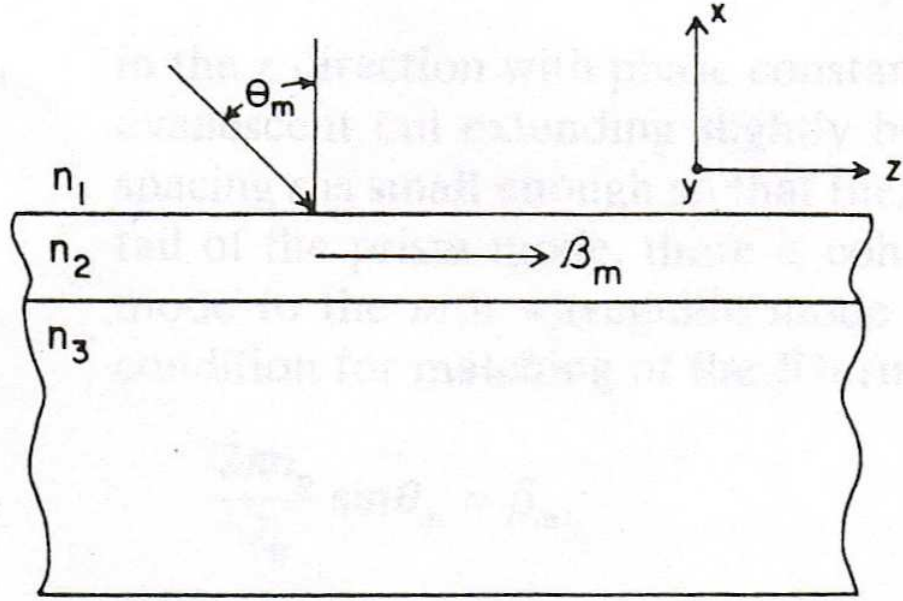
Figure B.1:   Diagram of coupling without a prism.

several modes that can exist, then there are several β_m (constant phase terms in the z-direction) that can exist.

The key is to get one of these modes to match up with the mode in the prism β_p. Both of these possible modes (β_m, β_p) have tails that extend beyond the region of the standing wave. The standing wave in the prism has a tail that extends into the n_1 layer and the wave mode in the waveguide has a tail that extends into the n_1 layer also (reference Figure B.2). When these tails overlap in a constructive manner, an exchange of energy takes place and the mode is successfully coupled. The equation that explains the matching of these terms ($\beta_m = \beta_p$) is shown below.

$$2\pi n_p/\lambda_0 \sin(\theta_m) = \beta_m \qquad \text{(B.2)}$$
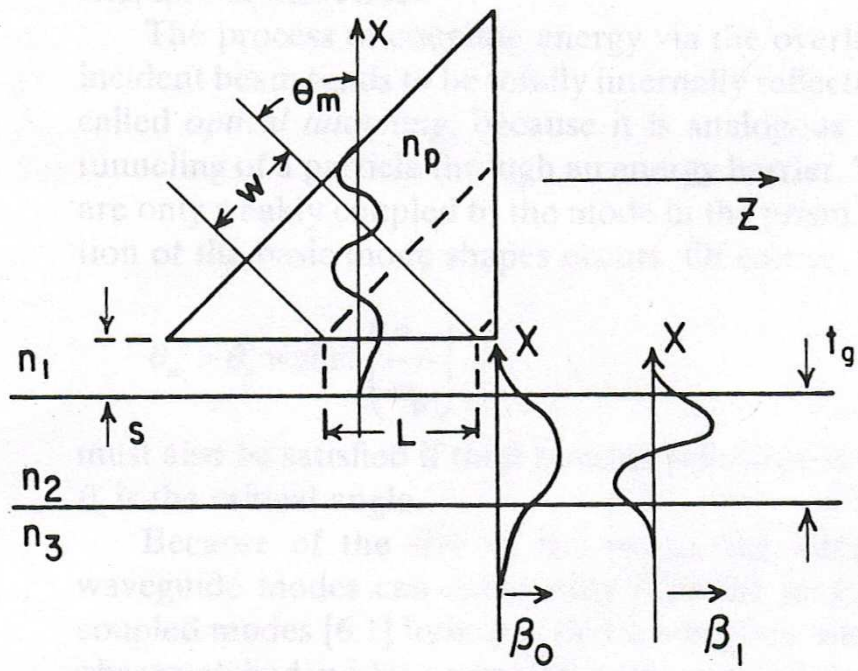
Figure B.2:   Diagram of coupling with a prism.

Realize of course that the equation:

$$\theta_m > \theta_c = \arcsin(n_1/n_p) \tag{B.3}$$

must also be satisfied for TIR to occur, where θ_c is the critical angle [10]. The interaction between the prism standing wave mode and the waveguide mode only occurs over length L (see Figure B.2). For a complete interchange of energy between the tails of these modes, the interaction of these modes in the z-direction must satisfy $kL = \pi/2$, k is the coupling coefficient. This coefficient depends on the indices of the prism, cladding and core and the prism spacing between the prism and the cladding. Therefore the required length for coupling is based on:

$$L = W/\cos(\theta_m) = \pi/2k \tag{B.4}$$

This can be solved for k by applying a known L, giving:

$$k = \pi \cos(\theta_m)/2W \tag{B.5}$$

In general the better the beam, *i.e.* the more uniform the electric field is across the the width W, resulting in a better coupled wave. Also to get almost 100 percent of the beam coupled, the trailing edge of the beam must exactly intersect the right-angle corner of the prism. If it is not perfectly in the corner, then some will be lost to reflection or transmission.

The equation that shows that the prism must be of an higher index than that of the cladding and the waveguide medium is shown below:

$$\beta_m \cong kn_2 = 2\pi/\lambda_0 n_2 \tag{B.6}$$

It can be seen that $n_p > n_2$ since the $\sin(\theta_m) \leq 1$.

127

Appendix C. Band Diagram and Gap map Programs

This appendix displays the band diagram program in Matlab® created by Dr. Haus and the gap map program in Matlab® created by Jeff Clark.

C.1 *Band Diagram Created by Dr. Haus*

The following Matlab® programs are the E and H field band diagrams for triangular structured two-dimensional PhC's. The inputs are the periodicity 'd' in μm and the radius 'a' in μm, along with the dielectric of the column material 'EPSA' and the dielectric of the material 'EPSB'. Another parameter that can be adjusted is the number of plane waves used to evaluate the design 'N1'.

Listing C.1: E field band diagram program. (appendix3/twoDEprog2gapmapver3.m)

```
  % These programs are for air columns in a dielectric
  % program for calculating the E-polarized band structure of the ...
      triangular
  % lattice.    A parameter determining the number of plane
  % waves
5 clear; clc; clf;
  N1 = 9;  % number of plane waves (i.e. 9) INPUT
  pi = acos(-1.0);
  %the lattice constant is scaled to unity.  The raduis of the ...
      column.
  d=.320; % I think this is the spacing of columns (microns) INPUT
10 a=.134;  % I think this is the radius of the columns (microns) ...
      INPUT
  % Volume fraction of column in the unit cell.
  bbeta = 3.14159*a*a/d/d*2.0/sqrt(3.0);
  EPSA=1; % column DIELECTRIC  INPUT
  MatNam1 = 'air'; %name of material
15 EPSB=2.957;% material DIELECTRIC  INPUT
  MatNam2 = 'SU-8'; %name of material
  % The major symmetry points in the Brillouin zone are defined (for
  % triangular geometry)

20
  gxg = 0.0; gyg = 0.0;
  gxx = 0.0; gyx = 2.0*pi/sqrt(3.0);
  gxj = 2.0*pi/3.0; gyj = 2.0*pi/sqrt(3.0);
  % The itinerary around the brillouin zone is laid out.
25 gxi(1) = gxx;
  gyi(1) = gyx;
  gxi(2) = gxg;
```

128

```matlab
  gyi(2) = gyg;
  gxi(3) = gxj;
30 gyi(3) = gyj;
  gxi(4) = gxx;
  gyi(4) = gyx;


35
   %   Construct the wave vectors used in the plane wave calculation

           L=0;
        gx1 = 2.0*pi;
40      gy1 = -2.0*pi/sqrt(3.0);
        gx2 = 0.0;
        gy2 = 2.0*pi*2.0/sqrt(3.0);
   %       generate all the wavevectors within a hexagon of
   %       diameter 2*n1.
45
  for ii=-N1:N1;
     for j=-N1:N1;
        if ( (-(N1+1)<(ii+j)) & ((ii+j)<(N1+1))),
           L=L+1;
50         gx(L) = gx1*ii + gx2*j;
           gy(L) = gy1*ii + gy2*j;
        end;
     end;
  end;
55

  % Construct the dielectric matrix
  % the volume of the unit cell is defined

60      vcel = sqrt(3.0)/2.0*d*d;
     for ii =1:L;
        EPS(ii,ii)= bbeta/EPSA+(1.0-bbeta)/EPSB;



65

           i1= ii + 1;
           for j=i1:L;
              x1 = gx(ii) - gx(j);
70            x2 = gy(ii) - gy(j);
              x = sqrt(x1*x1+x2*x2)*a/d;
              EPS(ii,j)=2.0*pi*(1/EPSA-1/EPSB)*a*a/(vcel)*besselj(1,...
                 x)/x;
              %  construct the inverse-dielectric matrix
              %
75 % The matrix is symmetric
              EPS(j,ii) = EPS(ii,j);
           end;
        end
```

129

```matlab
80

    % Use the itinerary constructed above to move around the ...
        Brillouin zone
        n=L;
85  % Counter for the number of points in the itinerary
        nknt = 1;
    for nk = 1:3;
            nk1 = nk+1
          nmax= 20;
90      for l=1:nmax;
            dkx =(l-1)*(gxi(nk1)-gxi(nk))/(nmax) + gxi(nk);
            dky =(l-1)*(gyi(nk1)-gyi(nk))/(nmax) + gyi(nk);
          for ii=1:n;
            a(ii,ii)=EPS(ii,ii)*((dkx+gx(ii))^2+(dky+gy(ii))^2)/4.0/...
                pi/pi;
95           for j=ii+1:n;
                a(ii,j)= EPS(ii,j)*((dkx+gx(ii))*(dkx+gx(j))+(dky+gy...
                    (ii))*...
                    (dky+gy(j)))/4.0/pi/pi;
                a(j,ii)=a(ii,j);
             end
100      end
        %

    % Find the eignevalues
            v=eig(a);
105         %
    % Store the lowest 10 eigenvalues for plotting
            for li=1:10;
             rr(nknt,li)=sqrt(v(li));
             kxx(nknt)=nknt-1;
110         end

        nknt = nknt + 1;
      end

115 end



120 % Plot lowest six eigenvalues

    figure(1)
    hold on;
    plot(kxx,rr(:,1),'r');
125 plot(kxx,rr(:,2),'b');
    plot(kxx,rr(:,3),'g');
    plot(kxx,rr(:,4),'y');
```

130

```
    plot(kxx,rr(:,5),'r');
    plot(kxx,rr(:,6),'b');
130 plot(kxx,rr(:,7),'g');
    plot(kxx,rr(:,8),'y');
    plot(kxx,rr(:,9),'r');
    plot(kxx,rr(:,10),'b');
    hold off;
135 xlabel('r/a','fontweight','bold','fontsize',16)
    ylabel('\omegaa/2\pic','fontweight','bold','fontsize',16)
    % title({'Gap Map for triangular structure';'columns of \epsilon...
        =',int2str(EPSA),...
    %     ' and material \epsilon=',int2str(EPSB);'E polarization red ...
        and blue, H polarization green and black'},'fontweight','bold...
        ','fontsize',16)

140 title({['Band Diagram of E Field Polarization for triangular ...
        structure'] ;['columns of \epsilon=',num2str(EPSA),' ', MatNam1...
        ,' and material \epsilon=',num2str(EPSB),' ', MatNam2]})
```

Listing C.2: H field band diagram program. (appendix3/twoDHprog2gapmapver3.m)

```
    % program for calculating the H-polarized band structure of the ...
        triangular
    % lattice.  Lines are inserted to convert it to band structure ...
        computation
    % for the E-polarized waves.  A parameter determining the number ...
        of plane
    % waves
 5 clear; clc; clf;
    N1 = 9;  % number of plane waves (i.e. 9) INPUT
    pi = acos(-1.0);
    %the lattice constant is scaled to unity.  The raduis of the ...
        column.
    d=.320; % I think this is the spacing of columns  INPUT
10 a=0.134;  % I think this is the radius of the columns  INPUT
    % Volume fraction of column in the unit cell.
    bbeta = 3.14159*a*a/d/d*2.0/sqrt(3.0);
    EPSA=1; % column DIELECTRIC  INPUT
    MatNam1 = 'Air'; %name of material
15 EPSB=2.957;% material DIELECTRIC  INPUT
    MatNam2 = 'SU-8'; %name of material
    % The major symmetry points in the Brillouin zone are defined (for
    % triangular geometry)

20
    gxg = 0.0; gyg = 0.0;
    gxx = 0.0; gyx = 2.0*pi/sqrt(3.0);
    gxj = 2.0*pi/3.0; gyj = 2.0*pi/sqrt(3.0);
    % The itinerary around the brillouin zone is laid out.
25 gxi(1) = gxx;
```

131

```
   gyi(1) = gyx;
   gxi(2) = gxg;
   gyi(2) = gyg;
   gxi(3) = gxj;
30 gyi(3) = gyj;
   gxi(4) = gxx;
   gyi(4) = gyx;



35
   %   Construct the wave vectors used in the plane wave calculation

         L=0;
       gx1 = 2.0*pi;
40       gy1 = -2.0*pi/sqrt(3.0);
       gx2 = 0.0;
       gy2 = 2.0*pi*2.0/sqrt(3.0);
   %     generate all the wavevectors within a hexagon of
   %     diameter 2*n1.
45
   for ii=-N1:N1;
     for j=-N1:N1;
         if ( (-(N1+1)<(ii+j)) & ((ii+j)<(N1+1))),
           L=L+1;
50         gx(L) = gx1*ii + gx2*j;
           gy(L) = gy1*ii + gy2*j;
         end;
       end;
   end;
55


   % Construct the dielectric matrix
   % the volume of the unit cell is defined

60       vcel = sqrt(3.0)/2.d0*d*d;
     for ii =1:L;
         EPS(ii,ii) = bbeta*EPSA + (1.0-bbeta)*EPSB;
         % H-method insert the following line to replace the ...
             preceding line.
         % Construct the inverse dielectric matrix
65       %  EPS(ii,ii)= bbeta/EPSA+(1.0-bbeta)/EPSB;



           i1= ii + 1;
70         for j=i1:L;
             x1 = gx(ii) - gx(j);
             x2 = gy(ii) - gy(j);
             x = sqrt(x1*x1+x2*x2)*a/d;
             EPS(ii,j) = 2.0*pi*(EPSA-EPSB)*a*a/(vcel) * besselj(1,...
               x)/x;
```

132

```matlab
75                    % H-method insert the following line to replace the ...
                        preceding
                      % line , construct the inverse - dielectric matrix
                      %   EPS(ii,j)=2.d0*pi*(1/EPSA-EPSB)*a*a/(vcel)*besselj...
                        (1,x)/x;
    % The matrix is symmetric
                      EPS(j,ii) = EPS(ii,j);
80          end;
        end




85
    % Use the itinerary constructed above to move around the ...
        Brillouin zone
        n=L;
    % Counter for the number of points in the itinerary
        nknt = 1;
90  for nk = 1:3;
            nk1 = nk+1
          nmax= 20;
        for l=1:nmax;
            dkx =(l-1)*(gxi(nk1)-gxi(nk))/(nmax) + gxi(nk);
95          dky =(l-1)*(gyi(nk1)-gyi(nk))/(nmax) + gyi(nk);
          for ii=1:n;
            a(ii,ii) = ((dkx+gx(ii))^2 + (dky+gy(ii))^2)/4.0/pi/pi;
            b(ii,ii) = EPS(ii,ii);
            for j=ii+1:n;
100             a(ii,j) = 0.0;
                a(j,ii) = 0.0;
                b(ii,j) = EPS(ii,j);
                b(j,ii) = EPS(ii,j);
            end
105     end
        % H-method insert the following lines and replace the ...
            preceding 10
        % lines
        %  for ii=1:n;
        %    a(ii,ii)=EPS(ii,ii)*((dkx+gx(ii))^2+(dky+gy(ii))^2)/4.0/...
            pi/pi;
110     %       for j=ii+1:n;
        %        a(ii,j)= EPS(ii,j)*((dkx+gx(ii))*(dkx+gx(j))+(dky+gy(...
            ii))*...
        %       (dky+gy(j)))/4.0/pi/pi;
        %       a(j,ii)=a(ii,j);
        %        end
115     %       end

    % Find the eignevalues
            v=eig(a,b);
            % Find the eignevalues for the H-method replace the ...
                preceding line
```

133

```
120         %   v=eig(a);
    % Store the lowest 10 eigenvalues for plotting
            for li=1:10;
              rr(nknt,li)=sqrt(v(li));
              kxx(nknt)=nknt-1;
125         end

          nknt = nknt + 1;
      end

130 end



135 % Plot lowest six eigenvalues

    figure(1)
    hold on;
    plot(kxx,rr(:,1),'r');
140 plot(kxx,rr(:,2),'b');
    plot(kxx,rr(:,3),'g');
    plot(kxx,rr(:,4),'y');
    plot(kxx,rr(:,5),'r');
    plot(kxx,rr(:,6),'b');
145 plot(kxx,rr(:,7),'g');
    plot(kxx,rr(:,8),'y');
    plot(kxx,rr(:,9),'r');
    plot(kxx,rr(:,10),'b');

150 xlabel('r/a','fontweight','bold','fontsize',16)
    ylabel('\omegaa/2\pic','fontweight','bold','fontsize',16)
    % title({'Gap Map for triangular structure';'columns of \epsilon...
        =',int2str(EPSA),...
    %      ' and material \epsilon=',int2str(EPSB);'E polarization red ...
        and blue, H polarization green and black'},'fontweight','bold...
        ','fontsize',16)

155 title({['Band Diagram of H Field polarization for triangular ...
        structure'] ;['columns of \epsilon=',num2str(EPSA),' ', MatNam1...
        ,' and material \epsilon=',num2str(EPSB),' ', MatNam2]})
```

C.2 Gap Map Program Created by Jeff Clark

The following program was designed to allow gap maps of two-dimensional tri-angular structured PhC's to be created based off of the previous two programs by Dr. Haus (being used as subroutines). Input parameters are 'N1' number of plane waves used to evaluate the desired structures, 'EPSA' the dielectric of columns, 'EPSB' the

134

dielectric of the material, 'NDC' number of dispersion curves calculated, 'Prec' the precision of the PBG desired, 'a range' the radius range for the calculations of the gap map, 'a range increments' the value that the 'a range' is incremented from one end of the range to the other.

Listing C.3:   E field band diagram program. $(\mathrm{appendix3/main}_r outine_v er5.m)$

```matlab
%main routine
pack
clear;clc;clf;

5 %Inputs

d=1;%lattice spacing
%a=.48; %radius
N1=9;  % number of plane waves
10 EPSA=1; %epselon of columns
MatNam1 = 'Air'; %name of material
EPSB=11.94;  % epselon of material
MatNam2 = 'AlGaAs'; %name of material
NDC=10;  %number of dispersion curves
15 Prec = 2; % precision of the PBG
a_range = [.34 .38];  % range of radius of columns
a_range_increments = .01; % increment range radius of columns

%end inputs
20
% determine radius to send in subroutine
count = 0;
for t = a_range(1):a_range_increments:a_range(2)
    a = t;
25    count = count +1;

    %call sub routine for E and H field
    rr = Efielddispersion(N1,d,a,EPSA,EPSB,NDC);% this is actually...
        the H field subroutine
    ss = Hfielddispersion(N1,d,a,EPSA,EPSB,NDC);%  this is ...
        actually the E field subroutine
30
    % precision of band gap
    factor = 10^Prec;
    gg = rr.*factor;  % this is so we can round the dispersion ...
        curve
    gg = round(gg);   % numbers to the percsion requested
35    rr = gg./factor;

    factor = 10^Prec;
    gg2 = ss.*factor;  % this is so we can round the dispersion ...
        curve
    gg2 = round(gg2);   % numbers to the percsion requested
40    ss = gg2./factor;
```

135

```matlab
        % calculations for PBG
        for z = 1:NDC-1
            bandH = max(rr(:,z));  % finds the max number along this ...
                dispersion curve
            bandL = min(rr(:,z+1)); % finds the min number along the ...
                disperision curve
            if bandL-bandH > 0   % this determins if there is a gap or...
                 not
                PBGLow(count,z)= bandH;  % now we store the results
                PBGHigh(count,z)=bandL;
            else
                PBGLow(count,z)=0;
                PBGHigh(count,z)=0;

            end
            z = z+1;
        end
        % now for the H field
        for z = 1:NDC-1
            HbandH = max(ss(:,z));  % finds the max number along this ...
                dispersion curve
            HbandL = min(ss(:,z+1)); % finds the min number along the ...
                disperision curve
            if HbandL-HbandH > 0   % this determins if there is a gap ...
                or not
                HPBGLow(count,z)= HbandH;  % now we store the results
                HPBGHigh(count,z)=HbandL;
            else
                HPBGLow(count,z)= 0;  % now we store the results
                HPBGHigh(count,z)=0;
            end
            z = z+1;
        end

    x(count) = (round((a/d).*factor))./factor;  % this records the...
        r/a factor for the x axis
    end


  % this gets rid of the zeros and records only integer numbers for...
      the most
% part
u = 1;
u1 = 1;
for c = 1:count
    u = 1;
    u1 = 1;
    for v = 1:size(PBGLow')
        if PBGLow(c,v) > 0
            y(c,u) = PBGLow(c,v);
            u = u + 1;
```

```matlab
                end
            if PBGHigh(c,v) > 0
                y2(c,u1) = PBGHigh(c,v);
                u1 = u1 + 1;
            end
        end
    end

    %This is the same as above but for the H field
    u = 1;
    u1 = 1;
    for c = 1:count
        u = 1;
        u1 = 1;
        for v = 1:size(HPBGLow')
            if HPBGLow(c,v) > 0
                Hy(c,u) = HPBGLow(c,v);
                u = u + 1;
            end
            if HPBGHigh(c,v) > 0
                Hy2(c,u1) = HPBGHigh(c,v);
                u1 = u1 + 1;
            end
        end
    end

    %determine what to plot

    [i,j] = find(PBGLow); % finds the indicies of the nonzero integers
    j(max(size(j))+1)= 0; % add a 0 to end of string to use as stop ...
        bit in next code
    i(max(size(i))+1)= 0;% add a 0 to end of string to use as stop bit...
        in next code
    counter = 1;

    % now same as above for the H field

    [Hi,Hj] = find(HPBGLow); % finds the indicies of the nonzero ...
        integers
    Hj(max(size(Hj))+1)= 0; % add a 0 to end of string to use as stop ...
        bit in next code
    Hi(max(size(Hi))+1)= 0;% add a 0 to end of string to use as stop ...
        bit in next code
    Hcounter = 1;


    % plot
    %plots the dispersion curves on the gap map
    figure(2)
    while counter < max(size(j))-1  % make sure we don't violate the ...
        max length of the matrix
        newcounter = 1;
```

137

```matlab
        while isequal(j(counter),j(counter+1)) % finds all column ...
            numbers so they can be ploted with corresponding x values
             if counter < max(size(j))-1
                inew(newcounter) = i(counter);
                jnew(newcounter) = j(counter);
                counter = counter +1;
                newcounter = newcounter+1;
            end
        end
        inew(newcounter) = i(counter);
        jnew(newcounter) = j(counter);
        plot(x(inew(1:end)),PBGLow(inew(1:end),jnew(1:end)),'r')
        hold on
        plot(x(inew(1:end)),PBGHigh(inew(1:end),jnew(1:end)),'b')
        hold on
        clear inew
        clear jnew
        counter = counter +1;
    end
    % now print the H field gap map
Hold on

    while Hcounter < max(size(Hj))-1  % make sure we don't violate the...
        max length of the matrix
        Hnewcounter = 1;
        while isequal(Hj(Hcounter),Hj(Hcounter+1)) % finds all column ...
            numbers so they can be ploted with corresponding x values
             if Hcounter < max(size(Hj))-1
                Hinew(Hnewcounter) = Hi(Hcounter);
                Hjnew(Hnewcounter) = Hj(Hcounter);
                Hcounter = Hcounter +1;
                Hnewcounter = Hnewcounter+1;
            end
        end
        Hinew(Hnewcounter) = Hi(Hcounter);
        Hjnew(Hnewcounter) = Hj(Hcounter);
        plot(x(Hinew(1:end)),HPBGLow(Hinew(1:end),Hjnew(1:end)),'g')
        hold on
        plot(x(Hinew(1:end)),HPBGHigh(Hinew(1:end),Hjnew(1:end)),'k')
        hold on
        clear Hinew
        clear Hjnew
        Hcounter = Hcounter +1;
    end
    xlabel('r/a','fontweight','bold','fontsize',16)
    ylabel('\omegaa/2\pic','fontweight','bold','fontsize',16)
    title({['Gap Map for triangular structure'] ;['columns of \epsilon...
        =',num2str(EPSA),' ', MatNam1,' and material \epsilon=',num2str...
        (EPSB),' ', MatNam2];['H polarization red and blue, E ...
        polarization green and black']})
```

138

Listing C.4:   H field band diagram program. (appendix3/Efielddispersion.m)

```matlab
function rr = Efielddispersion(N1,d,a,EPSA,EPSB,NDC)
% program for calculating the E-polarized band structure of the ...
    triangular
% lattice.  Lines are inserted to convert it to band structure ...
    computation
% for the H-polarized waves.  A parameter determining the number ...
    of plane
% waves

%N1 = 9;  % number of plane waves (i.e. 9) INPUT
pi = acos(-1.0);
%the lattice constant is scaled to unity.  The raduis of the ...
    column.
%d=1; % I think this is the spacing of columns  INPUT
%a=0.48;  % I think this is the radius of the columns  INPUT
% Volume fraction of column in the unit cell.
bbeta = 3.14159*a*a/d/d*2.0/sqrt(3.0);
%EPSA=1.; % column DIELECTRIC  INPUT
%EPSB=13;% material DIELECTRIC  INPUT
% The major symmetry points in the Brillouin zone are defined (for
% triangular geometry)


gxg = 0.0; gyg = 0.0;
gxx = 0.0; gyx = 2.0*pi/sqrt(3.0);
gxj = 2.0*pi/3.0; gyj = 2.0*pi/sqrt(3.0);
% The itinerary around the brillouin zone is laid out.
gxi(1) = gxx;
gyi(1) = gyx;
gxi(2) = gxg;
gyi(2) = gyg;
gxi(3) = gxj;
gyi(3) = gyj;
gxi(4) = gxx;
gyi(4) = gyx;




%  Construct the wave vectors used in the plane wave calculation

        L=0;
      gx1 = 2.0*pi;
      gy1 = -2.0*pi/sqrt(3.0);
      gx2 = 0.0;
      gy2 = 2.0*pi*2.0/sqrt(3.0);
%      generate all the wavevectors within a hexagon of
%      diameter 2*n1.

for ii=-N1:N1;
    for j=-N1:N1;
        if ( (-(N1+1)<(ii+j)) & ((ii+j)<(N1+1))),
```

139

```matlab
                L=L+1;
                gx(L) = gx1*ii + gx2*j;
50              gy(L) = gy1*ii + gy2*j;
            end;
        end;
    end;


55
    % Construct the dielectric matrix
    % the volume of the unit cell is defined

        vcel = sqrt(3.0)/2.d0*d*d;
60  for ii =1:L;
        EPS(ii,ii) = bbeta*EPSA + (1.0-bbeta)*EPSB;
        % H-method insert the following line to replace the ...
            preceding line.
        % Construct the inverse dielectric matrix
        %  EPS(ii,ii)= bbeta/EPSA+(1.0-bbeta)/EPSB;
65


        i1= ii + 1;
        for j=i1:L;
70          x1 = gx(ii) - gx(j);
            x2 = gy(ii) - gy(j);
            x = sqrt(x1*x1+x2*x2)*a/d;
            EPS(ii,j) = 2.0*pi*(EPSA-EPSB)*a*a/(vcel) * besselj(1,...
                x)/x;
            % H-method insert the following line to replace the ...
                preceding
75          % line , construct the inverse-dielectric matrix
            %   EPS(ii,j)=2.d0*pi*(1/EPSA-EPSB)*a*a/(vcel)*besselj...
                (1,x)/x;
  % The matrix is symmetric
            EPS(j,ii) = EPS(ii,j);
        end;
80  end


85 % Use the itinerary constructed above to move around the ...
      Brillouin zone
      n=L;
  % Counter for the number of points in the itinerary
      nknt = 1;
  for nk = 1:3;
90      nk1 = nk+1;
        nmax= 20;
    for l=1:nmax;
        dkx =(l-1)*(gxi(nk1)-gxi(nk))/(nmax) + gxi(nk);
        dky =(l-1)*(gyi(nk1)-gyi(nk))/(nmax) + gyi(nk);
```

140

```
95          for ii=1:n;
                 a(ii,ii) = ((dkx+gx(ii))^2 + (dky+gy(ii))^2)/4.0/pi/pi;
                 b(ii,ii) = EPS(ii,ii);
                 for j=ii+1:n;
                      a(ii,j) = 0.0;
100                   a(j,ii) = 0.0;
                      b(ii,j) = EPS(ii,j);
                      b(j,ii) = EPS(ii,j);
                 end
            end
105     % H-method insert the following lines and replace the ...
             preceding 10
        % lines
        %   for ii=1:n;
        %     a(ii,ii)=EPS(ii,ii)*((dkx+gx(ii))^2+(dky+gy(ii))^2)/4.0/...
             pi/pi;
        %         for j=ii+1:n;
110     %         a(ii,j)= EPS(ii,j)*((dkx+gx(ii))*(dkx+gx(j))+(dky+gy(...
             ii))*...
        %         (dky+gy(j)))/4.0/pi/pi;
        %         a(j,ii)=a(ii,j);
        %         end
        %         end
115
   % Find the eignevalues
             v=eig(a,b);
             % Find the eignevalues for the H-method replace the ...
                preceding line
        %    v=eig(a);
120 % Store the lowest 10 eigenvalues for plotting
             for li=1:NDC;
              rr(nknt,li)=sqrt(v(li));
              kxx(nknt)=nknt-1;
             end
125
        nknt = nknt + 1;
      end

   end
130



   % Plot lowest six eigenvalues
135
   figure(1)
   hold on;
   plot(kxx,rr(:,1),'r');
   plot(kxx,rr(:,2),'b');
140 plot(kxx,rr(:,3),'g');
   plot(kxx,rr(:,4),'y');
   plot(kxx,rr(:,5),'r');
```

141

```
plot(kxx,rr(:,6),'r');
hold off;
```

Listing C.5:   H field band diagram program. (appendix3/Hfielddispersion.m)

```matlab
function ss = Hfielddispersion(N1,d,a,EPSA,EPSB,NDC)
% program for calculating the H-polarized band structure of the ...
    triangular
% lattice.    A parameter determining the number of plane
% waves
5
%N1 = 9;  % number of plane waves (i.e. 9) INPUT
pi = acos(-1.0);
%the lattice constant is scaled to unity.  The raduis of the ...
    column.
%d=1; % I think this is the spacing of columns  INPUT
10 %a=0.48;  % I think this is the radius of the columns   INPUT
% Volume fraction of column in the unit cell.
bbeta = 3.14159*a*a/d/d*2.0/sqrt(3.0);
%EPSA=1.; % column DIELECTRIC  INPUT
%EPSB=13;% material DIELECTRIC  INPUT
15 % The major symmetry points in the Brillouin zone are defined (for
% triangular geometry)


gxg = 0.0; gyg = 0.0;
20 gxx = 0.0; gyx = 2.0*pi/sqrt(3.0);
gxj = 2.0*pi/3.0; gyj = 2.0*pi/sqrt(3.0);
% The itinerary around the brillouin zone is laid out.
gxi(1) = gxx;
gyi(1) = gyx;
25 gxi(2) = gxg;
gyi(2) = gyg;
gxi(3) = gxj;
gyi(3) = gyj;
gxi(4) = gxx;
30 gyi(4) = gyx;



  % Construct the wave vectors used in the plane wave calculation
35
        L=0;
     gx1 = 2.0*pi;
     gy1 = -2.0*pi/sqrt(3.0);
     gx2 = 0.0;
40     gy2 = 2.0*pi*2.0/sqrt(3.0);
%     generate all the wavevectors within a hexagon of
%     diameter 2*n1.

for ii=-N1:N1;
45   for j=-N1:N1;
       if ( (-(N1+1)<(ii+j)) & ((ii+j)<(N1+1))),
```

142

```
                 L=L+1;
                 gx(L) = gx1*ii + gx2*j;
                 gy(L) = gy1*ii + gy2*j;
50         end;
      end;
   end;


55 % Construct the dielectric matrix
   % the volume of the unit cell is defined

         vcel = sqrt(3.0)/2.0*d*d;
      for ii =1:L;
60        EPS(ii,ii)= bbeta/EPSA+(1.0-bbeta)/EPSB;




65          i1= ii + 1;
            for j=i1:L;
                x1 = gx(ii) - gx(j);
                x2 = gy(ii) - gy(j);
                x = sqrt(x1*x1+x2*x2)*a/d;
70              EPS(ii,j)=2.0*pi*(1/EPSA-1/EPSB)*a*a/(vcel)*besselj(1,...
                   x)/x;
                %  construct the inverse-dielectric matrix
                %
  % The matrix is symmetric
                EPS(j,ii) = EPS(ii,j);
75          end;
      end



80
   % Use the itinerary constructed above to move around the ...
      Brillouin zone
       n=L;
   % Counter for the number of points in the itinerary
       nknt = 1;
85 for nk = 1:3;
          nk1 = nk+1;
        nmax= 20;
      for l=1:nmax;
          dkx =(l-1)*(gxi(nk1)-gxi(nk))/(nmax) + gxi(nk);
90        dky =(l-1)*(gyi(nk1)-gyi(nk))/(nmax) + gyi(nk);
        for ii=1:n;
            a(ii,ii)=EPS(ii,ii)*((dkx+gx(ii))^2+(dky+gy(ii))^2)/4.0/...
               pi/pi;
             for j=ii+1:n;
                 a(ii,j)= EPS(ii,j)*((dkx+gx(ii))*(dkx+gx(j))+(dky+gy...
                    (ii))*...
```

143

```matlab
95                      (dky+gy(j)))/4.0/pi/pi;
                    a(j,ii)=a(ii,j);
                end
            end
            %
100
    % Find the eignevalues
            v=eig(a);
            %
    % Store the lowest 10 eigenvalues for plotting
105         for li=1:NDC;
                ss(nknt,li)=sqrt(v(li));
                kxx(nknt)=nknt-1;
            end

110         nknt = nknt + 1;
        end

    end

115


    % Plot lowest six eigenvalues

120 figure(1)
    hold on;
    plot(kxx,ss(:,1),'r');
    plot(kxx,ss(:,2),'b');
    plot(kxx,ss(:,3),'g');
125 plot(kxx,ss(:,4),'y');
    plot(kxx,ss(:,5),'r');
    plot(kxx,ss(:,6),'r');
    hold off;
```

Appendix D. Index Program for AlGaAs

This appendix shows the Matlab® program to calculate the indices of AlGaAs courtesy of Lt.Col. Lott.

D.1   The Matlab® Index Program

The following code returns the real and imaginary (if there is any absorption at that wavelength and mole fraction) index of AlGaAs. This code was based off of the C-code created by Lt.Col. Lott and was converted to Matlab® by Capt. Ochoa. This code is a function and can easily be used from the Matlab® command line. The inputs are the mole fraction of Aluminum and the wavelength in angstroms.

Listing D.1:   AlGaAs index calculation program. (appendix4/AlGaAs2Indxr.m)

```matlab
function IndexOfRefraction = AlGaAs2Indxr(x, lambda)
% AlGaAs2Indxr Index of Refraction of AlGaAs between 1.5 to 2.2 eV
% IndexOfRefraction = AlGaAs2Indxr(x, lambda);
% x - mole fraction of Al
% lambda - Angstroms
%
% Calculates the real and complex index of refraction for AlxGa1-...
    xAs
% between 1.5 to 2.2 eV. Ref: Aspnes et al JAP 60(2) 15 July 1986
% 8265.3 Ang to 5635 Ang

% based on C-code by Lt Col James A. Lott
% note: does not call AlGaAs1Indxr for x>=.8... may need to modify...
    later...
% Converted to Matlab by: Lt Bernhard, Capt Ochoa 1/21/00

%initialize B

B = 0;

if x < 0
    x = 0;
end

if x > 1
    x = 1;
end

dumvar = x*10;
dumint = floor(dumvar);

% convert lambda to energy in eV
```

145

```matlab
    hbo = 1.2398/(lambda*10^-4);

    for n = 1:2
        if dumint == 0
            if lambda > 6440
                A = 5.4323-.00036682*lambda+1.8515E-8*lambda^2;
            else
                A = 12.117-.0025398*lambda+1.945E-7*lambda^2;
            end
            B = -.40018+.31110*hbo-.0023811*hbo^2;
        end

        if dumint == 1
            A = 7.1961-.00087025*lambda+5.279E-8*lambda^2;
            if hbo < 1.5
                B=0;
            else
                B=-.4627+.31595*hbo;
            end
        end

        if dumint == 2
            if lambda > 7300
                A = 8.954-.0012113*lambda+6.6093E-8*lambda^2;
            else
                A = 7.9718-.0011754*lambda+7.9735E-8*lambda^2;
            end
            if hbo < 1.65
                B = 0;
            else
                B=-.59874+.36371*hbo;
            end
        end

        if dumint == 3
            A = 6.2665-.00061784*lambda+3.3085E-8*lambda^2;
            if hbo < 1.71
                B = 0;
            else
                B=-.72324+.42533*hbo;
            end
        end

        if dumint == 4
            A = 6.3718-.0006667*lambda+3.6448E-8*lambda^2;
            if hbo < 1.82
                B = 0;
            else
                B=-.67961+.37484*hbo;
            end
        end
```

146

```matlab
    if dumint == 5
        A = 6.6566-.000777*lambda+4.45688E-8*lambda^2;
        if hbo < 1.99
            B = 0;
        else
            B=-1.3012+.655*hbo;
        end
    end

    if dumint == 6
        A = 6.82823-.0008582*lambda+5.138948E-8*lambda^2;
        if hbo < 2.1
            B = 0;
        else
            B=-1.213+.58*hbo;
        end
    end


    if dumint == 7
        A = 7.1055-.0009804*lambda+6.10584E-8*lambda^2;
        B = 0;
    end


    if dumint == 8
        A = 6.52743-.00086692*lambda+5.5396E-8*lambda^2;
        B = 0;
    end

    if dumint == 9
        A = 5.1113-0.00047623*lambda+2.7779E-08*lambda^2; %5635 to...
            8265
        B = 0;
    end


    if dumint == 10
        A = 4.7921-0.00041411*lambda+2.405E-08*lambda^2; %5635 to...
            8265
        B = 0;
    end

    if B < 0
        B = 0;
    end

    A1(n) = A;
    B1(n) = B;
```

147

```matlab
        dumint = dumint + 1;
    end

    rindex = A1(1) - (A1(1) - A1(2))*(10*x - floor(10*x));
    cindex = (B1(1) - (B1(1) - B1(2))*(10*x - floor(10*x)));

    IndexOfRefraction = rindex - i*cindex;
```

148

T his appendix explains the equations used in the program that predicts the holographic interference pattern used in the holographic polymerization/lithography process.

E.1 Geometry and Equations of the Interference Pattern of Two-Dimensional PhC setup

The following text is courtesy of Dr. Sutherland. The text explains the equations that were typed into MATHCAD® which is displayed after this text explanation.

The following sketch illustrates the geometry and equations that follow.
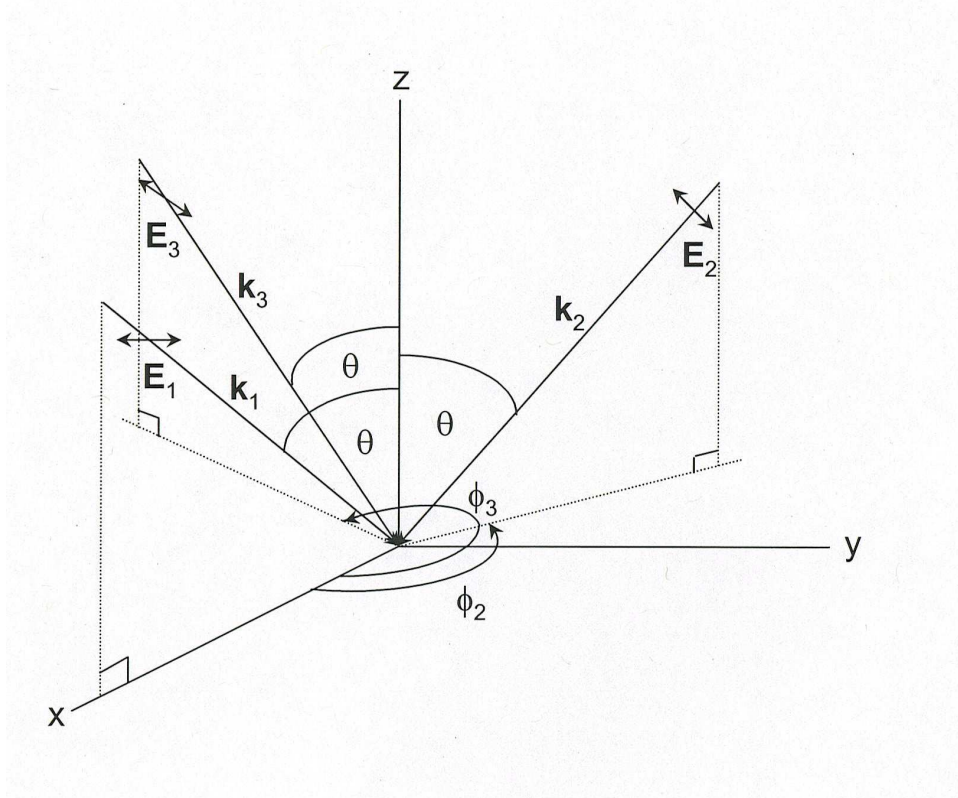
Figure E.1: The geometry that explains the equations used in the holographic polymerization/lithography process.

The sample is in the x-y plane, and the z-axis is perpendicular to the sample. The wave vectors of figure E.1 are given by:

149

$$k_1 = -k(\sin(\theta)\hat{x} + \cos(\theta)\hat{z})$$

$$k_2 = -k((\sin(\theta)\cos(\phi_2))\hat{x} + (\sin(\theta)\sin(\phi_2))\hat{y} + \cos(\theta)\hat{z})$$

$$k_3 = -k((\sin(\theta)\cos(\phi_3))\hat{x} + (\sin(\theta)\sin(\phi_3))\hat{y} + \cos(\theta)\hat{z})$$

Where k is the wave vector $(2\pi)/\lambda$ and λ is the wavelength of the laser that is writing the structure. The fields are given by:

$$E_1 = \hat{y}$$

$$E_2 = -\cos(\theta)\cos(\phi_2)\hat{x} - \cos(\theta)\sin(\phi_2)\hat{y} + \sin(\theta)\hat{z}$$

$$E_3 = \sqrt{2}(-(\sin(\alpha)\sin(\phi_3) + \cos(\alpha)\cos(\theta)\cos(\phi_3))\hat{x} + (\sin(\alpha)\cos(\phi_3)$$

$$- \cos(\alpha)\cos(\theta)\sin(\phi_3))\hat{y} + \cos(\alpha)\sin(\theta)\hat{z})$$

The angel α is the angle of polarization in the local plane of polarization of beam 3; in other words this is the the polarization of beam 1 that has an added angle α with respect to the plane of incidence in the z-plane. The intensity in the sample is given by:

$$I(r) = 4 + \sum_{m \neq n} S_{mn} \exp(iG_{mn}) \tag{E.3}$$

where $G_{mn} = k_m - k_n$ are the reciprocal lattice vectors, and $S_{mn} = E_m \cdot E_n$ are the structure factors and $m, n = 1...3$.

It is worth noting that the θ values govern the overall pattern, ϕ governs the overall periodicity and α governs the intensity of each pattern or the volume fraction.

E.2   Holographic Interference Equations in MATHCAD$^{\circledR}$

This program will calculate a two-dimensional interference pattern achieved when three laser beams intersect. It depends on the angle theta (incident angle) the rotation angle (phi) from a fixed reference plane x-z and the polarization of each

150

beam in accordance to each beam's plane of incidence (which is related to the angle phi also). These calculations are oriented with the sample that is being written on to be in the x-y plane. The angle alpha is the angle of polarization with respect to the plane of incidence of beam 3. Theta, alpha and phi must be in radians

$$\theta 1 := 50 \cdot \frac{\pi}{180}$$

$$\theta 2 := 50 \cdot \frac{\pi}{180}$$

$$\theta 3 := 50 \cdot \frac{\pi}{180}$$

$$\phi 2 := 120 \cdot \frac{\pi}{180}$$

$$\phi 3 := 240 \cdot \frac{\pi}{180}$$

$$\alpha := 10 \cdot \frac{\pi}{180}$$

$$\lambda := 0.3648$$

$$k := 2 \cdot \frac{\pi}{\lambda}$$

The wave vectors are as follows:

$$x := \begin{pmatrix} 1 \\ 0 \\ 0 \end{pmatrix}$$

$$y := \begin{pmatrix} 0 \\ 1 \\ 0 \end{pmatrix}$$

$$z := \begin{pmatrix} 0 \\ 0 \\ 1 \end{pmatrix}$$

$$k1 := -k \cdot (sin(\theta 1) \cdot x + cos(\theta 1) \cdot z)$$

$$k2 := -k \cdot [(sin(\theta 2) \cdot cos(\phi 2)) \cdot x + (sin(\theta 2) \cdot sin(\phi 2)) \cdot y + cos(\theta 2) \cdot z]$$

$$k3 := -k \cdot [(sin(\theta 3) \cdot cos(\phi 3)) \cdot x + (sin(\theta 3) \cdot sin(\phi 3)) \cdot y + cos(\theta 3) \cdot z]$$

The E-fields are given by the following equations:

151

$$E1 := y$$

$$E2 := -(cos(\theta2) \cdot cos(\phi2)) \cdot x - (cos(\theta2) \cdot sin(\phi2)) \cdot y + sin(\theta2) \cdot z$$

$$E3 := \sqrt{2} \cdot [-(sin(\alpha) \cdot sin(\phi3) + cos(\alpha) \cdot cos(\theta3) \cdot cos(\phi3)) \cdot x + (sin(\alpha) \cdot cos(\phi3) -$$

$$cos(\alpha) \cdot cos(\theta3) \cdot sin(\phi3)) \cdot y + (cos(\alpha) \cdot sin(\theta3)) \cdot z]$$

Now calculate the structure factors $(S_{mn} = E_m \cdot E_n)$.

$$S := \begin{pmatrix} E1 \cdot E2 \\ E1 \cdot E3 \\ E2 \cdot E1 \\ E2 \cdot E3 \\ E3 \cdot E1 \\ E3 \cdot E2 \end{pmatrix}$$

Now calculate the reciprocal lattice vectors $(G_{mn} = k_m - k_n)$.

$$G := \begin{pmatrix} k1 - k2 \\ k1 - k3 \\ k2 - k1 \\ k2 - k3 \\ k3 - k1 \\ k3 - k2 \end{pmatrix}$$

$$r(a, b, c) := \begin{pmatrix} a \\ b \\ c \end{pmatrix}$$

$$n := 0, 1..5$$

$$I(a, b, c) := 4 + \sum_n (S_n \cdot e^{i \cdot G_n \cdot r(a,b,c)})$$

$$N := 100$$

$$scale := 0.01$$

This gives a scale such that 30 is 0.3 microns

$$q := 1, 2..N$$

152

$$w := 1, 2..N$$

$$a_q := q \cdot scale$$

$$b_w := w \cdot scale$$

$$c_w := w \cdot scale$$

$$J0_{q,w} := I(a_q, b_w, 0)$$

Then insert a plot and use 'J0' as the argument to have plotted.

Appendix F. SU-8 Processing Steps

This appendix explains the process used to spin on and develop the SU-8 photo-resist.

F.1   Process for the Spin on and Development of SU-8 Photo-Resist.

The process used in this experiment to spin-on the SU-8 2010 negative photo-resist by MicroChem for a 15 μm thick layer is detailed below:

Spin-on

The glass substrate was cleaned with Acetone and Methonal and dried with Air/Nitrogen.

Then it was baked at 200° C for 5 minutes.

Then it was placed in a spinner that was set for the following parameters:

Ramp to 500 rpm at 100 rpm/sec.

Ramp to 3000 rpm at 300 rpm/sec and hold for 30 seconds.

Soft bake to evaporate the solvent and densify the film at 65° C for 1 minute, then at 95° C for 2 minutes.

Post-exposure process

After exposure, a post-exposure bake is necessary for the cross-linking to occur. Heat on hot plate at 65° C for 1 minute, then at 95° C for 2 minutes. It is important to note that since the SU-8 is on a glass substrate, the hot plate may need to be turned up higher to ensure the temperature of the SU-8 reaches 95° C. It must get above 95° C for the cross-linking to occur; however, it can not get hotter than 115° to 120° C. To facilitate this requirement, the samples were put on a 105° C hot plate for the 2 minute time period. This ensures the above restrictions are meet. Allow the samples to cool slowly. Put in SU-8 developer from MicroChem, for 3 minutes with slight agitation. The samples were then rinsed with isopropyl alcohol and allowed to dry. Once dry, hard bake at 180° C for 1 minute in order to ensure the hardness of the structure.

MICRO·CHEM

NANO™ SU-8 2000

Negative Tone Photoresist Formulations 2002-2025

- High aspect ratio imaging
  Near vertical side walls

- Near UV (350-400nm) processing

- Improved coating properties
  Uniformity (lower surface tension)
  Adhesion

- Faster drying
  Improved throughput

5μm, 10μm and 20μm post arrays in a 50μm thick film.

SU-8 2000 is a high contrast, epoxy based photoresist designed for micromachining and other microelectronic applications, where a thick, chemically and thermally stable image is desired. SU-8 2000 is an improved formulation of SU-8, which has been widely used by MEMS producers for many years. By using a faster drying, more polar solvent system, improved coating properties and higher throughput are realized. Film thicknesses of 0.5 to >200mm can be achieved with a single coat process. The excellent imaging characteristics of SU-8 are maintained. The exposed and subsequently cross-linked portions of the film are rendered insoluble to liquid developers. SU-8 2000 has very high optical transparency above 360nm, which makes it ideally suited for imaging near vertical sidewalls in very thick films. SU-8 2000 is best suited for permanent applications where it is imaged, cured and left in place

Process Guidelines

SU-8 2000 is most commonly processed with conventional near UV (350-400nm) radiation, although it may be imaged with e-beam or x-ray. i-line (365nm) is recommended. Upon exposure, cross-linking proceeds in two steps (1) formation of a strong acid during the exposure process, followed by (2) acid-initiated, thermally driven epoxy cross-linking during the post exposure bake (PEB) step.

Substrate Pretreat

Coat

Soft Bake

Expose

Post Expose Bake (PEB)

Develop

Rinse & Dry

Hard Bake *(optional)*

Imaged Material

Remove *(optional)*

Figure F.1: Data sheet for SU-8.

155

A normal process is: spin coat, soft bake, expose, post expose bake (PEB) followed by develop. A controlled hard bake is recommended to further cross-link the imaged SU-8 2000 structures when they will remain as part of the device. The entire process should be optimized for the specific application. A baseline process is given here to be used as a starting point.

Substrate Pretreat

To obtain maximum process reliability, substrates should be clean and dry prior to applying the SU-8 2000 resist. Start with a solvent cleaning, or a rinse with dilute acid, followed by a DI water rinse. Where applicable, substrates should be subjected to a piranha etch / clean (H_2SO_4 & H_2O_2). To dehydrate the surface, bake at 200°C for 5 minutes on a contact hot plate or 30 minutes in a convection oven. Adhesion promoters are typically not required. For applications that require electroplating and subsequent removal of SU-8 2000 apply MicroChem's OmniCoat prior to processing.

Coat

SU-8 2000 resists are designed to produce low defect coatings over a very broad range of film thickness. The film thickness versus spin speed data displayed in Table 1 and Figure 1 provide the information required to select the appropriate SU-8 2000 resist and spin conditions, to achieve the desired film thickness.

The recommended coating conditions are:

(1) STATIC Dispense: Approximately 1ml of SU-8 2000 per inch of substrate diameter.
(2) Spread Cycle: Ramp to 500 rpm at 100 rpm/second acceleration. This will take 5 seconds.
(3) Spin Cycle: Ramp to final spin speed at an acceleration of 300 rpm/second and hold for a total of 30 seconds.
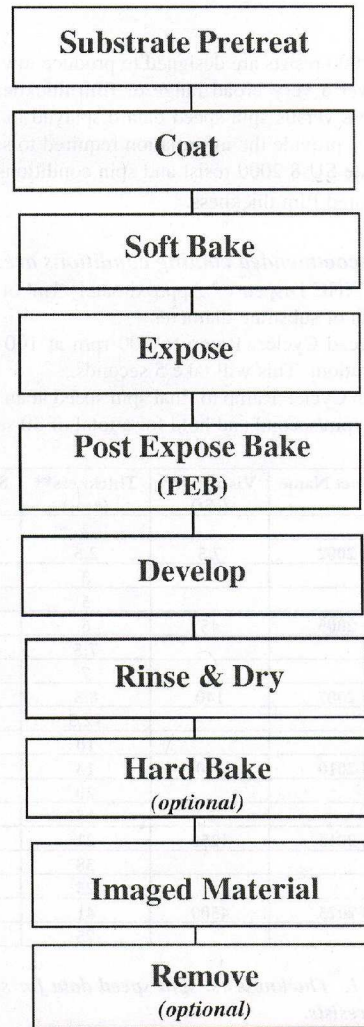
Product Name	Viscosity** (cSt)	Thickness** (μms)	Spin Speed (rpm)
		2	3000
SU-8 2002	7.5	2.5	2000
		3	1000
		5	3000
SU-8 2005	45	6	2000
		7.5	1000
		7	3000
SU-8 2007	140	8.5	2000
		12.5	1000
		10	3000
SU-8 2010	380	13	2000
		20	1000
		15	3000
SU-8 2015	1250	21	2000
		38	1000
		25	3000
SU-8 2025	4500	41	2000
		75	1000

Table 1. Thickness vs. spin speed data for selected SU-8 2000 resists.
** Approximate
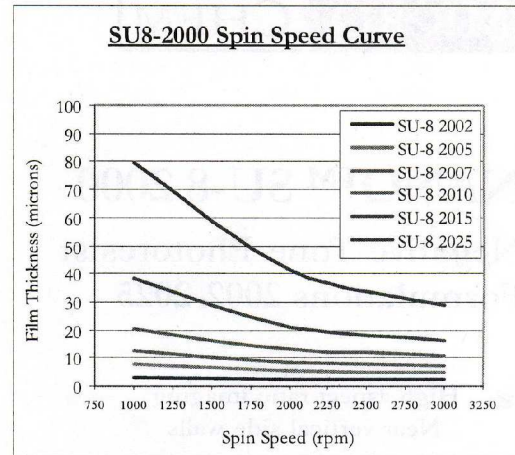
Figure 1. Spin speed vs. thickness curves for selected SU-8 2000 resists.

Soft Bake

After the resist has been applied to the substrate, it must be soft baked to evaporate the solvent and densify the film. SU-8 2000 is normally baked on a level hot plate, although convection ovens may be used. The following bake times are based on contact hot plate processes. Bake times should be optimized for proximity and convection oven bake processes since solvent evaporation rate is influenced by the rate of heat transfer and ventilation.

For best results, ramping or stepping the soft bake temperature is recommended. Lower initial bake temperatures allow the solvent to evaporate out of the film at a more controlled rate, which results in better coating fidelity, reduced edge bead and better resist-to-substrate adhesion. Refer to Table 2. for TWO STEP contact hot plate process recommendations.

Product Name	Thickness (μms)	Pre-bake @ 65°C	Softbake @ 95°C
	2	1	2
SU-8 2002	2.5	1	2
	3	1	2
	5	1	2
SU-8 2005	6	1	2
	7.5	1	2
	7	1	2
SU-8 2007	8.5	1	2
	12.5	1	2
	10	1	2
SU-8 2010	13	1	2
	20	1	3
	15	1	2
SU-8 2015	21	1	3
	38	2	5
	25	1	3
SU-8 2025	41	2	5
	75	3	9

Table 2. Recommended soft bake parameters

Figure F.2: Data sheet for SU-8.

156

Expose

SU-8 is optimized for near UV (350-400nm) exposure. i-line exposure tools are recommended. SU-8 is virtually transparent and insensitive above 400nm but has high actinic absorption below 350nm. This can be seen in Figure 2. Excessive dose below 350nm may, therefore, result in over exposure of the top portion of the resist film, resulting in exaggerated negative sidewall profiles or T-topping. The optimal exposure dose will depend on film thickness (thicker films require higher dosage) and process parameters. The exposure dose recommendations in Table 3. are based on source intensity measurements taken with an i-line (365nm) radiometer and probe.

Expose tip: When using a broad spectral output source, for best imaging results, i.e. straightest sidewalls, filter out excessive energy below 350nm.

Catastrophic adhesion failure, severely negative sidewalls and excessive cracking often indicate an under cross-linking condition. To correct the problem, increase the exposure dose and/or increase the post exposure bake (PEB) time.

Table 3. Recommended expose dose processes

Post Expose Bake

Following exposure, a post expose bake (PEB) must be performed to selectively cross-link the exposed portions of the film. This bake can be performed either on a hot plate or in a convection oven. Optimum cross-link density is obtained through careful adjustments of the exposure and PEB process conditions. The bake recommendations below are based on results obtained with a contact hot plate.

PEB tip: SU-8 is readily cross-linked and can result in a highly stressed film. To minimize stress, wafer bowing and resist cracking, a slow ramp or TWO STEP contact hot plate process, as shown in Table 4., is recommended. Rapid cooling after PEB should be avoided.

Figure 2. SU-8 absorbance vs. film thickness

Product Name	Thickness (μms)	PEB 1 @ 65°C	PEB 2 @ 95°C
	2	1	1
SU-8 2002	2.5	1	1
	3	1	1
	5	1	1
SU-8 2005	6	1	1
	7.5	1	1
	7	1	1
SU-8 2007	8.5	1	2
	12.5	1	2
	10	1	2
SU-8 2010	13	1	2
	20	1	2
	15	1	2
SU-8 2015	21	1	2
	38	1	3
	25	1	3
SU-8 2025	41	1	3
	75	1	7

Table 4. Recommended post expose bake parameters

Figure F.3:   Data sheet for SU-8.

157

Develop

SU-8 2000 resists have been optimized for use with MicroChem's SU-8 Developer. Immersion, spray or spray-puddle processes can be used. Other solvent based developers such as ethyl lactate and diacetone alcohol may also be used. Strong agitation is recommended for high aspect ratio and/or thick film structures. Recommended develop times are given in Table 5. for immersion processes. These proposed develop times are approximate, since actual dissolution rates can vary widely as a function of agitation rate, temperature and resist processing parameters.

Product Name	Thickness (μms)	Development (minutes)
	2	1
SU-8 2002	2.5	1
	3	1
	5	1
SU-8 2005	6	1
	7.5	1
	7	1
SU-8 2007	8.5	2
	12.5	3
	10	2
SU-8 2010	13	3
	20	3
	15	3
SU-8 2015	21	3
	38	4
	25	4
SU-8 2025	41	5
	75	7

Table 5. Recommended develop processes

Rinse and Dry

Following development, the substrate should be rinsed briefly with isopropyl alcohol (IPA), then dried with a gentle stream of air or nitrogen.

Rinse tip: If a white film is produced during rinse, this is an indication that the substrate has been under developed. Simply immerse or spray the substrate with SU-8 developer to remove the film and complete the development process. Repeat the rinse step.

Hard Bake (cure)

SU-8 2000 has good mechanical properties, therefore hard bakes are normally not required. For applications where the imaged resist is to be left as part of the final device, the resist may be ramp/step hard baked between 150-200°C on a hot plate or in a convection oven to further cross link the material. Bake times vary based on type of bake process and film thickness.

Removal

SU-8 2000, after expose and PEB, is a highly cross-linked epoxy, which makes it extremely difficult to remove with conventional solvent based resist strippers. MicroChem's Remover PG will swell and lift off minimally cross-linked SU-8 2000. However, if OmniCoat has been applied immersion in Remover PG should effect a clean and thorough Lift-Off of the SU-8 2000 Material. It will not remove fully cured or hard baked SU-8 2000 without the use of OmniCoat. Alternate removal processes include immersion in oxidizing acid solutions such as piranha etch / clean, plasma ash, RIE, laser ablation and pyrolosis.

To remove minimally cross-linked SU-8 2000, or if using Omnicoat, with Remover PG, heat the bath to 50-80°C and immerse the substrates for 30-90 minutes. Actual strip time will depend on resist thickness and cross-link density. For more information on MicroChem Omnicoat and Remover PG please see the relevant product data sheets.

Storage

Store SU-8 2000 resists upright in tightly closed containers in a cool, dry environment away from direct sunlight at a temperature of 40-70°F(4-21°C). Store away from light, acids, heat and sources of ignition. Shelf life is twelve months from date of manufacture.

Disposal

SU-8 2000 resists may be included with other waste containing similar organic solvents to be discarded for destruction or reclaim in accordance with local state and federal regulations. It is the responsibility of the customer to ensure the disposal of SU-8 2000 resists and residues made in observance all federal, state, and local environmental regulations.

Environmental, Health and Safety

Consult product Material Safety Data Sheet before working with SU-8 2000 resists. Handle with care. Wear chemical goggles, chemical gloves and suitable protective clothing when handling SU-8 2000 resists. Do not get into eyes, or onto skin or clothing. Use with adequate ventilation to avoid breathing vapors or mist. In case of contact with skin, wash affected area with soap and water. In case of contact with eyes, rinse immediately with water and flush for 15 minutes lifting eyelids frequently. Get emergency medical assistance.

The information is based on our experience and is, we believe to be reliable, but may not be complete. We make no guarantee or warranty, expressed or implied, regarding the information, use, handling, storage, or possession of these products, or the application of any process described herein or the results desired, since the conditions of use and handling of these products are beyond our control.

MICRO CHEM
1254 Chestnut Street
Newton, MA 02464
tel: (617)965-5511 fax: (617)965-5818
email: mcc@microchem.com www.microchem.com

Rev. 2/02

Figure F.4: Data sheet for SU-8.

Bibliography

1. A. Liu, A. Asundi. "Photonic Bandgap Crystals-A Breakthrough for New Generation Integrated Optical Device". *SPIE*, (5145):98–106, 2003.

2. Agresta, Mr. Donald, 2005. Electronic Engineer, AFRL/SNDP, WPAFB.

3. Burzynski, Ryszard, 2005. Hybrid Technologies.

4. C. Summers, *et al.* "Tunable Photonic Crystal Structures". *SPIE*, 5511:81–92, 2004.

5. Constantino, 2005. AFRL/MLPJ, WPAFB.

6. D. C. Meisel, *et al.* "Three-dimensional photonic crystals by holographic lithography using the umbrella configuration: symmetries and complete photonic band gaps". *Phys Rev B*, 70, 2004.

7. H. Driel, *et al.* "Tuning 2-D Photonic Crystals". *SPIE*, 5511:1–9, 2004.

8. Haus, Dr., 2005. Director Electro-Optics Program, University of Dayton.

9. Hecht, Eugene. *Optics*. Pearson Education Inc., California, fourth edition edition, 2002.

10. Hunsperger, Robert G. *Integrated Optics, Theory and Technology*. Springer-Verlag Berlin Heidelberg New York, fourth edition, 1982.

11. J.Fleming, S.YuLin. "Fabrication and Properties of 3-D Polysilicon Photonic Lattices in the Infrared". *IEEE*, 366–370, 1999.

12. J.Joannopoulos, J. Winn, R. Meade. *Photonic Crystals, Molding the Flow of Light*. Princeton University Press, New Jersey, 1995.

13. Johnson, Howard. "Dielectric Loss Tangents". *On Line Newsletter*, 2005. *www.sigcon.com/Pubs/news/4_5.htm*.

14. Johnson, S. and J. Joannopoulos. *Introduction to Photonic Crystals : Bloch's Theorem, Band Diagrams, and Gaps (but no defects)*. Technical report, MIT, MIT, Boston, MA, 2003.

15. Noda, S. "Three-dimensional photonic crystals operating at optical wavelength region". *Physica B*, 279:142–149, 2000.

16. S. Johnson, J.Joannopoulos. *Photonic Crystals, The Road from Theory to Practice*. Massachusetts Institute of Technology, Massachusetts, 2002.

17. S. Kawakami, *et al.* "Mechanism of shape formation of three-dimensional periodic nanostructures by bias sputtering". *Appl. Phys. Lttrs*, 74(3), 1999.

18. Saleh, B.E.A. and M.C. Teich. *Fundamentals of Photonics*. John Wiley & Sons, Inc., New York, NY, 1991.

19. S.R. Kennedy, *et al.* "Optical properties of a three-dimensional silicon square spiral photonic crystal". *Photonic and Nanostructures F and A*, 2003.

20. Sutherland, Dr. Richard, 2005. AFRL/MLPJE, WPAFB.

21. Toader, *et al.* "Photonic Band Gaps Based on Tetragonal Lattices of Slanted Pores". *Physica Review Letters*, 90(23), June 2003.

22. Tondiglia, Vincent, 2005. AFRL/MLPJ, WPAFB.

23. Venkataraman, *et al.* "Fabrication of 3D silicon photonic crystal structures using conventional micromachining technology". *SPIE*, 5347, 2004.

24. W. Park, *et al.* "Tunable Nanophotonic Device Based on Flexible Photonic Crystal". *SPIE*, 5511, 2004.

25. Yablonovitch, E. "Photonic Crystals : Semiconductors of Light". *Scientific American*, 47–55, Dec 2001.

26. Yu. V. Miklyaev, *et al.* "Three-dimensional face-centered-cubic photonic crystal templates by laser holography: fabrication, optical characterization, and band-structured calculations". *Appl. Phys. Lttrs.*, 82, 2003.

REPORT DOCUMENTATION PAGE

The public reporting burden for this collection of information is estimated to average 1 hour per response, including the time for reviewing instructions, searching existing data sources, gathering and maintaining the data needed, and completing and reviewing the collection of information. Send comments regarding this burden estimate or any other aspect of this collection of information, including suggestions for reducing this burden to Department of Defense, Washington Headquarters Services, Directorate for Information Operations and Reports (0704–0188), 1215 Jefferson Davis Highway, Suite 1204, Arlington, VA 22202–4302. Respondents should be aware that notwithstanding any other provision of law, no person shall be subject to any penalty for failing to comply with a collection of information if it does not display a currently valid OMB control number. **PLEASE DO NOT RETURN YOUR FORM TO THE ABOVE ADDRESS.**

1. REPORT DATE *(DD–MM–YYYY)*	2. REPORT TYPE	3. DATES COVERED *(From — To)*
01–03–2006	Master's Thesis	Sept 2004 — Mar 2006

4. TITLE AND SUBTITLE

CHARACTERISTICS OF TWO-DIMENSIONAL TRIANGULAR AND THREE-DIMENSIONAL FACE-CENTERED-CUBIC PHOTONIC CRYSTALS

5a. CONTRACT NUMBER

5b. GRANT NUMBER

5c. PROGRAM ELEMENT NUMBER

6. AUTHOR(S)

Jeffrey Dustin Clark, Major, USAF

5d. PROJECT NUMBER

5e. TASK NUMBER

5f. WORK UNIT NUMBER

7. PERFORMING ORGANIZATION NAME(S) AND ADDRESS(ES)

Air Force Institute of Technology
Graduate School of Engineering and Management
2950 Hobson Way
WPAFB OH 45433-7765

8. PERFORMING ORGANIZATION REPORT NUMBER

AFIT/GEO/ENP/06-01

9. SPONSORING / MONITORING AGENCY NAME(S) AND ADDRESS(ES)

N/A

10. SPONSOR/MONITOR'S ACRONYM(S)

11. SPONSOR/MONITOR'S REPORT NUMBER(S)

12. DISTRIBUTION / AVAILABILITY STATEMENT

APPROVED FOR PUBLIC RELEASE; DISTRIBUTION UNLIMITED

13. SUPPLEMENTARY NOTES

14. ABSTRACT

The fabrication of photonic crystals (PhC) with photonic band gaps (PBG) in the visible range is a difficult task due to the small structural feature sizes of the PhC. The particular type of PhC examined is a two-dimensional (2-D) triangular structure with a PBG designed for visible wavelengths with applications in visible integrated photonic systems. This work examines the processes involved and viability of fabricating 2-D triangular PhC's by a variety of techniques: focused ion beam, electron lithography and holographic photo-polymerization/lithography. The design of the PhC was based on a program created to display gap maps for triangular structures. The PBG of the structure designed from the gap maps was then modeled using another program created to display band diagrams for triangular PhC structures. The fabrication techniques and materials used to create the PhC in part determine the characterization technique required to investigate the PBG. Techniques used here include the coupling of a beam by means of a prism into a wave-guiding medium and edge firing. Two commercial FDTD modeling programs were evaluated. Finally, FDTD modeling and simulation results are compared to the design and experimental results. Experimental techniques and results, along with modeling and simulation results, will be discussed.

15. SUBJECT TERMS

Photonic Crystals, Photonic Band Gaps, 2-D Triangular PhC, FIB, Holographic Lithography

16. SECURITY CLASSIFICATION OF:			17. LIMITATION OF ABSTRACT	18. NUMBER OF PAGES	19a. NAME OF RESPONSIBLE PERSON
a. REPORT	b. ABSTRACT	c. THIS PAGE			Dr. Michael A. Marciniak, AFIT/ENP
U	U	U	UU	181	**19b. TELEPHONE NUMBER** *(include area code)* (937) 255–3636, ext 4529